universität wien

DISSERTATION

Titel der Dissertation

Thermoacoustic Tomography with Circular Integrating Detectors

Verfasser

Gerhard Zangerl

angestrebter akademischer Grad

Doktor der Naturwissenschaften (Dr.rer.nat)

Wien, im November 2010

Contents

Abstract

At the present day, imaging methods are very important in medical diagnostics. A new promising method is Thermoacoustic Tomography, which is a hybrid imaging technique that is capable of imaging light absorption properties of biological objects. The main emphasis of this thesis is the derivation of reconstruction formulas that can be used to convert data, collected by circular integrating detectors, into an image of the desired absorbtion properties. The derived formulas lead to fast and stable reconstruction algorithms. Further, we present numerical results from simulated data that show the robustness of our algorithms.

Zusammenfassung

Heutzutage sind bildgebende Verfahren sehr wichtig für die medizinische Diagnostik. Ein neues vielversprechendes Verfahren ist die Thermoakustische Tomographie, die in der Lage ist, Lichtabsorbtionseigenschaften biologischer Objekte darzustellen. Der Schwerpunkt dieser Doktorarbeit liegt in der Herleitung von Rekonstruktionsformeln, die dazu benützt werden können Daten, die mit zirkulär integrierenden Detektoren gesammelt wurden, in ein Bild der gewünschten Absorptionseigenschaften umzurechen. Die hergeleiteten Formeln führen zu stabilen und schnellen Rekonstruktionsalgorithmen. Im weiteren presentieren wir numerische Resultate die zeigen, dass unsere Algorithmen robust und stabil sind.

Introduction

Thermoacoustic tomography (TAT), which is also known as opto- or photoacoustic tomography, is a new non–invasive imaging modality with various applications in medicine and biology. This imaging technique utilizes the fact that an object that it is illuminated by electromagnetic radiation emits sound waves. These waves are recorded by pressure sensitive detectors and converted into a three dimensional image of the object. To obtain an image from pressure data, a mathematical model is needed that describes acoustic

wave propagation. Once such a model is chosen reconstruction algorithms can be derived that convert data into images.

The main emphasis of this thesis is the derivation of explicit reconstruction formulas for TAT, in the case that acoustic pressure is measured with circular integrating detectors. The implementation of these formulas will lead to fast reconstruction algorithms. Besides this practical reason, explicit reconstruction formulas can also provide insight into the underlying mathematical problem.

As its name implies, a circular integrating detector in TAT is a device that measures a quantity that is proportional to the integral of acoustic pressure over a circle. We will derive two different kinds of reconstruction formulas that use data which are collected by circular integrating detectors. The first type uses the circular integrals directly for imaging, whereas the second type reconstructs acoustic pressure pointwise first. Once the pressure is known pointwise, reconstruction formulas are applied that are based on pointwise data.

Moreover, we investigate the problem that in practice only approximate circular, or toroidal, detectors can be fabricated, which measure inexact pressure integrals. We apply a model that describes a toroidal detector and use it for analyzing the influence, of erroneous measurements, on the reconstructed images.

The outline of this thesis is as follows:

Chapter 1. Overview. We shortly explain the physical context and provide the mathematical model of TAT that we use in this thesis. Moreover, we give an overview of existing works in TAT and present some reconstruction formulas.

Chapter 2. Circular Integrating Detectors and presentation of the main results. We shortly motivate and explain circular integrating detectors, and present the main results that are derived in this thesis. Furthermore, we present new reconstruction formulas derived from the limiting case when the radius of a circular integrating detector approaches zero.

Chapter 3. Two step reconstruction Algorithms. This chapter contains detailed explanations and derivations of reconstruction formulas that are derived for special measuring configurations of circular detectors.

Chapter 4. Conversion of Measurement data. We consider integrals of

acoustic pressure over two families of circles in the plane and derive pointwise reconstruction formulas for each family.

Chapter 5. Resolution of Circular Integrating Detectors. A model that describes the inaccuracy of an approximate circular integrating (toroidal) detector is presented. Based on this model the blurring in reconstructed images caused by inaccurate measurements is studied.

Chapter 6. Numerical Results. We simulate the data that are collected by the arrangement of circles considered in chapter 3. Two dimensional sections, of the initial pressure, derived from reconstruction formulas in this chapter, are shown.

Appendix. We give a list of the integral transforms that are used in this thesis. Further we proof some results that were used in the thesis and present the derivation of the model that is commonly used in TAT with homogeneous sound speed.

Attachment. Moreover, two additional works where the author was involved, on TAT with linear integrating detectors, are attached to this thesis [20, 21]. These works are related to the present topic, as a circular integrating detector approximates a linear detector when its radius is large enough.

Chapter 1

Overview

1.1 Physical context and mathematical model

TAT is a new imaging method that is attractive to medicine and biology because it is capable to provide a three dimensional image of electromagnetic absorbtion properties of biological tissue. These properties are of considerable interest for medical diagnostics as they are related to the molecular composition of tissue and reveal its pathological condition [13, 27].

In TAT we assume that a small sample of biological tissue is placed inside a water tank and is illuminated by a short pulse of electromagnetic radiation, see figures 1.1 and 1.2. Electromagnetic energy is absorbed by the object and causes a thermoelastic expansion [33, 30, 31, 32]. A consequence of this expansion is an acoustic ultrasound wave that is related to the electromagnetic absorbtion properties of the object. Pressure changes due to the ultrasound wave can be measured by an arrangement of detectors that is also assumed to be contained in the water tank.

Ultrasound in TAT carries information about the electromagnetic absorbtion properties of tissue, which are also imaged in optical tomography by algorithms that require the intensity of backscattered light from tissue as measurement data [7, 51, 8]. By this means, TAT combines optical and ultrasound imaging and thus represents a hybrid imaging technique [56, 15]. TAT is capable of imaging electromagnetic absorption properties with high resolution because of the information conserving propagation of sound waves.

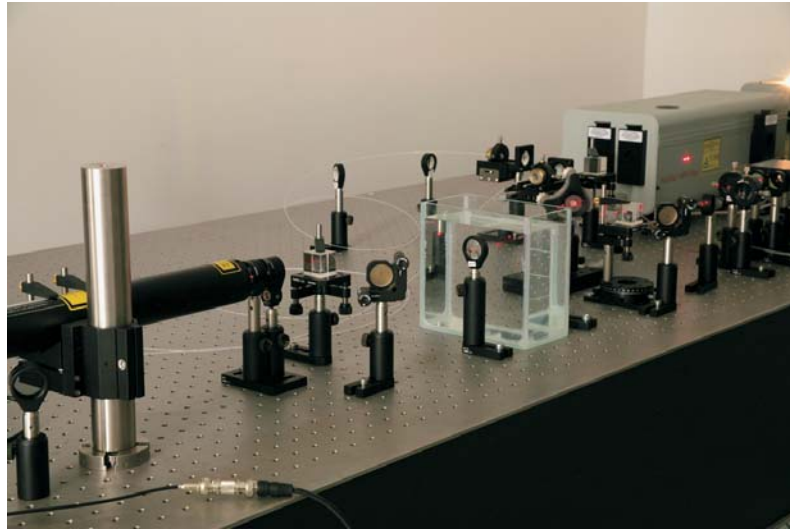Figure 1.1: An experimental setup for TAT fixed on a laboratory bench. An object, contained in the water tank, is illuminated by an excitation laser.
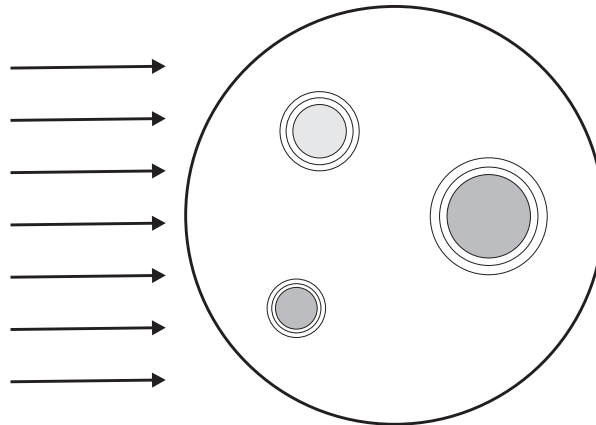

Figure 1.2: An object (for instance a sample of tissue) is exposed to a short laser pulse (rays from the left) that is absorbed inside the object (gray shaded areas) which causes the propagation of a sound wave (concentric circles around gray shaded areas).

The conversion of pressure measurements into a three dimensional image requires a model that describes acoustic wave propagation. Mathematically, the propagation of sound waves in tissue is modeled as a Cauchy Problem for the wave equation with constant sound speed. A derivation of this model, from the governing equations of fluid–and thermodynamics can be found in the appendix.

Throughout this thesis we assume that thermoacoustic pressure p satisfies the Cauchy problem

$$\partial_t^2 p(\mathbf{x}, t) = \Delta p(\mathbf{x}, t), \qquad (\mathbf{x}, t) \in \mathbb{R}^3 \times (0, \infty), \qquad (1.1)$$
$$p(\mathbf{x}, 0) = f(\mathbf{x}), \qquad \mathbf{x} \in \mathbb{R}^3, \qquad (1.2)$$
$$\partial_t p(\mathbf{x}, 0) = 0, \qquad \mathbf{x} \in \mathbb{R}^3, \qquad (1.3)$$

for the three dimensional wave equation where $\mathbf{x}$ denotes a point in three dimensional space $\mathbb{R}^3$ and $t \geq 0$ denotes the time variable. Further we refer to $f(\mathbf{x}) \in C_0^\infty(\Omega)$ as the initial density or initial pressure of the considered Cauchy problem, where $C_0^\infty(\Omega)$ denotes the space of infinitely differentiable functions that are compactly supported in the domain $\Omega \subset \mathbb{R}^3$.

We mention here that also more complicated models, which investigate inhomogeneous sound speed and attenuation effects, have been studied [2, 12, 28, 29].

1.2 TAT with pointlike detectors

Several explicit reconstruction formulas for the initial pressure have been derived in TAT for pointwise measurement data. As examples we present two particular reconstruction formulas and mention practical problems for TAT with approximate point, or pointlike, detectors. Because of these problems researchers have been motivated to develop linear–and circular integrating detectors.

The presented formulas relate the initial density and the measurement data by means of integral transforms. A list of these transforms can be found in the appendix of this thesis.

Classically, the *inverse problem* in TAT is to recover the function f from pointwise pressure data recorded over time on the boundary $\partial\Omega$, which is assumed to be smooth. The considered inverse problem for point like detectors

deals with the inversion of the operator

$$P : \mathcal{C}_0^\infty(\Omega) \to \mathrm{ran}(P) \subset \mathcal{C}^\infty(\partial\Omega \times \mathbb{R}_{>0}), \quad P(f) = p\,|_{\partial\Omega \times \mathbb{R}_{>0}}, \qquad (1.4)$$

where p is a solution of the Cauchy problem (1.1) -(1.2). For special geometries, for instance when $\partial\Omega$ is either a sphere, a cylinder, or a plane, several exact frequency domain reconstruction formulas have been derived [59, 58, 55, 54, 60]. Also Fourier series formulas that expand f in the basis of eigenfunctions of the operator Δ_Ω have been derived in [57, 36]. An extensive review of reconstruction methods and recent progress in TAT can be found in [34]. Moreover, when Ω is a sphere and the spaces in equation (1.4) are equipped with appropriate norms, it is known that the operator P is an isometry [16].

The examples we present here were derived in [59, 58, 55]. Furthermore, we will see that reconstruction formulas derived for circular integrating detectors have a similar form.

Firstly, assume that pointwise data $g = P(f)$ are given on the surface of the cylinder $\partial\Omega = \partial(B_R(0) \times \mathbb{R})$. Further, we denote by $f^m(z, r)$ and $g^m(z, t)$ the $m-$th Fourier coefficient of the initial pressure and the measurement data (described in cylindrical coordinates which are introduced in section 3.1) with respect to the angular variable. Then the relation,

$$\mathbf{H}_r \left\{ \mathbf{F}_z \left\{ f^m \right\} \right\} (k, v) = \frac{2}{\pi} \frac{\mathbf{F}_t \left\{ \mathbf{F}_z \left\{ g^m \right\} \right\} (k, \sqrt{k^2 + v^2})}{H_n^{(2)}(Rv)\sqrt{k^2 + v^2}}, \qquad (k, v) \in \mathbb{R} \times (0, \infty),$$

$$(1.5)$$

holds, where $\mathbf{H}$, $\mathbf{F}$ and $H_n^{(2)}$ denote the Hankel–and Fourier transform and the second order Hankel function of order n respectively. As outlined in the appendix the subscripts r, z and t indicate to which variable an integral transforms is applied.

Secondly, we assume that pointwise measurements are given on a sphere S_R of radius R. We denote pointwise measurements again by g and by $f^m(r, \vartheta)$ and $g^m(\vartheta, t)$ the $m-$th Fourier coefficients of f and g (described in spherical coordinates which are introduced in section 3.2) with respect to the angular variable. We obtain the following relation,

$$\mathbf{H}_r^l \{ f_l^m \}(\omega) = \frac{2}{\pi} \frac{\mathbf{F}_t \{ g_l^m \}(\omega)}{\omega^2 \, h_l^{(1)}(R\omega)}, \qquad \omega \in \mathbb{R}, \ l \in \mathbb{N}, \qquad (1.6)$$

where $h_l^{(1)}$ denotes the spherical Hankel function.

Finally, we mention practical problems that are related to TAT with point-like detectors. The formulas above assume that acoustic pressure is known pointwise. However, in practice, acoustic pressure is measured by piezoelectric transducers, which can only provide approximate pointwise (pointlike) measurements. For this reason, the formulas above yield images with a spatial resolution that is essentially limited by the size of the piezoelectric transducers [56]. The size of a piezoelectric detector, which is typically a square of a side length of about 400μm, can in principle be reduced. However, reducing the size of a pointlike detector also decreases its signal–to–noise ratio.

1.3 TAT with linear integrating detectors

A first approach that tried to overcome the problem of finite aperture size of piezoelectric transducers has been given by M. Xu and L. Wang in [56]. Therein the spatial blurring caused by detectors is modeled as a convolution with a point–spread function of ultrasonic transducers and is used to improve reconstructions by deconvolution.

A practical approach, that tries to overcome the limitations due to finite aperture sice of detectors, was proposed in [11], where linear integrating, or shortly, linear detectors were introduced. A linear integrating detector in TAT that measures the integral of acoustic pressure over a line is, for instance, realized by a thin laser beam. A linear detector reduces the problems caused by finite aperture size because it is capable to approximate a line very accurately [44, 23].

The inverse problem in TAT with linear integrating detectors is to recover the initial density from a two dimensional family of line integrals. Different measurement configurations for linear integrating detectors are considered in [18, 47, 10, 16, 46, 11].

As an example for TAT with linear detectors we present the setup considered in [11] because it motivates a similar setup for circular detectors. In [11] line integrals of acoustic pressure are given by the two dimensional family of lines that are tangential to a cylinder of radius R and are parallel to the $xy-$plane, see figure 1.3. For the sake of simplicity we assume that the cylinder is centered at the origin. Moreover we require that the initial
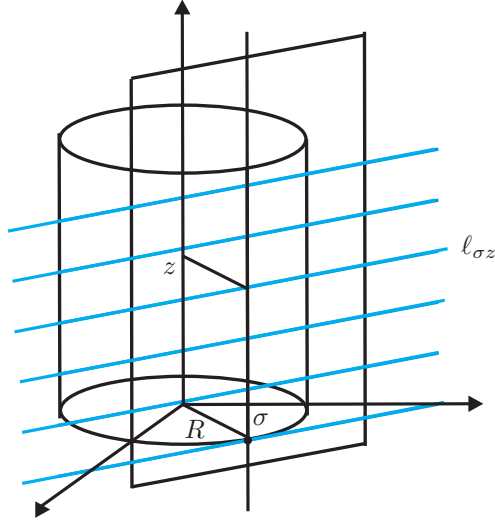
Figure 1.3: A one dimensional family of lines tangential to a cylinder.

pressure is supported inside the cylinder. For every $\sigma \in S^1$ denote by (x, y, z) the coordinates of a point $\mathbf{x} \in \mathbb{R}^3$ with respect to the basis $(\check{\sigma}, \check{\sigma}^{\perp}, e_3)$, where $\check{\sigma} = (\sigma, 0)$ and $\check{\sigma}^{\perp} = (\sigma^{\perp}, 0)$. For the considered family of line integrals, TAT with linear integrating detectors is concerned with the inversion of the operator

$$L : \mathcal{C}_0^{\infty}(B_R(0) \times \mathbb{R}) \longrightarrow \operatorname{ran}(L) \subset \mathcal{C}^{\infty}(S^1 \times \mathbb{R} \times \mathbb{R}_{>0}) \qquad (1.7)$$

$$(Lf)(\sigma, z, t) := \int_{\mathbb{R}} p(R\check{\sigma} + y\check{\sigma}^{\perp} + ze_3, t)\, dy,$$

where $x = R$ and $B_R(0)$ denotes the ball of radius R that is centered at the origin.

In the following, we use the abbreviation

$$G_{\sigma}^{L}(z, t) := (Lf)(\sigma, z, t) \qquad (1.8)$$

to denote the integral line over the line $\ell_{\sigma z}$, see figure 1.3. Further denote by

$$F_{\sigma}^{L}(x, z) := \int_{\mathbb{R}} f(x\check{\sigma} + y\check{\sigma}^{\perp} + ze_3)\, dy \qquad (1.9)$$

the integrated initial pressure f.

One of the main results in [11] states that the line integrals (1.8), i.e. our measurements, and the integrated initial data satisfy the relation

$$\mathbf{C}_x \left\{ \mathbf{F}_z \left\{ F_\sigma^L \right\} \right\} (k, v) = \mathbf{C}_t \left\{ \mathbf{F}_z \left\{ G_\sigma^L \right\} \right\} (k, \sqrt{k^2 + v^2}) \frac{k}{\sqrt{k^2 + v^2}}, \qquad (1.10)$$

where the cosine transform $\mathbf{C}$ can be found in the appendix. Using formula (1.10) we propose the following reconstruction procedure for the initial pressure f:

Assume the function F_σ^L is be determined by formula (1.10) for all $\sigma \in S^1$. Subsequently, we fix the variable z and consider the function

$$(\sigma, x) \mapsto F_\sigma^L(x, z), \qquad (1.11)$$

which in fact, see definition (1.9) and figure 1.4, is the 2D Radon transform of the initial pressure f restricted to the plane $\mathbb{R}^2 \times \{z\}$. Applying the inverse 2D Radon transform

$$f(x, y, z_0) = \frac{-1}{(2\pi)^2} \int_\mathbb{R} \frac{1}{q} \left(\int_{S^1} \frac{\partial}{\partial s} F_\sigma(s, z_0) \Big|_{s = \sigma \cdot \binom{x}{y} + q} d\sigma \right) dq$$

in each plane $\mathbb{R}^2 \times \{z_0\}$ yields the desired reconstruction of f, where the notation in [41].

Besides explicit reconstruction formulas, the influence of measurement errors is investigated in [20, 23]. More precisely, two kinds of errors are considered, where the first one is due to the finite width of a laser beam that is used to measure a line integral. Secondly, the effect of imprecise time measurements, which are modeled by a impulse response function, are investigated. Since a linear detector approximates a line accurately, approximation errors due to the width of the laser beam can be neglected. Nevertheless, it is interesting to analyze the influence of inaccurate measurements.

The results in [23] hold for very general two dimensional families of line integrals. However, to explain the results, we assume that line integrals are given by the two dimensional family of lines which is considered in (1.7).

For this setup we model approximate measurements by

$$(L_{\varphi, \omega} f)(\sigma, z, t) = \varphi *_t \int_{\mathbb{R}^3} \omega(d(\ell_{\sigma z}, \mathbf{x})) \, p(\mathbf{x}, t) d\mathbf{x}. \qquad (1.12)$$
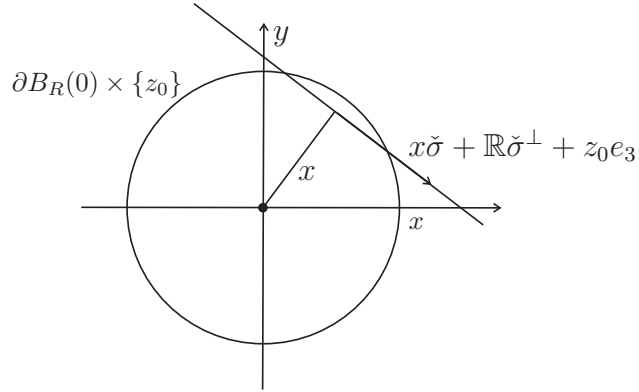
Figure 1.4: For $z = z_0$ fixed $F_\sigma^L(x, z_0)$ is the integral over the line in direction $\check{\sigma}^\perp$ that has distance x from the (outward pointing) $z-$axis, which is indicated by the black dot in the figure.

The weight ω is a function which describes the radial profile of a linear detector, φ denotes the impulse response function of the detector and d is the normal distance of a point $\mathbf{x} \in \mathbb{R}^3$ to the line $\ell_{\sigma z}$.

In order to determine an approximate solution fore the present setup for TAT with linear detectors usually the inverse L^{-1} of the operator (1.7) is applied to approximate measurements, which yields a blurred version of the desired initial pressure f. The main result in [20, 23] states that this blurred version is given by the identity

$$\left(L^{-1} L_{\varphi,\omega}\right)(f) = \Phi * W * f, \tag{1.13}$$

where the W and Φ are radially symmetric functions that are determined for ω and φ as outlined in [20]. Since Φ and W are known equation (1.13) can be used to determine f from the blurred version $\Phi * W * f$ by deconvolution.

We will give a similar analysis for circular integrating detectors. In this case the result (1.12) also holds true but its proof is harder.

Chapter 2

Circular Integrating Detectors and presentation of the main results

We shortly explain circular integrating detectors and summarize the main results of the thesis. Once more we bring to attention that a list of integral transforms is given in the appendix. Detailed derivations and explanations of the presented results can be found in the chapters 3, 4 and 5.

In applications an arrangement of detectors is positioned, or attached, beside an object in order to collect acoustic pressure data. The positioning of linear integrating detectors can be impractical because of their length [50]. Therefore in [62, 64] *circular integrating, or circular, detectors*, which are an alternative to pointlike and linear detectors, were introduced. As its name implies, such a detector measures a quantity that is proportional to the integral of acoustic pressure over a circle. Practically, they are realized by a laser beam which is guided along a circle in an optical fiber.

We mention that the use of circular integrating detectors was independently proposed by X. Yang and others in [61]. However, this study was limited to two spatial dimensions, where the circular shaped detector can be used as a virtual point detector.

If we use circular integrating detectors, instead of pointlike or linear detectors, the reconstruction process in TAT changes. Circular integrals of
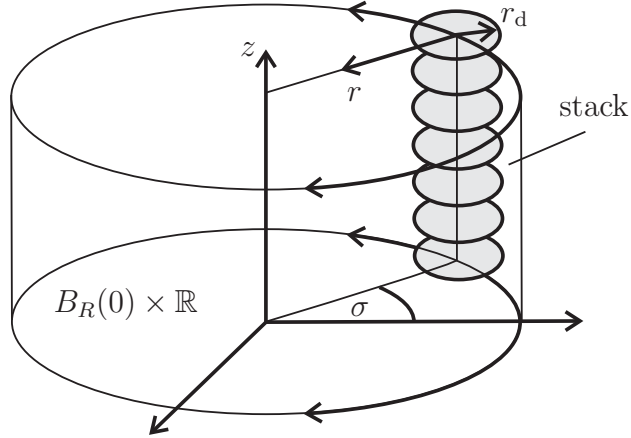
Figure 2.1: Scanning geometry: A stack of circles centered on the boundary of $B_R(0) \times \mathbb{R}$ is rotated around the $\mathbf{e}_3$-axis.

acoustic pressure are measured for a two dimensional family of circular detectors and are used to obtain a three dimensional reconstruction of the initial pressure. In the following, we will present reconstruction formulas that were derived in this thesis and have been published in [64, 65, 62, 63]:

Firstly, we generalize the setup which is shown in figure 1.3. We consider a stack of coaxial circles which are rotated around an object like depicted in figure 2.1. In order to obtain a reconstruction of the initial pressure we have to invert the operator

$$C : \mathcal{C}_0^\infty(B_R(0) \times \mathbb{R}) \longrightarrow \operatorname{ran}(C) \subset \mathcal{C}^\infty(S^1 \times \mathbb{R} \times \mathbb{R}_{>0}) \tag{2.1}$$

$$(Cf)(\sigma, z, t) := \frac{1}{2\pi} \int_0^{2\pi} p((r_{\mathrm{d}} \cos(\alpha), r_{\mathrm{d}} \sin(\alpha), 0) + R\check{\sigma} + z e_3) \, d\alpha,$$

where $\check{\sigma}, \check{\sigma}^\perp, e_3$ and $B_R(0)$ have the same meaning as in (1.7) and r_{d} denotes the radius of a circular integrating detector. If $\mathbb{R}^3$ is parameterized in cylindrical coordinates, see equation (3.2), it turns out that C can be inverted by solving a sequence of inverse problems, for a two dimensional wave equation, like explained in Proposition 3.1. We use the abbreviation

$$G_\sigma^C(z, t) := (Cf)(\sigma, z, t)$$

and

$$F_\sigma^C(z, r) = \frac{1}{2\pi} \int_0^{2\pi} f((r\cos(\alpha), r\sin(\alpha)) + R\check{\sigma} + ze_3)d\alpha, \qquad (2.2)$$

denotes the circular mean of f over the circles $\alpha \mapsto (r\cos(\alpha), r\sin(\alpha), z) + R\check{\sigma}$.

The main result of section 3.1.2 states that F_σ and the measurement data satisfy the relation

$$\mathbf{H}_r\left\{\mathbf{F}_z\left\{F_\sigma^C\right\}\right\}(k, v) = \frac{2}{\pi} \frac{\mathbf{C}_t\left\{\mathbf{F}_z\left\{G_\sigma^C\right\}\right\}(k, \sqrt{k^2 + v^2})}{J_0(r_\mathrm{d}v)\sqrt{k^2 + v^2}}, \qquad (2.3)$$

whenever $J_0(r_\mathrm{d}v) \neq 0$. It is interesting to note that formula (2.3) is quite similar to the inversion formula (1.10) for linear integrating detectors but where $\mathbf{C}_x$ and k are replaced by $\mathbf{H}_r$ and $1/J_0(rv)$ respectively.

The left side of formula (2.3) defines a $\mathcal{C}^\infty$ function since $f \in \mathcal{C}_0^\infty(\Omega)$. Therefore the fraction in (2.3) has to be defined whenever its denominator vanishes. Formally, applying the inverse Fourier and Hankel transforms (that can be found in the appendix) to formula (2.3) yields the explicit reconstruction formula

$$F_\sigma^C(z, r) = \frac{1}{\pi^2} \int_\mathbb{R} \int_0^\infty \frac{\mathbf{C}_t\left\{\mathbf{F}_z\left\{G_\sigma^C\right\}\right\}(k, \sqrt{k^2 + v^2})}{J_0(r_\mathrm{d}v)\sqrt{k^2 + v^2}} \, vJ_0(rv) \, e^{ikz}dvdk, \quad (2.4)$$

where the latter integral converges since $f \in \mathcal{C}_0^\infty(\Omega)$.

However, in practice the implementation of (2.4) causes problems due to the roots of its denominator. This problem can be circumvented in the case when the detector radii r_d become so large that the cylindrical stack of circles encloses the initial pressure. In this case a simple formula can deduced from (1.5), by observing that $F_\sigma^C(z, r) = f^0(z, r)$ and $G(z, t) = g^0(z, t)$, which is given by

$$\mathbf{H}_r\left\{\mathbf{F}_z\left\{F_\sigma^C\right\}\right\}(k, v) = \frac{2}{\pi} \frac{\mathbf{F}_t\left\{\mathbf{F}_z\left\{G_\sigma^C\right\}\right\}(k, \sqrt{k^2 + v^2})}{H_0^{(2)}(r_\mathrm{d}v)\sqrt{k^2 + v^2}} \, . \qquad (2.5)$$

Applying the inverse Hankel and Fourier transform to the right hand side gives a stable reconstruction formula since the absolute value of $H_0^{(2)}$ never vanishes, see figure 2.2. Moreover, in the present case we know that $F_\sigma(z, \cdot)$ is
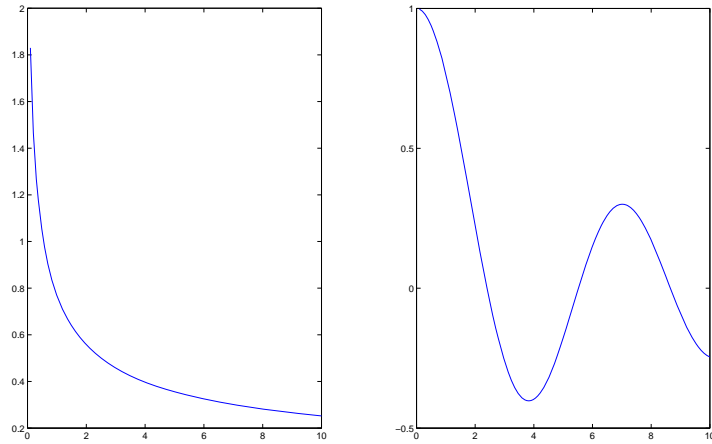
Figure 2.2: Left: Absolute value of the $0-$th order Hankel function of the second kind. Right: The $0-$th order Bessel function.

supported on $(0, r_\mathrm{d})$, which implies that $\mathbf{F}_z \{F_\sigma\} (k, \cdot)$ can be expanded into a Fourier Bessel series on $(0, r_\mathrm{d})$. This series expansion allows us to prove the inversion formula

$$F_\sigma^C(z, r) = \frac{2}{\pi^2 r_\mathrm{d}^3} \int_\mathbb{R} \left(\sum_{n \in \mathbb{N}} \frac{\mathbf{S}_t \{t\, \mathbf{F}_z \{G_\sigma\}\} \left(k, \sqrt{k^2 + v_n^2}\right) v_n}{k^2 + v_n^2} \frac{J_0(r v_n)}{J_1(r_\mathrm{d} v_n)^3} \right) e^{ikz} dk$$

(2.6)

in section 3.1.3, where the v_n are the roots of the function $v \mapsto J_0(r_\mathrm{d} v)$. Further, we can use relation (2.5) to derive an additional Fourier Bessel type inversion formula which is given by

$$F_\sigma^C(z, r) = \frac{2}{\pi^2 r_\mathrm{d}^2} \int_\mathbb{R} \left(\sum_{n \in \mathbb{N}} \frac{\mathbf{F}_t \{\mathbf{F}_z \{G_\sigma^C\}\} \left(k, \sqrt{k^2 + v_n^2}\right)}{H_0^{(2)}(r_\mathrm{d} v_n) \sqrt{k^2 + v_n^2}} \frac{J_0(r v_n)}{J_1(r_\mathrm{d} v_n)^2} \right) e^{ikz} dk\,.$$

(2.7)

The last two formulas allow for a stable reconstruction, see remark 3.3, of the integrated initial pressure F_σ^C. Numerical examples based on an implementation of these formulas are presented in chapter 6.

If we assume that the F_σ^C are determined by one of the reconstruction formulas above and that the variable z is fixed, it is not hard to see that the

map

$$(\sigma, r) \mapsto F_\sigma^C(r, z), \tag{2.8}$$

is the circular mean transform over circles which are centered on the circle $R \cdot S^1$. Reconstruction formulas for f from this integrals were found recently in [16, 17, 35, 36] and a back projection type formula is given explicitly in remark 3.1.

In section 3.2 we derive reconstruction formulas for a two dimensional family of circles of latitude on the sphere $S_R = \partial B_R$ of radius R, which is centered at the origin. The proposed proposed family is generated from the family depicted in figure 2.3 by rotating it around the x-axis.

This family of circles is beneficial for data acquisition since an acoustic pulse generated inside B_R passes through its surface in finite time T. Therefore, we don't expect artifacts, through to missing data, for the considered setup.

Note that this is contrarily to the case of a cylindrical stack of circular detectors. In this case, at least in applications, pressure signals, due to the finite hight of the stack, are lost.

Detailed proofs and explanations of the presented results can be found in section 3.2.

We are concerned with the inversion of the operator

$$S : \mathcal{C}_0^\infty(B_R) \longrightarrow \operatorname{ran}(S) \subset \mathcal{C}^\infty(S^1 \times [0, \pi] \times [0, T]) \tag{2.9}$$

$$(Sf)(\sigma, \vartheta, t) := \frac{1}{2\pi} \int_0^{2\pi} p(D_\sigma \cdot \Phi(R, \vartheta, \phi), t) \, d\phi,$$

where D_σ denotes

$$D_\sigma = \begin{pmatrix} 1 & 0 & 0 \\ 0 & \cos(\widetilde{\sigma}) & -\sin(\widetilde{\sigma}) \\ 0 & \sin(\widetilde{\sigma}) & \cos(\widetilde{\sigma}) \end{pmatrix} \tag{2.10}$$

the rotation around the $x-$axis, $\widetilde{\sigma} = \arg(\sigma)$ and

$$\Phi(r, \vartheta, \phi) = r\sin(\vartheta) \begin{pmatrix} \cos(\phi) \\ \sin(\phi) \\ 0 \end{pmatrix} + r \begin{pmatrix} 0 \\ 0 \\ \cos(\vartheta) \end{pmatrix}$$
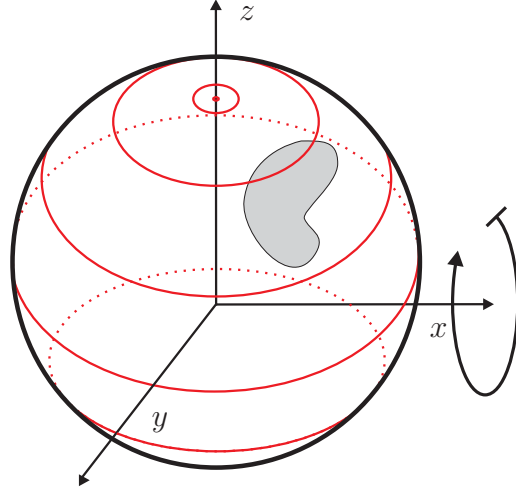
Figure 2.3: Scanning geometry: Circles of latitude on a sphere enclose an object and are rotated around it.

where $(r, \vartheta, \phi) \in \mathbb{R}_{\geq 0} \times [0, \pi] \times [0, 2\pi]$. Further, we use the abbreviation

$$G_\sigma^S(\vartheta, t) := (Sf)(\sigma, R, \vartheta) \tag{2.11}$$

to denote the integrals over circles of latitude of hight $r\cos(\vartheta)$ and the integrated initial pressure by

$$F_\sigma^S(r, \vartheta) = \frac{1}{2\pi} \int_0^{2\pi} f(D_\sigma \cdot \Phi(r, \vartheta, \phi)).$$

The $l-$th Fourier coefficients $F_{\sigma,l}^S$ and $G_{\sigma,l}^S$ of F_σ^S and G_σ^S for the $l-$th Legendre polynomial P_l, satisfy the relation

$$\mathbf{H}_r^l \left\{ F_{\sigma,l}^S \right\}(\omega) = \frac{2}{\pi} \frac{\mathbf{C}_t \left\{ G_{\sigma,l}^S \right\}(\omega)}{\omega^2 j_l(R\omega)}, \tag{2.12}$$

where $\mathbf{H}^l$ denotes the spherical Hankel transform of order l and j_l the $l-$th order spherical Bessel function, which can be found in the appendix of this thesis. The implementation of formula (2.12) is problematic because of the

roots of its denominator. A stable alternative to (2.12) can be derived from a frequency domain formula derived in [55]. This formula is given by

$$\mathbf{H}_r^l\{F_{\sigma,l}^S\}(\omega) = \frac{2}{\pi}\frac{\mathbf{F}_t\{G_{\sigma,l}^S\}(\omega)}{\omega^2\, h_l^{(1)}(R\omega)}, \qquad \omega \in \mathbb{R},\ l \in \mathbb{N}. \tag{2.13}$$

With analogous arguments as in the case of a cylindrical stack of circles we can show the following two stable reconstruction formulas. They are stated by

$$F_\sigma^S(r,\vartheta) = \frac{2}{\pi}\sum_{l\in N}\sum_{n\in\mathbb{N}} \frac{\mathbf{F}_t\left\{G_{\sigma,l}^S\right\}(\omega_{nl})}{\omega_{nl}^2\, h_l^{(1)}(R\omega_{nl})} \frac{j_l(rv_n)P_l(\cos(\vartheta))}{j_{l+1}(R\omega_{nl})^2} \tag{2.14}$$

and

$$F_\sigma^S(r,\vartheta) = \sqrt{\frac{2}{\pi}}\ \sum_{l\in\mathbb{N}}\sum_{n\in\mathbb{N}} \frac{\mathbf{S}_t\left\{tG_\sigma^S\right\}_l(\omega_{nl})j_l(r\omega_{nl})}{\omega_{nl}^2 j_{l+1}(R\omega_{nl})^3}\, P_l(\cos(\vartheta)), \tag{2.15}$$

where in the formulas above the ω_{nl} denote the roots of the function $\omega \mapsto j_l(R\omega)$. The formulas and their proofs are given in section 3.2.4. Moreover, section 3.2.5 contains a convergence result, for the series expansions (2.14) and (2.15) for noisy measurement data.

Once the function F_σ^S is known for all $\sigma \in S^1$ we define, for a fixed $0 < r \leq R$, the map

$$(\sigma,\vartheta) \mapsto F_\sigma^S(r,\vartheta). \tag{2.16}$$

It is not hard to figure out, see figure 2.3, that the map (2.16) consists of the circular means of $f|_{S_r}$ over circles on S_r, which are centered on the great circle that lies in the $yz-$plane. Note that we refer to a center on S_r when we use the phrase "centered on".

In section 3.2.3 a new reconstruction formula for $f|_{S_r}$ from the considered family of circular means is derived. The formula is based on stereographic projection from the north pole on S_r, which maps a circle resp. great circle on S_r onto a circle resp. a line in the plane, see figure 2.4. Therefore the projection of the considered family of circles is the family of circles in the $xy-$plane that are centered on the $y-$axis. For the circular means of a function over the latter family reconstruction formulas are known [6]. They
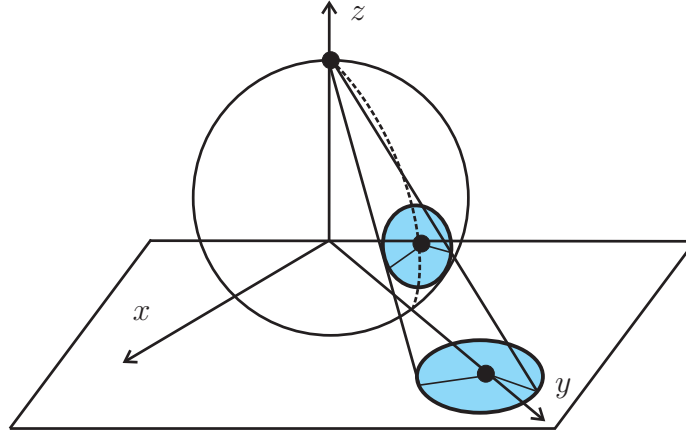
Figure 2.4: Stereographic projection of a circle centered on the great circle in the $yz-$plane (dotted line). The result is a circle in the centered on the $y-$axis in the plane.

can be used to derive new reconstruction formulas for the proposed family on S_r since stereographic projection is a factorable map [45].

In chapter 4 we assume that the initial pressure f is supported in the upper half plane $H = \{\mathbf{x} \in \mathbb{R}^3 : x \geq 0\}$ and that circular means of the acoustic pressure are given in the plane $\mathbb{R}^2 = \partial H$ for two specific families of circles. Our aim is to reconstruct acoustic pressure pointwise from its circular means over these families. Once acoustic pressure is known pointwise we can apply pointwise reconstruction formulas [54, 57, 58].

The first family consists of circles of fixed radius r_d and center $\mathbf{x} \in \mathbb{R}^2$, which is depicted in figure 2.5. Let $G^a(\mathbf{x}, t)$ denote the circular mean, of acoustic pressure $p(\mathbf{x}, t)$, over a circle centered at $\mathbf{x}$. Note that the time variable is omitted in the following to keep our notation simple.

The main result in section 4.1 is based on a Fourier series expansion of the functions G^a and p and the Funk–Hecke theorem which can be found in the appendix. It states that the Fourier coefficients of the measurement data
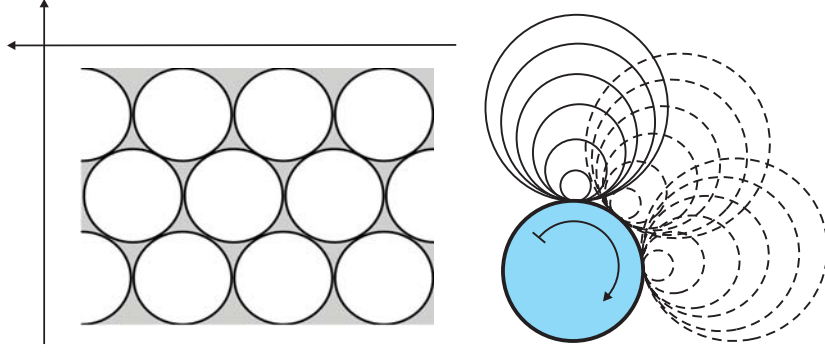
Figure 2.5: Scanning geometries. Left: Circular integrating detectors of fixed radius r_{d} centered in the plane. Right: The family of circles tangential to another circle.

G_λ^a and the pressure p_λ are related by the integral equation

$$G_\lambda^a(R) = \frac{1}{2\pi} \int_{-1}^{1} p_\lambda \left(\sqrt{R^2 + r_{\mathrm{d}}^2 + 2r_{\mathrm{d}}Rt} \right) \frac{T_{|\lambda|}(t)}{\sqrt{1 - t^2}} dt \,, \qquad (2.17)$$

where $R = |\mathbf{x}|$ and T_λ denotes the Tchebychev polynomial of order λ. Equation (2.17) shows that the pressure p can be found from G^a by solving a sequence of one dimensional integral equations. However, since it is difficult to derive an explicit solution of equation (2.17) we solve it numerically for each λ.

The second family consist of circles, see figure 2.5, which are tangential to another (fixed) circle of radius ρ. The circular mean over a circle of this family, that is centered at $\mathbf{x}$ and has radius $r = |\mathbf{x}| - \rho$, is denoted by $G^b(\mathbf{x}, r)$.

In this case it is possible to derive the equation

$$g_\lambda(k) = \int_1^\infty \frac{u_\lambda(k/\sigma)dp}{\sqrt{\sigma^2 - 1}} T_{|\lambda|} \left(\sqrt{\sigma^2 - 1} \right) \frac{1}{\sigma} d\sigma. \qquad (2.18)$$

where $g_\lambda(k) := G_\lambda^b \left(\frac{\rho + \sqrt{k^2 + \rho^2}}{2}, \frac{\sqrt{k^2 + \rho^2} - \rho}{2} \right)$ and $u_\lambda(k) := p_\lambda \left(\sqrt{k^2 + \rho^2} \right)$. Integral equation (2.18) is a convolution product for the Mellin transform $\mathbf{M}$. Applying this transform, we obtain an equation that can be solved for $\mathbf{M}\{u_\lambda\}$ like explained in section 4.2.

In chapter 5 we address the fact that in applications circular integrating detectors are approximated by toroidal shaped optical fibers. Moreover the quantity measured by a toroidal detector, is recorded in an ultrasound detection system. Since this system does not immediately respond to acoustic pressure, blurred temporal measurements are caused.

The results in chapter 5 hold for general measurement configurations of toroidal detectors but we assume here the configuration depicted in figure 2.1 to explain the results. We model approximate measurements, due to erroneous time measurements the detection system and the thickness of a toroidal detector, as

$$(C_{\varphi,\omega} f)(\sigma, z, t) = \varphi *_t \int_{\mathbb{R}^3} \omega(\mathbf{x}(\sigma, z), \mathbf{z}) \, p(\mathbf{z}, t) d\mathbf{z}, \qquad (2.19)$$

where φ denotes the impulse response function of a detection system and ω is a function that models the sensitivity of a toroidal detector. This function depends on the position of a point $\mathbf{z}$ to the center $\mathbf{x}(\sigma, z)$ of the circle $c_{\sigma z}$, which is given by $\alpha \mapsto (r_{\mathrm{d}} \cos(\alpha), r_{\mathrm{d}} \sin(\alpha) + R\breve{\sigma} + ze_3)$.

Usually the inverse C^{-1} of (2.1) is applied to erroneous measurements which results in a blurred version of the initial pressure. The main result in chapter 5 states that the blurred initial pressure is given by

$$\left(C^{-1} C_{\varphi,w}\right)(f) = \Phi * U * f \,,$$

where Φ is given in explicitly in Theorem 5.1 and U is a radial function that is related to the sensitivity function ω of a toroidal detector like explained in chapter 5.

2.1   The limiting case $r_{\mathrm{d}} \to 0$

In TAT with circular detectors an obvious limiting case occurs.

- The radius r_{d} of a circular integrating detector approaches 0.

The results for circular integrating detectors, which were presented in this chapter, provide new reconstruction formulas for pointlike detectors in the limiting case $r_{\mathrm{d}} \to 0$.

Note that formula (2.3) still holds when the stacks of circular detectors are not placed on the circle $R \cdot S^1$, like depicted in figure 2.1, but on an arbitrary point $\mathbf{x} \in \mathbb{R}^2$. Also formula (2.12) holds for any sphere $S_{R,\mathbf{x}}$, centered at an arbitrary point $\mathbf{x} \in \mathbb{R}^3$. Thus, we will use the notations $g_{\mathbf{x}}^C$ and $g_{\mathbf{x}}^S$, for point measurements, in the limiting case for formulas (2.3) and (2.12). According to this, also the integrated initial pressures are denoted by $F_{\mathbf{x}}^C$ and $F_{\mathbf{x}}^S$.

Since $J_0(0) = 1$, reconstruction formula (2.3) still makes sense when $r_\mathrm{d} \to 0$, and the formal limit is

$$\mathbf{H}_r \left\{ \mathbf{F}_z \left\{ F_{\mathbf{x}}^C \right\} \right\} (k, v) = \frac{2}{\pi} \frac{\mathbf{C}_t \left\{ \mathbf{F}_z \left\{ g_{\mathbf{x}}^C \right\} \right\} (k, \sqrt{k^2 + v^2})}{\sqrt{k^2 + v^2}}, \tag{2.20}$$

which is very similar to formula (1.5). However, the meaning of formula (2.20) is quite different. It establishes a relation between the circular means $F_{\mathbf{x}}^C$, of f, and pointwise data $g_{\mathbf{x}}^C$ on the line $\mathbb{R}e_3 + R\mathbf{x}$. If $\mathbf{x} \in R \cdot S^1$ we obtain a new reconstruction formula for point detectors on a cylindrical surface, where f has to be recovered from $F_{\mathbf{x}}^C$ by the reconstruction procedure described in remark 3.1.

If $\mathbf{x} = xe_1$ lies on the x−axis $F_{\mathbf{x}}^C(r, z)$ is the integral over the circle, centered at $(x, 0, z)$, with radius r that is perpendicular to the xz−plane. Thus, for z fixed, the map

$$(r, x) \mapsto F_{xe_1}(r, z)$$

is the circular mean transform of $f|_{\mathbb{R} \times \{z\}}$ over circles centered on the line $\mathbb{R}e_1 + ze_3$ with radius r. A reconstruction formula, for such a family of circles, can be found in [6]. Applying these formula in each pane $\mathbb{R} \times \{z\}$ yields the function f.

In the limiting case $R \to 0$ of a sphere $S_{R,\mathbf{x}}$ we obtain the relation

$$\mathbf{H}_r^0 \left\{ F_{\mathbf{x}}^S \right\}_0 (\omega) = \frac{2}{\pi} \frac{\mathbf{C}_t \left\{ g_{\mathbf{x}}^S \right\}_0 (\omega)}{\omega^2}, \tag{2.21}$$

between 0−th order Legendre coefficients from formula (2.12). However, we do not obtain a relation for higher order coefficients of $F_{\mathbf{x}}^S$ since the pointwise data $g_{\mathbf{x}}^S$ do not depend on ϑ, which implies that $\mathbf{C}_t \left\{ g_{\mathbf{x}}^S \right\}_l (\omega) = 0$ for $l > 0$. Moreover, note that

$$F_{\mathbf{x},0}^S = \int_0^\pi \left(\int_0^{2\pi} f(\Phi(r, \vartheta, \phi)) d\phi \right) \sin(\vartheta) d\vartheta = \frac{1}{r^2} M(f)(\mathbf{x}, r), \tag{2.22}$$

where $M(f)(\mathbf{x}, r)$ denotes the spherical mean of the initial pressure. Moreover, since $g_{\mathbf{x},0}^S(t) = g_{\mathbf{x}}^S(t) \int_0^\pi \sin(\vartheta) d\vartheta$ we can rewrite (2.21) as

$$\mathbf{H}_r^0 \left\{ r^{-2} M(f)(\mathbf{x}, \cdot) \right\} (\omega) = \frac{4}{\pi} \frac{\mathbf{C}_t \left\{ g_{\mathbf{x}} \right\}(\omega)}{\omega^2}. \tag{2.23}$$

The last expression establishes a new relationship between pointwise measurements and the spherical means $M(f)$.

The series expansion formulas (2.15) and (2.6) assume that the functions $F_{\mathbf{x}}^C(\cdot, z)$ resp. $F_{\mathbf{x}}^S(\cdot, \vartheta)$ are supported in the intervals $(0, r_{\mathrm{d}})$ resp. $(0, R)$. Clearly, this assumption can not be satisfied in the limiting case when r_{d} and R approach 0. However, for a r_1 large enough we can expand the functions $\mathbf{F}_z \left\{ F_{\mathbf{x}}^C \right\}(k, \cdot)$ and $F_0^S(\cdot) = r^{-2} M(f)(\mathbf{x}, \cdot)$ into Fourier Bessel series, given by

$$\mathbf{F}_z \left\{ F_{\mathbf{x}}^C \right\}(k, r) = \frac{2}{r_1^2} \sum_{n \in \mathbb{N}} \mathbf{H}_r \left\{ \mathbf{F}_z \left\{ F_{\mathbf{x}}^C \right\} \right\}(k, \tilde{v}_n) \frac{J_0(r\tilde{v}_n)}{J_1(r_1 \tilde{v}_n)^2}, \tag{2.24}$$

where $(\tilde{v}_n)_{n \in \mathbb{N}}$ denote the zeros of $v \mapsto J_0(r_1 \tilde{v})$ and

$$r^{-2} M(f)(\mathbf{x}, r) = \sum_{n \in \mathbb{N}} \mathbf{H}_r^0 \left\{ r^{-2} M(f)(\mathbf{x}, \cdot) \right\}(\bar{v}_n) \frac{j_0(r\bar{v}_n)}{j_1(r_1 \bar{v}_n)^2} \tag{2.25}$$

where $(\bar{v}_n)_{n \in \mathbb{N}}$ denote the zeros of $v \mapsto j_0(r_1 \bar{v})$. Together with formulas (2.20) and (2.23) we obtain the new series expansion formulas

$$\mathbf{F}_z \left\{ F_\sigma \right\}(k, r) = \frac{2}{r_1^2} \sum_{n \in \mathbb{N}} \mathbf{H}_r \left\{ \mathbf{F}_z \left\{ F_\sigma \right\} \right\}(k, \tilde{v}_n) \frac{J_0(r\tilde{v}_n)}{J_1(r_1 \tilde{v}_n)^2}, \tag{2.26}$$

and

$$r^{-2} M(f)(\mathbf{x}, r) = \frac{4}{\pi} \sum_{n \in \mathbb{N}} \frac{\mathbf{C}_t \left\{ g_{\mathbf{x}} \right\}(\omega)}{w^2} \frac{j_0(r\bar{v}_n)}{j_1(r_1 \bar{v}_n)^2}, \tag{2.27}$$

where J_1 and j_1 denote the Bessel and spherical Bessel functions, which can be found in the appendix.

Unfortunately, formulas (2.5), (2.15), (2.6) and (2.7) do not yield new reconstruction formulas since their denominator is not bounded for $r_{\mathrm{d}} \to 0$.

Chapter 3

Two step reconstruction Algorithms

This chapter contains detailed derivations and explanations of the formulas which were derived for the experimental setups depicted in figures 2.3 and 2.1. Both formulas utilize the effect that the three dimensional wave equation in cylindrical or spherical coordinates reduces to a two dimensional wave equation when it is integrated over its azimuthal angle. In both cases the three dimensional reconstruction process requires the solution of a sequence of two dimensional inverse problems for the two dimensional wave equation.

In the following sections the notation slightly differs from the notation that has been used in chapter 1. More precisely, we omit the upper indices S and C that were used in chapter 1 to distinguish the measurement configurations described by the operators 2.1 and 2.9. In the following it will be clear which measurement configuration is investigated and thus the simplified notation does not cause confusion.

3.1 Circular Integrating Detectors in Cylindrical geometry

We consider the TAT with circular integrating detectors for the setup depicted in figure 2.1. Acoustic pressure p satisfies the Cauchy problem (1.1)-(1.3).

further, we assume here that f is supported in the cylinder $B_R(0) \times \mathbb{R}$, where R is a fixed positive number and where $p(x, t)$ denotes the unique solution of (1.1)-(1.3).

For $\sigma \in S^1$, we define the integral of acoustic pressure over a circle as

$$P_\sigma(z, r, t) := \frac{1}{2\pi} \int_0^{2\pi} p(\boldsymbol{\Phi}_\sigma(z, r, \alpha), t) \, d\alpha , \quad (z, r, t) \in \mathbb{R} \times (0, \infty)^2 , \quad (3.1)$$

where

$$\boldsymbol{\Phi}_\sigma : \quad \mathbb{R} \times (0, \infty) \times [0, 2\pi] \to \mathbb{R}^3$$

$$(z, r, \alpha) \mapsto (R\sigma, 0) + (r \cos(\alpha), r \sin(\alpha), z)^T . \quad (3.2)$$

With terminology the integrated initial pressure and the measurement data are given by

$$F_\sigma(z, r) := \frac{1}{2\pi} \int_0^{2\pi} f(\boldsymbol{\Phi}_\sigma(z, r, \alpha)) \, d\alpha , \quad (z, r) \in \mathbb{R} \times (0, \infty) , \quad (3.3)$$

$$G_\sigma(z, t) := P_\sigma(z, r_{\mathrm{d}}, t) , \quad\quad\quad (\sigma, z, t) \in S^1 \times \mathbb{R} \times (0, \infty) \quad (3.4)$$

where

This notation is consistent with the notation introduced in chapter 1.

Our goal is to recover the unknown initial data f from measured data $(G_\sigma)_{\sigma \in S^1}$.

3.1.1   Two Stage Reconstruction

Reconstruction with circular integrating detectors is based on the following reduction to the axial symmetric wave equation:

Proposition 3.1. *Let $f \in C_0^\infty(B_R(0) \times \mathbb{R})$ and define P_σ and F_σ, $\sigma \in S^1$ by (3.1), (3.3). Then P_σ satisfies the axial symmetric wave equation*

$$\partial_t^2 P_\sigma(z, r, t) = \left(r^{-1} \partial_r r \partial_r + \partial_z^2 \right) P_\sigma(z, r, t) , \quad (z, r, t) \in \mathbb{R} \times (0, \infty)^2 , \quad (3.5)$$

$$P_\sigma(z, r, 0) = F_\sigma(z, r) , \quad\quad\quad\quad (z, r) \in \mathbb{R} \times (0, \infty) , \quad (3.6)$$

$$\partial_t P_\sigma(z, r, 0) = 0 , \quad\quad\quad\quad\quad (z, r) \in \mathbb{R} \times (0, \infty) . \quad (3.7)$$

Moreover P_σ remains bounded as $r \to 0$.

Proof. Equations (3.6), (3.7) and the boundedness of P_σ for $r \to 0$ immediately follow from (1.2), (1.3), the requirement that $f \in C_0^\infty(\Omega)$ and the definitions of P_σ and F_σ. Moreover, in cylindrical coordinates the Laplace operator is given by the expression

$$\Delta = r^{-1}\partial_r r \partial_r + \partial_z^2 + r^{-2}\partial_\alpha^2.$$

Integrating the equation $\Delta p = \partial_t^2 p$ with respect to α gives (3.5). $\square$

Note that (3.5)-(3.7) is uniquely solvable if we require that its solution remains bounded as $r \to 0$.

Remark 3.1. Proposition 3.1 is the basis of the following two-stage procedure which reconstructs the initial pressure f in (1.1)-(1.3) from the data $(G_\sigma)_{\sigma \in S^1}$:

(i) For $\sigma \in S^1$ (fixed position of the stack of circles) we determine the initial pressure F_σ of (3.5)-(3.7) using the data G_σ.

Repeating this procedure for every σ, we obtain a family of functions F_σ, $\sigma \in S^1$, corresponding to averages over circles centered on $\partial(B_R(0) \times \mathbb{R})$.

(ii) Next we observe that for fixed $z = z_0$, the function

$$(\sigma, r) \mapsto F_\sigma(z_0, r)$$

is the circular mean transform of $f|_{\{z=z_0\}}$ with centers on a circle. For the circular mean transform stable analytic inversion formulas have been discovered recently [3, 16, 18, 35, 36]. Exemplarily, one of the formulas in [16, Theorem 1.1] reads

$$f(\mathbf{x}', z_0) = \frac{1}{2\pi R} \int_{S^1} \left(\int_0^{2R} (\partial_r r \partial_r F_\sigma)(z_0, r) \log \left| r^2 - |\mathbf{x}' - R\sigma|^2 \right| \, dr \right) d\sigma,$$

(3.8)

where $\mathbf{x}'$ denotes the coordinates in the plane $\mathbb{R}^2 \times \{z_0\}$.

The key task for recovering f is to derive stable and fast algorithms to reconstruct the initial data in (3.5)-(3.7) from measurement data G_σ. A possible reconstruction method is based on time reversal (back-propagation)

similar to [12, 25]. However, the degeneration of $r^{-1}\partial_r r \partial_r$ at $r = 0$ and the finite hight of the stack of circular integrating detectors may cause difficulties in such procedures. The inversion approach in this paper is based on analytic inversion formulas for reconstructing F_σ.

3.1.2   Exact Inversion Formula

The formula, which we derive, describes a relationship between several integral transforms of the measurement data G_σ and F_σ. The integral transforms, and the meaning of the subscripts, can be found in the appendix of this thesis.

Proposition 3.2. *Let $f \in C_0^\infty(B_R(0) \times \mathbb{R})$ and define $F_\sigma(z, r)$ and $G_\sigma(z, t)$ by (3.3), (3.4). Then the relation*

$$\mathbf{H}_r\left\{\mathbf{F}_z\left\{F_\sigma\right\}\right\}(k, v) = \frac{2}{\pi}\frac{\mathbf{C}_t\left\{\mathbf{F}_z\left\{G_\sigma\right\}\right\}\left(k, \sqrt{k^2 + v^2}\right)}{J_0(r_{\mathrm{d}}v)\sqrt{k^2 + v^2}} \qquad (3.9)$$

holds whenever $J_0(r_{\mathrm{d}}v) \neq 0$.

Proof. The zero order Bessel function J_0 is an Eigenfunction of the operator $r^{-1}\partial_r r \partial_r$ with eigenvalue -1. Then the function $r \mapsto J_0(rv)$ is an eigenfunction of the same operator with eigenvalue $-v^2$. To appreciate this denote by $\hat{J}(r) = J_0(rv)$ and compute

$$\left(r^{-1}\partial_r r \partial_r\right)\hat{J}(r) = r^{-1}\hat{J}'(r) + \hat{J}''(r),$$

where the prime denotes the derivative with respect to r. Using the relations $\hat{J}'(r) = vJ_0'(rv)$, $\hat{J}''(r) = v^2 J_0''(rv)$ and substitute $u = rv$ we have

$$r^{-1}vJ_0'(rv) + v^2 J_0''(rv) = v^2\left(u^{-1}\partial_u J_0(u) + \partial_u^2 J_0(u)\right)$$

$$= -v^2 J_0(u) = -v^2 J_0(rv).$$

Further, separation of variables shows that the functions

$$(z, r, t) \mapsto e^{ikz}\cos\left(t\sqrt{k^2 + v^2}\right)J_0(rv), \qquad (k, v) \in \mathbb{R} \times (0, \infty),$$

solve (3.5), (3.7). Since the system (3.5)-(3.7) is linear a general solution can formally be written as

$$P_\sigma(z, r, t) := \frac{1}{2\pi}\int_{\mathbb{R}}\int_0^\infty \bar{F}(k, v)e^{ikz}J_0(rv)\cos\left(t\sqrt{k^2 + v^2}\right)vdvdk. \qquad (3.10)$$

The latter integral converges if we at least assume that $\bar{F}$ is contained in $L^1(\mathbb{R} \times \mathbb{R}_{>0}) \cap \mathcal{C}^\infty(\mathbb{R} \times \mathbb{R}_{>0})$. In order to obtain a solution to our problem we set $t = 0$ in equation (3.10) which shows that the initial condition F_σ of the Cauchy Problem (3.5)-(3.7) is the inverse Hankel and Fourier transform of $\bar{F}$. Since we can apply the Fourier and Hankel inversion theorems in the considered function spaces we conclude that equation (3.10) is a solution of the system (3.5)-(3.7) for $\bar{F}(k, v) := \mathbf{H}_r \{\mathbf{F}_z \{F_\sigma\}\} (k, v)$. It is easy to check that the substitution $\omega = \sqrt{k^2 + v^2}$ implies the identity $\omega d\omega = v dv$, which can be used to rewrite (3.10) as

$$P_\sigma(z, r_\mathrm{d}, t) =$$
$$G_\sigma(z, t) = \frac{1}{2\pi} \int_\mathbb{R} \left(\int_{|k|}^\infty J_0\big(r_\mathrm{d}\sqrt{\omega^2 - k^2}\big) \omega \bar{F}\big(k, \sqrt{\omega^2 - k^2}\big) \cos(\omega t) d\omega \right) e^{ikz} dk, \tag{3.11}$$

where we set $r = r_\mathrm{d}$. The inversion formulas for the Fourier and Cosine transforms now imply that

$$\mathbf{C}_t \{\mathbf{F}_z \{G_\sigma\}\} (k, \omega) = \frac{\pi}{2} \begin{cases} J_0\big(r_\mathrm{d}\sqrt{\omega^2 - k^2}\big) \omega \bar{F}\big(k, \sqrt{\omega^2 - k^2}\big), & \text{if } \omega > k, \\ 0, & \text{otherwise}. \end{cases}$$

Solving the last equation for $\bar{F}$ shows (3.9). $\square$

Proposition 3.2 leads to an algorithmic procedure for the reconstruction of F_σ from the data G_σ:

1. Apply the Fourier and cosine transform to the data G_σ.

2. Determine $\mathbf{H}_r \{\mathbf{F}_z \{F_\sigma\}\}$ from $\mathbf{C}_t \{\mathbf{F}_z \{G_\sigma\}\}$ according to (3.9)

3. Apply the inverse Fourier and Hankel transforms to obtain

$$F_\sigma(z, r) = \frac{1}{2\pi} \int_\mathbb{R} \int_0^\infty \mathbf{H}_r \{\mathbf{F}_z \{F_\sigma\}\} (k, v) J_0(rv) e^{ikz} \, v dv dk \,.$$

Remark 3.2 (Instability of (3.9)). Inversion formula (3.9) is not defined when $J_0(r_\mathrm{d}v)$ equals 0. From the proof of the above theorem it is clear that for exact data

$$\mathbf{C}_t\{\mathbf{F}_z\{G_\sigma\}\}\big(k, \sqrt{v_n^2 + k^2}\big) = 0\,, \qquad n \in \mathbb{N}\,, \tag{3.12}$$

for the zeros $(v_n)_{n \in \mathbb{N}}$ of the zero order Bessel function $r \mapsto J_0(r_{\mathrm{d}} v)$. In practice, however, only noisy (approximately measured) data $G_\sigma^\delta \simeq G_\sigma$ are available. In this case equation (3.12) is not necessarily satisfied and we have

$$\mathbf{C}_t\{\mathbf{F}_z\{G_\sigma^\delta\}\}\big(k, \sqrt{v_n^2 + k^2}\big) \neq 0 \,.$$

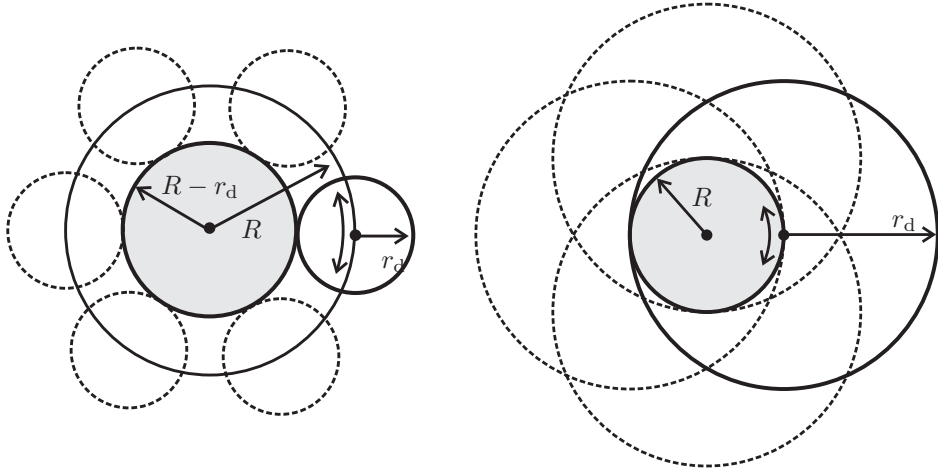It is therefore difficult to evaluate the quotient in (3.9) in a stable way in practice.

Figure 3.1: Cross section of experimental buildup when $r_{\mathrm{d}} < R$ (left) and $r_{\mathrm{d}} \geq 2R$ (right). In both cases the object has to be supported in the gray disc.

We can overcome this difficulty when we place circles around the object which are large enough to enclose it. The cases when the measuring circles are strictly outside the object or enclosing it are the only two situations that can be realized in practical applications and are summarized, see Figure 3.1, as follows:

(i) The stack of circles is strictly outside the object. In this case $r_{\mathrm{d}} < R$ and $\mathrm{supp}(f) \subset B_{R-r_{\mathrm{d}}}(0) \times \mathbb{R}$.

(ii) The object is enclosed in the stack of circles. In this case $r_{\mathrm{d}} \geq 2R$.

For the case $r_{\mathrm{d}} \geq 2R$ we will provide two stable formulas based on expansions of F_σ into Fourier Bessel series. Unfortunately, when $r_{\mathrm{d}} < R$ we can not derive such expansions since in this case the function $r \mapsto \mathbf{F}\{F_\sigma\}(k, r)$ is not supported in the interval $(0, r_{\mathrm{d}})$ and thus it cannot be expanded into a Fourier Bessel series which is crucial in the proofs of Theorems 3.1 and 3.2. Although no expansion formula is available we will show reconstructions based on an implementation of formula (3.9) in chapter 6. However, in the limiting case $r_{\mathrm{d}} \ll R$ a stable reconstruction formula is obtained, compare with Remark 3.5 below.

3.1.3 Stable Inversion Formulas

In the following we fix $\sigma \in S^1$, define F_σ, G_σ by equations (3.6) and (3.4) and let $(v_n)_{n \in \mathbb{N}}$ denote the zeros of the function $v \mapsto J_0(r_{\mathrm{d}} v)$. A treaties and a table of the zeros of Bessel functions can be found in [9]. In the following series expansion it is essential that Bessel functions of different order do not have common zeros.

Our first stable inversion formula is as follows:

Theorem 3.1 (The D'Hospital trick). *Assume $r_{\mathrm{d}} \geq 2R$. Then*

$$F_\sigma(z, r) = \frac{2}{\pi^2 r_{\mathrm{d}}^3} \int_{\mathbb{R}} \left(\sum_{n \in \mathbb{N}} \frac{\mathbf{S}_t \left\{ t\, \mathbf{F}_z \left\{ G_\sigma \right\} \right\} \left(k, \sqrt{k^2 + v_n^2} \right) v_n}{k^2 + v_n^2} \frac{J_0(r v_n)}{J_1(r_{\mathrm{d}} v_n)^3} \right) e^{ikz} dk$$

(3.13)

for any $(z, r) \in \mathbb{R} \times (0, \infty)$.

Proof. The assumptions $f \in C_0^\infty(B_R(0))$ and $r_{\mathrm{d}} \geq 2R$ imply that $\mathbf{F}_z\{F_\sigma\}(k, \cdot)$ is compactly supported in $(0, r_{\mathrm{d}})$ like it is depicted in figure 3.2. It can therefore be expanded into a Fourier Bessel series [52]

$$\mathbf{F}_z \left\{ F_\sigma \right\}(k, r) = \frac{2}{r_{\mathrm{d}}^2} \sum_{n \in \mathbb{N}} \mathbf{H}_r \left\{ \mathbf{F}_z \left\{ F_\sigma \right\} \right\}(k, v_n) \frac{J_0(r v_n)}{J_1(r_{\mathrm{d}} v_n)^2} .$$

(3.14)

Note that the latter formula holds pointwise since the function F_σ is continues and compactly supported. According to (3.9) we have

$$\mathbf{H}_r \left\{ \mathbf{F}_z \left\{ F_\sigma \right\} \right\}(k, v) = \frac{2}{\pi} \frac{\mathbf{C}_t \left\{ \mathbf{F}_z \left\{ G_\sigma \right\} \right\} \left(k, \sqrt{k^2 + v^2} \right)}{J_0(r_{\mathrm{d}} v) \sqrt{k^2 + v^2}} , \qquad v \notin \{ v_n : n \in \mathbb{N} \} .$$

Applying the rule of D'Hospital gives

$$
\begin{aligned}
\mathbf{H}_r\left\{\mathbf{F}_z\left\{F_\sigma\right\}\right\}(k, v_n) &= \frac{2}{\pi} \lim_{v \to v_n} \frac{\partial/\partial v\left[\mathbf{C}_t\left\{\mathbf{F}_z\left\{G_\sigma\right\}\right\}\left(k, \sqrt{k^2+v^2}\right)\right]}{\partial/\partial v\left[J_0(r_{\mathrm{d}}v)\sqrt{k^2+v^2}\right]} \\
&= \frac{2}{\pi} \lim_{v \to v_n} \frac{\mathbf{S}_t\left\{t\,\mathbf{F}_z\left\{G_\sigma\right\}\right\}\left(k, \sqrt{k^2+v^2}\right)\frac{v}{\sqrt{k^2+v^2}}}{J_1(r_{\mathrm{d}}v)r_{\mathrm{d}}\sqrt{k^2+v^2}} \\
&= \frac{2}{\pi r_{\mathrm{d}}} \frac{\mathbf{S}_t\left\{t\,\mathbf{F}_z\left\{G_\sigma\right\}\right\}\left(k, \sqrt{k^2+v_n^2}\right)v_n}{J_1(r_{\mathrm{d}}v_n)\left(k^2+v_n^2\right)} .
\end{aligned}
\tag{3.15}
$$

Inserting (3.15) in (3.14) and using the Fourier inversion formula shows (3.13). $\qquad\square$
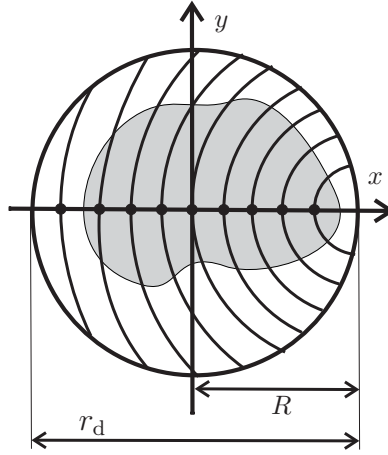

Figure 3.2: Since f is supported inside $B_R(0)$ the values of the function $F_{e_1}(z, \cdot)$ vanish for $r > r_{\mathrm{d}}$. The gray shaded area illustrates the initial density f restricted to a horizontal plane.

Remark 3.3. [Stability of (3.13)] From the asymptotic approximation (see [1])

$$
J_m(r_{\mathrm{d}}v) \simeq \sqrt{\frac{2}{\pi x}} \cos\left(r_{\mathrm{d}}v - \frac{m\pi}{2} - \frac{\pi}{4}\right), \quad \text{for } v \to \infty,
$$

3.1. CYLINDRICAL GEOMETRY

of the m-th order Bessel function it follows that the roots of $v \mapsto J_0(r_{\mathrm{d}}v)$ approximately satisfy the equation

$$r_{\mathrm{d}}v_n - \pi/4 = (2n+1)\pi/2.$$

Thus

$$v_n \simeq \frac{\pi(n+3/4)}{r_{\mathrm{d}}}, \quad |J_1(r_{\mathrm{d}}v_n)| \simeq \sqrt{\frac{2}{\pi r_{\mathrm{d}}v_n}}, \quad \text{for } n \to \infty.$$

Moreover the summands in (3.13) take the asymptotic form

$$\left| \mathbf{S}_t\left\{t\,\mathbf{F}_z\left\{G_\sigma\right\}\right\}\left(k,\sqrt{k^2+v_n^2}\right)\frac{v_n}{k^2+v_n^2}\frac{J_0(rv_n)}{J_1(r_{\mathrm{d}}v_n)^3} \right|$$

$$\simeq \left| \mathbf{S}_t\left\{t\,\mathbf{F}_z\left\{G_\sigma\right\}\right\}\left(k,\sqrt{k^2+v_n^2}\right) \right| \frac{1}{v_n} \frac{\left|\cos\left(v_n-\frac{\pi}{4}\right)\right|(2/(\pi r v_n))^{1/2}}{(2/(\pi r_{\mathrm{d}}v_n))^{3/2}}$$

$$\leq \frac{r^{1/2}}{4r_{\mathrm{d}}^{3/2}}\left| \mathbf{S}_t\left\{t\,\mathbf{F}_z\left\{G_\sigma\right\}\right\}\left(k,\sqrt{k^2+v_n^2}\right) \right|.$$

Consequently, the terms that do not depend on the data G_σ are bounded, and (3.13) can be implemented in stable way.

In the sequel we derive an additional inversion formula that circumvents the division by zero problem. In fact, our formula will be a consequence of the following result derived in [60].

Proposition 3.3. *Let p denote the unique solution of (1.1)-(1.3) and let f_σ^m and g_σ^m denote the Fourier coefficients of $f(\mathbf{\Phi}_\sigma(z,r,\alpha))$ and*

$$g_\sigma(\alpha,z,t) := \begin{cases} p(\mathbf{\Phi}_\sigma(z,r,\alpha),t), & \text{for } t > 0, \\ 0, & \text{otherwise}, \end{cases}$$

with respect to α. Then

$$\mathbf{H}_r\left\{\mathbf{F}_z\left\{f_\sigma^m\right\}\right\}(k,v) = \frac{2}{\pi}\frac{\mathbf{F}_t\left\{\mathbf{F}_z\left\{g_\sigma^m\right\}\right\}\left(k,\sqrt{k^2+v^2}\right)}{H_m^{(2)}(r_{\mathrm{d}}v)\sqrt{k^2+v^2}}, \qquad (k,v) \in \mathbb{R}\times(0,\infty),$$

$$(3.16)$$

with $H_m^{(2)}$ denoting the m-th order second kind Hankel function.

Now the second stable inversion formula can be stated as follows:

Theorem 3.2. *Assume* $r_{\mathrm{d}} \geq 2R$. *Then*

$$F_\sigma(z,r) = \frac{2}{\pi^2 r_{\mathrm{d}}^2} \int_{\mathbb{R}} \left(\sum_{n \in \mathbb{N}} \frac{\mathbf{F}_t \left\{ \mathbf{F}_z \left\{ G_\sigma \right\} \right\} (k, \sqrt{k^2 + v_n^2})}{H_0^{(2)}(r_{\mathrm{d}} v_n) \sqrt{k^2 + v_n^2}} \frac{J_0(r v_n)}{J_1(r_{\mathrm{d}} v_n)^2} \right) e^{ikz} dk \,. \tag{3.17}$$

Here G_σ *is extended by* $G_\sigma(z,t) = 0$ *for* $t < 0$.

Proof. We use again the Fourier–Bessel series (3.14) of proof of Theorem 3.1. Recalling the definitions of F_σ, G_σ and the Fourier coefficients f_σ^m, g_σ^m one notices that $F_\sigma = f_\sigma^0$, $G_\sigma = g_\sigma^0$. Therefore (3.16) for $m = 0$ implies

$$\mathbf{H}_r \left\{ \mathbf{F}_z \left\{ F_\sigma \right\} \right\} (k,v) = \frac{2}{\pi} \frac{\mathbf{F}_t \left\{ \mathbf{F}_z \left\{ G_\sigma \right\} \right\} (k, \sqrt{k^2 + v^2})}{H_0^{(2)}(r_{\mathrm{d}} v) \sqrt{k^2 + v^2}}, \qquad (k,v) \in \mathbb{R} \times (0, \infty)\,. \tag{3.18}$$

Inserting (3.18) in (3.14) and using the Fourier inversion formula shows (3.17). ☐

Equation (3.18) is quite similar to (3.9). However, in the denominator in (3.18) the zero order second kind Hankel function appears (instead of the zero order Bessel function) which cannot be zero for a finite argument [1]. Moreover, the asymptotic expansion of the Bessel and the second kind Hankel function show that the summands in (3.17) that do not depend on the data G_σ remain bounded as $n \to \infty$.

Remark 3.4. The derivation of (3.16) is based on the following Green function expansion in cylindrical coordinates [60]

$$\frac{e^{-i\omega|\mathbf{\Phi}_\sigma(z,r,\alpha) - \mathbf{\Phi}_\sigma(z_0, r_{\mathrm{d}}, \alpha_0)|}}{|\mathbf{\Phi}_\sigma(z,r,\alpha) - \mathbf{\Phi}_\sigma(z_0, r_{\mathrm{d}}, \alpha_0)|}$$

$$= \frac{-i\pi}{2} \int_{\mathbb{R}} \left(\sum_{m \in \mathbb{Z}} A_m(vr, vr_{\mathrm{d}}) e^{-im(\alpha - \alpha_0)} \right) e^{-i\omega(z - z_0)} dz\,, \quad (3.19)$$

with $v = \text{sign}(\omega)\sqrt{|\omega^2 - k^2|}$,

$$A_m(vr, vr_{\mathrm{d}}) = \begin{cases} H_m^{(2)}(vr_{\mathrm{d}})J_m(vr), & \text{if } \omega^2 > k^2, \\ 2i/\pi\, K_m(|v|\, r_{\mathrm{d}})I_m(|v|\, r), & \text{otherwise,} \end{cases}$$

and I_m, K_m denoting the m-th order modified Bessel functions of first and second kind, respectively. Here its is assumed that $r_{\mathrm{d}} > r$.

Interchanging the roles of r and r_{d} implies that for $r_{\mathrm{d}} > r$ the Green function expansion (3.19) holds with

$$A_m(vr, vr_{\mathrm{d}}) = \begin{cases} J_m(vr_{\mathrm{d}})H_m^{(2)}(vr), & \text{if } \omega^2 > k^2, \\ 2i/\pi\, I_m(|v|\, r_{\mathrm{d}})K_m(|v|\, r), & \text{otherwise.} \end{cases}$$

Similar to the proof of (3.16) in [60] this leads to a formula for reconstructing F_σ in the case $r_{\mathrm{d}} \leq 2R$, however again an unstable one with $J_0(vr_{\mathrm{d}})$ in the denominator.
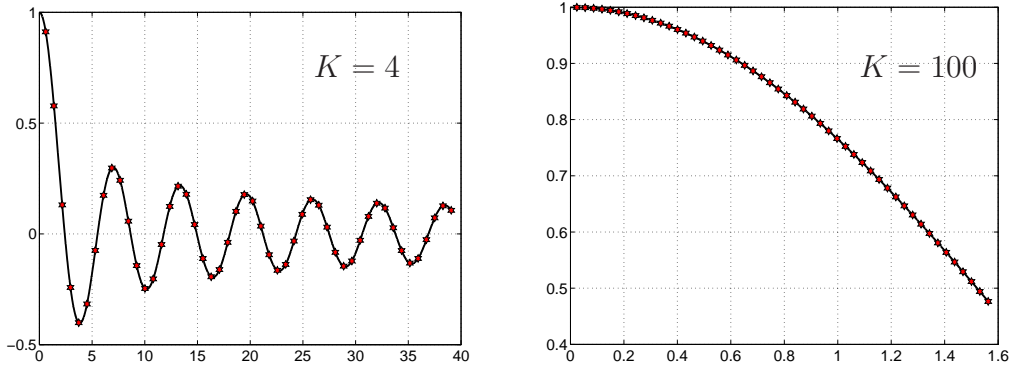

Figure 3.3: The first 50 denominators $J_0(r_{\mathrm{d}}v_n/K)$ in (3.22) for $K = 4$ (left) and $K = 100$ (right).

Remark 3.5. Suppose that $r_{\mathrm{d}} < R$ and that f is supported in $B_{R-r_{\mathrm{d}}}(0) \times \mathbb{R}$. For $r_1 \geq 2R - r_{\mathrm{d}}$ let $(\tilde{v}_n)_{n\in\mathbb{N}}$ denote the zeros of $v \mapsto J_0(r_1\tilde{v})$. Then one can expand $\mathbf{F}_z\{F_\sigma\}(k,\cdot)$ in a Fourier Bessel series (see [52])

$$\mathbf{F}_z\{F_\sigma\}(k,r) = \frac{2}{r_1^2}\sum_{n\in\mathbb{N}}\mathbf{H}_r\{\mathbf{F}_z\{F_\sigma\}\}(k,\tilde{v}_n)\frac{J_0(r\tilde{v}_n)}{J_1(r_1\tilde{v}_n)^2}, \qquad (k,r)\in\mathbb{R}\times(0,\infty).$$

$$(3.20)$$

According to (3.9) we have

$$\mathbf{H}_r \left\{ \mathbf{F}_z \left\{ F_\sigma \right\} \right\} (k, v) = \frac{2}{\pi} \frac{\mathbf{C}_t \left\{ \mathbf{F}_z \left\{ G_\sigma \right\} \right\} (k, \sqrt{k^2 + v^2})}{J_0(r_{\mathrm{d}} v) \sqrt{k^2 + v^2}} \qquad v \notin \left\{ v_n : n \in \mathbb{N} \right\} .$$

$$(3.21)$$

If we assume that r_1 is a integer multiple of r_{d}, i.e., $r_1 = K r_{\mathrm{d}}$, then $\tilde{v}_n = v_n/K \notin \left\{ v_m : m \in \mathbb{N} \right\}$ for any $n \in \mathbb{N}$. Therefore, inserting (3.21) in (3.20) yields

$$\mathbf{F}_z \left\{ F_\sigma \right\} (k, r) = \frac{2}{\pi^2 r_1^2} \sum_{n \in \mathbb{N}} \frac{\mathbf{C}_t \left\{ \mathbf{F}_z \left\{ G_\sigma \right\} \right\} (k, \sqrt{k^2 + \tilde{v}_n^2})}{J_0(r_{\mathrm{d}} \tilde{v}_n) \sqrt{k^2 + \tilde{v}_n^2}} \frac{J_0(r \tilde{v}_n)}{J_1(r_1 \tilde{v}_n)^2} \qquad (3.22)$$

In general, (3.22) is a again sensible to noise when $\tilde{v}_n$ gets close to a zero of $J_0(r_{\mathrm{d}} v)$.

In the limiting case $r_{\mathrm{d}} \ll R$ and for n not too large, the denominators $J_0(r_1 \tilde{v}_n)$ are well bounded from below (see right image in Figure 3.3). In this case, truncating (3.22) at a certain index n_0 leads to a stable inversion formula. In particular, for $r_{\mathrm{d}} = 0$ one obtains

$$\mathbf{F}_z \left\{ F_\sigma \right\} (k, r) = \frac{2}{\pi^2 r_1^2} \sum_{n \in \mathbb{N}} \frac{\mathbf{C}_t \left\{ \mathbf{F}_z \left\{ G_\sigma \right\} \right\} (k, \sqrt{k^2 + \tilde{v}_n^2})}{\sqrt{k^2 + \tilde{v}_n^2}} \frac{J_0(r \tilde{v}_n)}{J_1(r_1 \tilde{v}_n)^2} \qquad (3.23)$$

for every $r_1 \geq 2R$. Together with (3.8) this provides a novel inversion formula for TAT using point-like detectors on a cylindrical recording surface.

3.2   Circular Integrating Detectors in spherical geometry

In this section we assume that the circular means over a two dimensional family of circles of latitude on a sphere, like depicted in figure 2.3, are given. Collecting measurements with circular detectors on a sphere might be particulary useful to image a small object that is enclosed by it. In TAT, the sound that is emitted by an enclosed object, passes through the boundary of the sphere in finite time. Thus no shadowing effects in reconstructions due to missing data are expected.

Let acoustic pressure p again satisfy equations (1.1)-(1.3) and assume that initial pressure f is supported inside the ball $B_R(0)$, which is centered at the origin of $\mathbb{R}^3$ and has radius R. In this section we will derive reconstruction formulas similar to (3.9) and (3.13).

For $\sigma \in S^1$, define

$$P_\sigma(r, \vartheta, t) := \frac{1}{2\pi} \int_0^{2\pi} p(\boldsymbol{\Phi}_\sigma(r, \vartheta, \phi), t)\, d\phi\,, \quad (r, \vartheta, t) \in \mathbb{R}_{>0} \times [0, \pi] \times \mathbb{R}_{\geq 0}\,,$$

$$(3.24)$$

where

$$\boldsymbol{\Phi}_\sigma(r, \vartheta, \cdot) : [0, 2\pi] \to \mathbb{R}^3 \qquad (3.25)$$

$$\phi \mapsto D_\sigma \cdot (r \sin(\vartheta) \cos(\phi), r \sin(\vartheta) \sin(\phi), r \cos(\vartheta))^T\,,$$

and where D_σ, given by equation (2.10), denotes the rotation around the $x-$axis. For convenience, we give again the definitions of the integrated initial pressure and measurement data

$$F_\sigma(r, \vartheta) := \frac{1}{2\pi} \int_0^{2\pi} f(\Phi_\sigma(r, \vartheta, \phi))d\phi \qquad (\sigma, \vartheta, t), \in S^1 \times [0, \pi] \times \mathbb{R}_{\geq 0}$$

$$(3.26)$$

$$G_\sigma(\vartheta, t) := P_\sigma(R, \vartheta, t)\,. \qquad (3.27)$$

Note that the data $G_\sigma(\vartheta, \cdot)$ are supported in a bounded interval $[0, T]$ since acoustic waves in $\mathbb{R}^3$ pass every bounded region in finite time. More precisely acoustic pressure leaves $B_R(0)$ at a time less that $T = 2R$.

Remark 3.6. The measurement data defined in (3.27) are not what is directly measured by a family of parallel circles. To appreciate this, suppose for a moment that the pressure is caused by a small sphere at the origin contained in $B_R(0)$. Then $G_\sigma(\cdot, t)$ is a constant function for a fixed time t which would mean that the measurements are independent of the circumferences of the measuring circles. However, measurement data can easily be transformed into (3.27) by weighting each circular measurement by its circumference.

The next section outlines an algorithm to recover the integrated initial data F_σ from the data $(G_\sigma)_{\sigma \in S^1}$.

3.2.1   Reconstruction Process

Recovering the initial pressure from data collected with circular integrating or line detectors is based on a reduction of equations (1.1)-(1.3) to a two dimensional wave equation which finally leads to a two-stage reconstruction procedure. The following result is the basis of the 2D reconstruction algorithm.

Proposition 3.4. *Let $f \in C_0^\infty(\Omega)$ and define P_σ and F_σ, $\sigma \in S^1$, by (3.24), (3.26). Then P_σ satisfies the wave equation*

$$\partial_t^2 P_\sigma(r, \vartheta, t) = L P_\sigma(r, \vartheta, t), \qquad (r, \vartheta, t) \in \mathbb{R}_{>0} \times [0, \pi] \times \mathbb{R}_{\geq 0}, \qquad (3.28)$$
$$P_\sigma(r, \vartheta, 0) = F_\sigma(r, \vartheta), \qquad (r, \vartheta) \in \mathbb{R}_{>0} \times [0, \pi], \qquad (3.29)$$
$$\partial_t P_\sigma(r, \vartheta, 0) = 0, \qquad (r, \vartheta) \in \mathbb{R}_{>0} \times [0, \pi]. \qquad (3.30)$$

where the operator L is defined by

$$L := r^{-2} \partial_r r^2 \partial_r + r^{-2} \sin(\vartheta)^{-1} \partial_\vartheta \sin(\vartheta) \partial_\vartheta. \qquad (3.31)$$

Proof. The proof is almost analogous to the proof of Proposition 3.1. Equation (3.28) follows here from integrating the equation $\Delta p = \partial_t^2 p$ with respect to the azimuthal angle ϕ where the Laplace operator is given in spherical coordinates as

$$\Delta = r^{-2} \partial_r r^2 \partial_r + r^{-2} \sin(\vartheta)^{-1} \partial_\vartheta \sin(\vartheta) \partial_\vartheta + r^{-2} \sin^{-2}(\vartheta) \partial_\phi^2.$$

□

Remark 3.7. Proposition 3.4 is the basis of the following two-stage procedure for the reconstruction of f in (1.1)-(1.3) from the data $(G_\sigma)_{\sigma \in S^1}$:

(i) For $\sigma \in S^1$ (fixed position of the circles of latitude on $B_R(0)$) we determine the initial pressure F_σ of (3.28)-(3.30) using the data G_σ. An exact inversion formula for F_σ in terms of the measurement data G_σ will be derived in the next section.

Repeating this procedure for every σ, we obtain a family of functions F_σ, $\sigma \in S^1$, corresponding to averages of f over circles $\Phi_\sigma(r, \vartheta, \cdot)$given by (3.25).

(ii) Next one recognizes that for fixed $r \leq R$, the function

$$(\sigma, \vartheta) \mapsto F_\sigma(r, \vartheta)$$

is the mean of $f|_{S_r}$ over circles on the sphere S_r of radius r which are centered on a great circle. In section 3.2.3 an inversion formula for the function $f|_{S_r}$ from this means is derived. Once the functions $f|_{S_r}$ are known on all spheres S_r with $r < R$ we know the function f and the reconstruction process is finished.

3.2.2   Inversion Formula for the 2D Problem

In the following we use the spherical Hankel $\mathbf{H}^l$ transform and ϕ_l denotes the $l-$th fourier coefficient of the function ϕ with respect to the $l-$th normalized Legendre polynomial $P_l(\cos(\vartheta))$. The integral transforms are explained in more detail in the appendix.

Theorem 3.3. *Let $F_\sigma(r, \vartheta)$ and $G_\sigma(r, t)$ be given by (3.3), (3.27). Then F_σ is related to the measurement data G_σ by the Formula*

$$\mathbf{H}^l_r \{F_{\sigma,l}\}(\omega) = \sqrt{\frac{2}{\pi}} \frac{\mathbf{C}_t \{G_\sigma\}_l(\omega)}{\omega^2 j_l(r_0\omega)} \tag{3.32}$$

whenever $j_l(r_0\omega) \neq 0$.

Proof. Applying the separation Ansatz $R(r)S(\vartheta)\cos(\omega t)$ to equation to (3.28) and performing some manipulations, yields the ode's

$$\cot(\vartheta)\partial_\vartheta S + \partial^2_\vartheta S + l(l+1)S = 0$$
$$\frac{r^2}{R}\left[\frac{2}{r}\partial_r R + \partial^2_r R\right] + r^2\omega^2 - l(l+1) = 0,$$

for R and S. It is well known that the first equation is solved by the Legendre polynomials $P_l(\cos(\vartheta))$ whereas the solutions of the second equation are given by the spherical Bessel functions $j_l(rw)$. Thus for all $l \in \mathbb{N}$ the function

$$(r, \vartheta, t) \mapsto \omega^2 j_l(rw)P_l(\cos(\vartheta))\cos(\omega t)$$

is a bounded solution of (3.28) and (3.30). A general solution of equations (3.28)-(3.30) can be written as superposition

$$P_\sigma(r,\vartheta,t) = \sum_{l=0}^{\infty} \int_0^\infty \bar{F}_{\sigma,l}(\omega)\,\omega^2 j_l(r\omega) P_l(\cos(\vartheta))\cos(\omega t)d\omega, \qquad (3.33)$$

where it is assumed that the Legendre Polynomials are already normalized, i.e. $\| P_l \|_2 = 1$. Evaluating this expression at $t=0$ yields

$$F_\sigma(r,\vartheta) = \sum_{l=0}^{\infty} \int_0^\infty \bar{F}_{\sigma,l}(\omega)\omega^2 j_l(r\omega) P_l(\cos(\vartheta))d\omega.$$

Therefore its scalar product with the $l-$th Legendre Polynomial is given by

$$F_{\sigma,l}(r) = \int_0^\infty \bar{F}_{\sigma,l}(\omega)\,\omega^2 j_l(r\omega)d\omega.$$

The latter equation shows that $\bar{F}_{\sigma,l}(\omega) = \mathbf{H}_r^l\{F_{\sigma,l}\}(\omega)$ where the spherical Hankel transform of order l, $\mathbf{H}^l$, can be found in the appendix. Substituting $r=R$ in (3.33) one has $P_\sigma(r_0,\vartheta,t) = G_\sigma(\vartheta,t)$ and therefore

$$\mathbf{C}_t\{G_\sigma\}(\vartheta,\omega) = \sqrt{\frac{\pi}{2}}\sum_{l=0}^{\infty}\mathbf{H}_r^l\{F_{\sigma,l}\}(\omega)\,\omega^2 j_l(r_0\omega)\,P_l(\cos(\vartheta)). \qquad (3.34)$$

Using the orthogonality relation for Legendre polynomials implies

$$\mathbf{C}_t\{G_\sigma\}_l(\omega) = (\pi/2)^{1/2}\,\mathbf{H}_r^l\{F_{\sigma,l}\}(\omega)\,\omega^2 j_l(r_0\omega), \qquad (3.35)$$

and thus (3.32) follows. ☐

   It is interesting to note that this formula has got the same structure as Norton's famous inversion formula [43] which has been applied to photoacoustic tomography, e.g., in [5, 18].

3.2.3   Solving the 2nd Problem: Factorization Method

Once the inverse problem for the 2D problem (3.28)-(3.30) is solved for each σ, the second reconstruction step in the algorithm, described in remark 3.7, is concerned with the determination of f from its integrals over the family

of circles $c_{r\vartheta\sigma} := \Phi_\sigma(r,\vartheta,\cdot)$, where $(r,\vartheta,\sigma) \in [0,R] \times [0,\pi]^2$. For a *fixed* radius $r \leq R$ the circular means of $f|_{S_r}$ over the circles $c_{r\vartheta\sigma}$ are then given by $F_\sigma(r,\vartheta)$. Further, note that this family of circles is arranged along a great circle on S_r so that their *spherical midpoints* lie on it. Then this family of circles can be related to the average of a function over circles centered on a line via stereographic projection like shown in figure 3.4.

To state the results some notation is introduced:

- Let C_r denote the great circle on S_r that is parameterized by $\varphi_r(\sigma) = (0, r\cos(\sigma), r\sin(\sigma))$ which means that it is contained in the $yz-$plane.

- Let $\mathbf{p} = (0,0,r) \in C_r$ and $z^\perp$ be the $xy-$plane and denote by

$$\pi_r : S_r \setminus \{\mathbf{p}\} \to z^\perp, \ \mathbf{x} \mapsto \left(\frac{x}{r-z}, \frac{y}{r-z}\right) \tag{3.36}$$

  the stereographic projection from S_r onto $z^\perp$.

- Let $\mathcal{C}_0^\infty(S_r)$ be the space of infinitely differentiable functions with all derivatives vanishing at the north pole $\mathbf{p}$ and define the circular mean transform on S_r

$$(R_r h)(\vartheta, \sigma) := \int_0^{2\pi} h(\Phi_\sigma(r,\vartheta,\phi))d\phi \tag{3.37}$$

  over the circle $c_{r\vartheta\sigma}$ for every $h \in \mathcal{C}_0^\infty(S_r)$.

- Moreover for $g \in L^2(\mathbb{R}^2)$ let the integral

$$\mathbf{F}_{xy}\{g\}(\xi_1,\xi_2) := \int_{\mathbb{R}^2} g(x,y)e^{-i(x\xi_1+y\xi_2)}dxdy,$$

  denote its 2D Fourier transform.

- Finally let for an absolutely integrable function g

$$(\mathbf{R}_r g)(y,t) = \int_{C_{yt}} g(x,y)dC_{yt} \tag{3.38}$$

  denote the circular mean of g over a circle C_{yt} centered at $(0,y)$ and radius t.
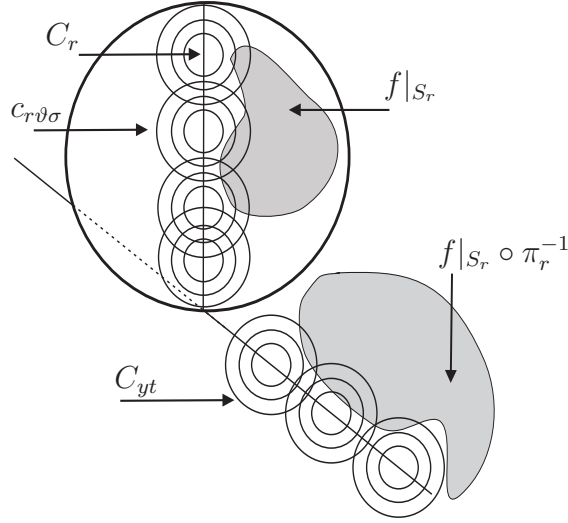
Figure 3.4: The circles $c_{r\vartheta\sigma}$ on S_r. After Stereographic projection one obtains the means over circles centered on a line of the function $f|_{S_r} \circ \pi_r^{-1}$.

Remark 3.8. Since the stereographic projection π_r is a conformal map the image $\pi_r(c_{r\vartheta\sigma}) := C_{yt}$ of every circle is a circle again. Further, with (3.37) and (3.38) the relation

$$(R_r f|_{S_r})(\vartheta, \sigma) = \int_{c_{r\vartheta\sigma}} f(\mathbf{x}) dc_{r\vartheta\sigma}(\mathbf{x})$$

$$= \int_{C_{yt}} (f|_{S_r} \circ \pi_r^{-1})(x, y) \frac{2 dC_{yt}}{r^2 + x^2 + y^2} = \mathbf{R}_r(g)(y, t), \quad (3.39)$$

where g is the is defined by

$$g(x, y) := \frac{2}{r^2 + x^2 + y^2} \left(f|_{S_r} \circ \pi_r^{-1} \right)(x, y), \qquad (3.40)$$

betwenn the circular means on the sphere and on the plane holds. The relation between R_r and $\mathbf{R}_r$ given by equation (3.39) can be interpreted as follows: If there is an inversion formula for the circular means over the family of circles $\pi_r(c_{r\vartheta\sigma})$ in the plane one is also able to reconstruct the desired function $f|_{S_r}(\pi_r^{-1}(x, y))$.

The next lemma tells us how the circles $c_{r\vartheta\sigma}$ are mapped onto the circles C_{yt} in the $xy-$plane.

Lemma 1. *Consider a circle C_{yt} in the xy plane with midpoint $(0, y)$ on the $y-$axis and radius t. Then $\pi_r^{-1}(C_{yt}) = c_{r\vartheta\sigma}$ is the circle with*

$$\sigma(y, t) = \frac{1}{2} \arctan\left(\frac{2yr}{y^2 - t^2 - r^2}\right),$$

$$\vartheta(y, t) = \frac{1}{2} \arctan\left(\frac{2tr}{y^2 - t^2 + r^2}\right).$$

Proof. The antipodal points $(y \pm t, 0)$ of a circle C_{yt} are mapped onto those points on S_r by π_r^{-1} which have the spherical coordinates $(r, \sigma^{\pm}, 0) = (r, 2 \arctan(r/(y \pm t)), 0)$. The spherical midpoint of $c_{r\vartheta\sigma}$ has got the coordinates $(r, \sigma(y, t), 0)$ with $\sigma(y, t) = (\sigma^+ + \sigma^-)/2$. Further its radius, the arclength on S_r from its midpoint to its boundary, is given as $\vartheta(y, t) = (\sigma^- - \sigma^+)/2$. The circle on S_r with this midpoint and radius is just given by $\Phi_\sigma(r, \vartheta, \cdot) = c_{r\vartheta\sigma}$. The simplified expressions for $\vartheta(y, t)$ and $\sigma(y, t)$ are given in lemma 1. $\square$

Theorem 3.4 (Factorization method). *Let $r > 0$, $f|_{S_r} \in \mathcal{C}_0^\infty(S_r)$ be symmetric with respect to the $yz-$plane and let g be as in (3.40). Then g can be reconstructed from the formula*

$$\mathbf{F}_{xy}\{g\}(\xi_1, \xi_2) = \pi |\xi_2| \, \mathbf{F}_{yt}\{\mathbf{R}_r g\}\left(\sqrt{\xi_1^2 + \xi_2^2}, \xi_2\right), \tag{3.41}$$

where

$$(\mathbf{R}_r g)(y, t) := (R_r f|_{S_r})(\vartheta(y, t), \sigma(y, t)).$$

Proof. Let C_{yt} be any circle in $z^\perp$ like in the previous lemma and g be the function (3.40). Then with lemma 1 its circular mean over C_{yt} is given by

$$(R_r f|_{S_r})(\vartheta(y, t), \sigma(y, t)) = (\mathbf{R}_r g)(y, t)$$

$$= \int_{C_{yt}} g(t \cos(\alpha), y + t \sin(\alpha)) d\alpha \tag{3.42}$$

Further note that the function g is symmetric with respect to the $y-$axis since f was symmetric with respect to the $yz-$plane and due to [24] from $f \in \mathcal{C}_0^\infty(S_r)$ it follows that g is a rapidly decreasing function on $\mathbb{R}^2$. The reconstruction of such functions from their means over circles with midpoints on a line is well treated for instance in [6]. The fourier inversion formula which is stated in the theorem is derived in there. $\square$

Remark 3.9. Although the reconstruction method above requires that $f|_{S_r}$ is symmetric with respect to the $yz-$plane in practice it is sufficient if it is supported in only one of the half spheres separated by the $yz-$plane. Then one can always interpret the values of the integrals $F_\sigma(r, \vartheta)$ as integrals over a symmetric object.

3.2.4   Stable Formulas for Wave Inversion

A direct implementation of formula (3.32) will cause serious numerical problems since the denominator becomes zero for certain values of ω. Similar to the cylindrical case [18, 64] this problem will be circumvented by expanding F_σ into a spherical Bessel series and employing reconstruction formula (3.32).

In the following let (ω_{nl}) for $l \in \mathbb{N}$ denote the zeros of the function $\omega \mapsto j_l(R\omega)$.

Theorem 3.5. *The function F_σ from (3.6) is reconstructed from the measurement data (3.27) by the formula*

$$F_\sigma(r, \vartheta) = \sqrt{\frac{2}{\pi}} \sum_{l \in \mathbb{N}} \sum_{n \in \mathbb{N}} \frac{\mathbf{S}_t \{tG_\sigma\}_l (\omega_{nl}) j_l(r\omega_{nl})}{\omega_{nl}^2 j_{l+1}(R\omega_{nl})^3} P_l(\cos(\vartheta)). \qquad (3.43)$$

Proof. Since $f \in \mathcal{C}_0^\infty(\Omega)$ the functions $F_{\sigma,l}(\cdot)$ are supported in $[0, R]$ and thus can be expanded into a series of spherical Bessel functions

$$F_{\sigma,l}(r) = \sum_{n \in \mathbb{N}} \mathbf{H}_r^l \{F_{\sigma,l}\} (\omega_{nl}) \frac{j_l(r\omega_{nl})}{j_{l+1}(R\omega_{nl})^2}. \qquad (3.44)$$

For exact measurement data the enumerator in (3.32) has to be zero whenever the denominator is zero. Thus one can use the rule of D'Hospital to evaluate $\mathbf{H}_r^l \{F_{\sigma,l}\}$ at ω_{nl}:

$$(\pi/2)^{1/2} \mathbf{H}_r^l \{F_{\sigma,l}\} (\omega_n) = \lim_{\omega \to \omega_{nl}} \frac{\partial_\omega \mathbf{C}_t \{G_\sigma\}_l (\omega)}{\partial_\omega \omega^2 j_l(R\omega)}$$

$$= \lim_{\omega \to \omega_{nl}} \frac{-\mathbf{S}_t \{tG_\sigma\}_l (\omega)}{2\omega j_l(R\omega) + \omega^2 \partial_\omega j_l(R\omega)} = \frac{\mathbf{S}_t \{tG_\sigma\}_l (\omega_{nl})}{\omega_{nl}^2 j_{l+1}(R\omega_{nl})},$$

where the last expressions follow from the identities $\partial_\omega j_l(\omega) = \frac{l}{\omega} j_l(\omega) - j_{l+1}(\omega)$ and $\partial_\omega \mathbf{C}_t \{tG_\sigma\} = -\mathbf{S}_t \{tG_\sigma\}$. $\qquad \square$

The expansion into a series of spherical Bessel functions in formula (3.43) can be implemented stable and can also be used to derive a second inversion formula. The following result can easily be obtained from the expansion formulas in derived in [59].

Proposition 3.5. *Let f_σ^m and g_σ^m denote the Fourier coefficients of the functions $f(\mathbf{\Phi}_\sigma(z, r, \phi))$ and $g_\sigma(\vartheta, \phi, t) := p(\mathbf{\Phi}_\sigma(r_0, \vartheta, \phi), t)$, where f and p are the unique solution of (1.1)-(1.3), with respect to ϕ. Then*

$$\mathbf{H}_r^l\{f_{\sigma,l}^m\}(\omega) = \frac{2}{\pi} \frac{\mathbf{F}_t\{g_{\sigma,l}^m\}(\omega)}{\omega^2\, h_l^{(1)}(R\omega)}, \qquad \omega \in \mathbb{R},\ l \in \mathbb{N}, \tag{3.45}$$

with $h_l^{(1)}$ denoting the l-th order Hankel function of the first kind.

Due to $F_{\sigma,l} = f_{\sigma,l}^0$ and $G_{\sigma,l} = g_{\sigma,l}^0$ and the fact that in the denominator of (3.45) this proposition leads immediately to a second inversion formula, given in the following

Theorem 3.6. *With the same assumptions as in Theorem 3.5*

$$F_\sigma(r, \vartheta) = \frac{2}{\pi} \sum_{l \in N} \sum_{n \in \mathbb{N}} \frac{\mathbf{F}_t\{G_{\sigma,l}\}(\omega_{nl})}{\omega_{nl}^2\, h_l^{(1)}(r_0\omega_{nl})} \frac{j_l(rv_n)P_l(\cos(\vartheta))}{j_{l+1}(R\omega_{nl})^2}. \tag{3.46}$$

Proof.   □

Remark 3.10. In Xu and Wang [59] they use the source term formulation

$$\begin{aligned} \Delta p(\mathbf{x}, t) - \partial_t^2 p(\mathbf{x}, t) &= f(\mathbf{x})\frac{d\delta(t)}{dt} \\ p(\mathbf{x}, t) = \partial_t p(\mathbf{x}, t) &= 0,\ t < 0 \end{aligned}$$

of the wave equation which for is equivalent to the initial value problem (1.1)-(1.3) for $t > 0$. Then their derivation of (3.45) is based on a series expansion of a Green function, which arises in an integral representation for the temporal Fourier transform of p [39]:

$$\frac{e^{i\omega(|\Phi_\sigma(R,\vartheta,\phi) - \Phi_\sigma(r,\vartheta,\phi)|)}}{|\Phi_\sigma(R, \vartheta, \phi) - \Phi_\sigma(r, \vartheta, \phi)|} = \sum_{l=0}^{\infty} j_l(\omega r) h_l^{(1)}(\omega R) P_l(\cos(\vartheta)). \tag{3.47}$$

Then (3.45) is derived straight forward using orthogonality relations for the Legendre polynomials and Bessel functions.

3.2.5   Noisy Data

In practise only noisy measurement data, write $G^\delta := G^\delta_\sigma$, are available and generically there is no solution of system (3.28)-(3.30) such that $P(r_0, \vartheta, t) = G^\delta(\vartheta, t)$. However, we can show that inversion formulas (3.43) and (3.46) still make sense in the case of noisy data G^δ.

Theorem 3.7. *Formulas (3.43) and (3.46) define continuous operators*

$$F : L^2([0, \pi] \times [0, T], \sin(\vartheta)d\vartheta dt) \to L^2([0, \pi] \times \mathbb{R}_{>0}, \sin(\vartheta)d\vartheta r^2 dr)$$

where $F(G^\delta)$ is either defined by formula (3.43) or (3.17).

Proof. The assertion in the theorem 3.7 is proven here for formula (3.43) only since the proof for (3.46) is almost analogous. Note that for any $G^\delta \in L^2([0, \pi] \times [0, T], \sin(\vartheta)d\vartheta dt)$ the function $\omega \mapsto \mathbf{S}_t \left\{ tG^\delta \right\}(\omega)$ is continuous and thus it makes sense to evaluate it at the discrete points ω_{nl}. Since the Legendre polynomials P_l form an orthonormal basis in $L^2([0, \pi], \sin(\vartheta)d\vartheta)$ the coefficients G^δ_l defined by (7.1) are in $\ell^2(\mathbb{N})$. Moreover for each $l \in \mathbb{N}$ the sequence $\left(\mathbf{S}_t \left\{ tG^\delta \right\}(\omega_{nl}) \right)_n$ also belongs to $\ell^2(\mathbb{N})$: To see this note that the roots ω_{nl}, for each l, increase in such a way that there is a $c > 0$ such that $\omega_{nl} > l + cn$. Moreover for each ω_{nl} we can choose a $k \in \mathbb{N}$ such that $2k\pi/T$ is as close to ω_{nl} as possible from below and write $2k\pi/T + \epsilon = \omega_{nl}$. Then for each $l \in \mathbb{N}$ it follows that the k are unbounded since the ω_{nl} are unbounded and the estimate

$$\left| \mathbf{S}_t \left\{ tG^\delta \right\}(\omega_{nl}) \right| = \left| \int_0^T tG^\delta(t) \sin((2k\pi/T + \epsilon)t)dt \right| \leq$$

$$\left| \int_0^T tG^\delta(t) \sin(2kt\pi/T)dt \right| + \left| \int_0^T tG^\delta(t) \cos(2kt\pi/T)dt \right|$$

holds.   Therefore $\left| \mathbf{S}_t \left\{ tG^\delta \right\}(\omega_{nl}) \right|$ is bounded by the sum of the absolute values of the k'th Fourier coefficients of $tG(\vartheta, t)$ with respect to the basis $\{\sin(2k\pi/T), \cos(2k\pi/T)\}$ and so the sequence $\left(\mathbf{S}_t \left\{ tG^\delta \right\}(\omega_{nl}) \right)_n$ belongs to $\ell^2(\mathbb{N})$. Putting all together we see that also the sequence $\left(\mathbf{S}_t \left\{ tG^\delta \right\}_l(\omega_{nl}) \right)_{nl}$ lies in $\ell^2(\mathbb{N} \times \mathbb{N})$. The remaining term in the series expansion (3.43) with respect to the basis functions $P_l(\cos(\vartheta))$ and $j_l(r\omega_{nl})/j_{l+1}(R\omega_{nl})$ is $1/(\omega^2_{nl} j^2_{l+1}(R\omega_{nl}))$. From the asymptotic formula for the Bessel function

$$j_{l+1}(R\omega_{nl}) \approx \cos\left(R\omega_{nl} - \frac{(l+2)\pi}{2} - \frac{\pi}{4} \right) \frac{1}{R\omega_{nl}}$$

and the fact that the ω_{nl} are the roots of j_l it follows that the sequence $\left(1/(\omega_{nl}^2\, j_{l+1}^2(R\omega_{nl}))\right)_{nl}$ is bounded and thus $\left(1/(\omega_{nl}^2\, j_{l+1}^2(R\omega_{nl})\, \mathbf{S}_t \left\{tG^\delta\right\}_l (\omega_{nl})\right)_{nl}$ also lies in $\ell^2(\mathbb{N} \times \mathbb{N})$ and so the series in (3.43) converges for any $G^\delta \in L^2([0,\pi] \times [0,T], \sin(\vartheta)d\vartheta dt)$. Since we know that formula (3.43) converges it can easily be checked that F is continues at 0 and since F is a linear operator the continuity of F follows. $\qquad\square$

The result above guarantees that for each of the formulas above there is a constant M such that

$$\| F - F^\delta \| \le M \| G - G^\delta \| < M\delta,$$

which means that the reconstruction error becomes small if the measurements are accurate enough.

The last theorem guarantees the convergence reconstruction formulas (3.43) and (3.46) for data in space $L^2([0,\pi] \times [0,T], \sin(\vartheta)d\vartheta dt)$. As an application of this result we derive a series expansion identity for characteristic function in the appendix. Moreover, this identity leads to a new series expansion for the dirac distribution.

Chapter 4

Conversion of Measurement Data

In this part of the thesis we suppose that initial pressure f is supported in the half space $H = \{\mathbf{x} \in \mathbb{R}^3 : x \geq 0\}$. Further we assume that we know the circular means, of the acoustic pressure p over two particular families of circles in $E = \partial H$. Our aim is, to determine the pressure p pointwise from this circular means, so that we can apply reconstructions formulas that require pointwise data on E, [54, 57, 58].

The first family of circles consists of the circles which have (fixed) radius r_{d} and are centered at $\mathbf{x} \in \mathbb{R}^2$. Pointwise inversion formulas for this family are of particular interest since these circular integrals are relatively easy to measure in applications. Secondly, we consider the family of circles which are tangential to another circle of fixed radius. Both families are depicted in the figure 2.5.

We define the operator

$$G : \mathcal{C}_0^\infty(\mathbb{R}^2 \times \mathbb{R}_{\geq 0}) \to \operatorname{ran}\,(G) \subset \mathcal{C}_0^\infty(\mathbb{R}^2 \times \mathbb{R}_{\geq 0} \times \mathbb{R}_{\geq 0}) \qquad (4.1)$$

$$G(p)(\mathbf{x}, r, t) = \frac{1}{2\pi} \int_0^{2\pi} p(\mathbf{x} + (r\cos(\alpha), r\sin(\alpha)), t)d\alpha,$$

where $G(p)(\mathbf{x}, r, t)$ is the circular mean over the circle with center $\mathbf{x}$ and radius r like depicted in figure 4.1.

Moreover we define the operator

$$G^a : \mathcal{C}_0^\infty(\mathbb{R}^2 \times \mathbb{R}_{\geq 0}) \to \operatorname{ran}(G^a) \subset \mathcal{C}_0^\infty(\mathbb{R}^2 \times \mathbb{R}_{\geq 0}) \tag{4.2}$$

by $G^a(p)(\mathbf{x}, t) := G(\mathbf{x}, r_{\mathrm{d}})$, which maps the function p onto the circular mean over the circle with center $\mathbf{x}$ and radius r_{d}. Circular means, over the second family of circles, are described by the operator

$$G^b : \mathcal{C}_0^\infty(\mathbb{R}^2 \times \mathbb{R}_{\geq 0}) \to \operatorname{ran}(G^b) \subset \mathcal{C}_0^\infty(\mathbb{R}^2 \times \mathbb{R}_{\geq 0}) \tag{4.3}$$

where $G^b(p)(\mathbf{x}, t) := G(\mathbf{x}, r)$ is the circular mean over the circle centered at $\mathbf{x}$ and radius $r = |\mathbf{x}| - \rho > 0$. Such a circle is tangential to the circle of radius ρ, which is centered at the origin.

In the following we will use the abbreviations

$$G^a(\mathbf{x}) := G^a(p)(\mathbf{x}, t), \quad G^b(\mathbf{x}) := G^b(p)(\mathbf{x}, t) \tag{4.4}$$
$$G(\mathbf{x}, r) := G(p)(\mathbf{x}, r, t),$$

were we also omit the time parameter since it is only a dummy variable in following computations.

4.1 Pointwise reconstruction for circles with fixed radius

Firstly, we are concerned with the inversion of the operator (4.2). The injectivity of this operator has been investigated in [53]. From the results therein we know that the operator G^a is injective for functions p in $L^p(\mathbb{R}^n)$ for $p < 2n/(n-1)$. Since p is compactly supported in the present case we know that its reconstruction from its circular has a unique solution. The first reconstruction method, which we present, is based on the simple observation that the integral over a circle, of fixed radius r_{d} and center $\mathbf{x}$, can be written as a convolution with a delta distribution. Although this method has already been investigated in [4] we present it here since it was found independently by the author.

In the following the abbreviations (4.4) are used and $\mathbf{F}$ denotes the Fourier transform which is defined in the appendix.

Theorem 4.1. *Let $G^a(\mathbf{x})$ denote the circular means, over circles of radius r_{d} and center $\mathbf{x}$. Then the pressure p is reconstructed point wise by*

$$\mathbf{F}\{p\}(\xi) = \frac{\mathbf{F}\{G^a\}(\xi)}{r_{\mathrm{d}} J_0(r_{\mathrm{d}}|\xi|)}, \tag{4.5}$$

whenever $J_0(r_{\mathrm{d}}|\xi|) \neq 0$.

Proof. It is not hard to see that $G^a(\mathbf{x})$ can be rewritten as

$$G^a(\mathbf{x}) = \frac{1}{2\pi} \int_0^{2\pi} p(\mathbf{x} + r_{\mathrm{d}}(\cos(\alpha), \sin(\alpha)))\, d\alpha$$

$$= \frac{1}{2\pi} \int_{\mathbb{R}^2} p(\mathbf{x})\delta(|\mathbf{x} - \mathbf{y}| - r_{\mathrm{d}})d\mathbf{y} = p(\mathbf{x}) * \delta(|\mathbf{x}| - r_{\mathrm{d}}). \tag{4.6}$$

The Fourier transform of the convolution product is equal to the product of the Fourier transforms of each of the factors. We compute the fourier transform of the distribution, which is given by

$$\mathbf{F}\{\delta(|\mathbf{x}| - r_{\mathrm{d}})\}(\xi) = \int_{\mathbb{R}^2} \delta(|\mathbf{x}| - r_{\mathrm{d}})e^{-i\mathbf{x}\xi}d\mathbf{x} = \int_{|\mathbf{x}|=r_{\mathrm{d}}} e^{-i\mathbf{x}\xi}d\mathbf{x}.$$

The latter integral is invariant under rotation since for any $A \in SO(2)$ the equation

$$\mathbf{F}\{\delta(|\mathbf{x}| - r_{\mathrm{d}})\}(\xi) = \int_{|\mathbf{x}|=r_{\mathrm{d}}} e^{-i\mathbf{x}\xi}d\mathbf{x} = \int_{|\mathbf{y}|=r_{\mathrm{d}}} e^{-iA^{-1}\mathbf{y}\xi}d\mathbf{y}$$

$$= \int_{|\mathbf{y}|=r_{\mathrm{d}}} e^{-\mathbf{y}A\xi}d\mathbf{y} = \mathbf{F}\{\delta(|\mathbf{x}| - r_{\mathrm{d}})\}(A\xi)$$

holds. Introduce $\tilde{\xi} = |\xi|(1,0)$, then, because of rotation invariance, we have

$$\mathbf{F}\{\delta(|\mathbf{x}| - r_{\mathrm{d}})\}(\xi) = \mathbf{F}\{\delta(|\mathbf{x}| - r_{\mathrm{d}})\}(\tilde{\xi}) = \tag{4.7}$$

$$\int_{|\mathbf{x}|=r_{\mathrm{d}}} e^{-i\mathbf{x}\tilde{\xi}}\,d\mathbf{x} = r_{\mathrm{d}} \int_0^\pi \cos(r_{\mathrm{d}}|\xi|\sin(t))\,dt - ir_{\mathrm{d}} \int_0^\pi \sin(r_{\mathrm{d}}|\xi|\sin(t))\,dt.$$

On the other hand we conclude, again by rotation invariance, that

$$\mathbf{F}\{\delta(|\mathbf{x}| - r_{\mathrm{d}})\}(\xi) = \mathbf{F}\{\delta(|\mathbf{x}| - r_{\mathrm{d}})\}(-\tilde{\xi}) = \tag{4.8}$$

$$= r_{\mathrm{d}} \int_0^\pi \cos(r_{\mathrm{d}}|\xi|\sin(t))\,dt + ir_{\mathrm{d}} \int_0^\pi \sin(r_{\mathrm{d}}|\xi|\sin(t))\,dt.$$

Finally, after adding equations (4.7) and (4.8) we arrive at

$$\int_{|\mathbf{x}|=r_\mathrm{d}} e^{-i\mathbf{x}\xi} = r_\mathrm{d} \int_0^\pi \cos(r_\mathrm{d}|\xi|\sin(t))\,dt = r_\mathrm{d} J_0(r_\mathrm{d}|\xi|).$$

The last equality is an integral representation for the Bessel function J_0 which for instance can be found in [48]. $\qquad\square$

The fraction in equation (4.5) causes problems at the roots of the denominator $J_0(r_\mathrm{d}|\xi|)$ which makes the reconstruction sensitive to noise. A possibility to evaluate the fraction, near a root of if its denominator, is to apply the rule of D'Hospital. However, numerical experiments indicate that this does not significantly improve the quality of reconstructions which motivates to search for a new formula.

In the following we parameterize $\mathbb{R}^2$ in polar coordinates. Further we employ the Fourier series expansion of a compactly supported function with respect to its angular variable like explained in the appendix. In polar coordinates the operator 4.1 has the form

$$G(R,\phi,r) = \frac{1}{2\pi} \int_0^{2\pi} p(\mathbf{x} + r(\cos(\alpha),\sin(\alpha)))d\alpha, \qquad (4.9)$$

where $\mathbf{x} = R(\cos(\phi),\sin(\phi))$.

The next theorem establishes a relationship between the Fourier coefficients of the function G and the pressure p.

Theorem 4.2. *Let G and p be expanded as Fourier series with respect to their angular variable. Then the Fourier coefficients satisfy the relation*

$$G_\lambda(R,r) = \int_{-1}^1 p_\lambda\left(\sqrt{R^2 + r^2 + 2rRt}\right) \frac{T_{|\lambda|}(t)}{\sqrt{1-t^2}}dt\,. \qquad (4.10)$$

Proof. Expanding p into a Fourier series

$$p(\mathbf{x} + r(\cos(\alpha),\sin(\alpha))) = \sum_{\lambda\in\mathbb{Z}} p_\lambda(|\mathbf{x} + r(\cos(\alpha),\sin(\alpha))|)e^{i\lambda\alpha}$$

together with equation (4.9), it follows that

$$G(R,\phi) = \int_0^{2\pi} \sum_{\lambda\in\mathbb{Z}} p_\lambda\left(\sqrt{R^2 + r^2 + 2rR\cos(\alpha-\phi)}\right)e^{i\lambda\alpha}d\alpha$$
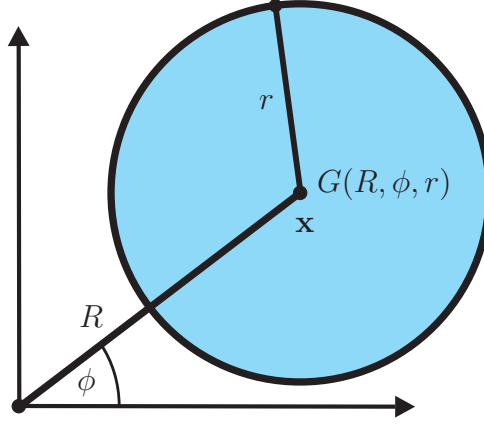
Figure 4.1: Circular mean over the circle centered at $R(\cos(\phi), \sin(\phi))$ with radius r.

With the Funk–Hecke theorem we have

$$G(R, \phi) = \sum_{\lambda \in \mathbb{Z}} \left(\int_{-1}^{1} p_\lambda \left(\sqrt{R^2 + r^2 + 2rRt} \right) \frac{T_{|\lambda|}(t)dt}{\sqrt{1-t^2}} \right) e^{i\lambda\phi}$$

and the result follows after expanding G into a Fourier series. $\qquad\square$

In the case when the detector radius is fixed we have that $G^a(R, \phi) = G(R, \phi, r_{\mathrm{d}})$. In order to reconstruct acoustic pressure p from measurement data G^a, we have to solve the integral equation

$$G^a_\lambda(R) = \frac{1}{2\pi} \int_{-1}^{1} p_\lambda \left(\sqrt{R^2 + r_{\mathrm{d}}^2 + 2r_{\mathrm{d}}Rt} \right) \frac{T_{|\lambda|}(t)}{\sqrt{1-t^2}} dt \qquad (4.11)$$

for each λ. Solving a sequence of one dimensional problems is a simplification of the original problem, where one would have to solve the two dimensional equation $G^a(\mathbf{x}) = \frac{1}{2\pi} \int_0^{2\pi} p(\mathbf{x} + r_{\mathrm{d}}(\cos(\alpha), \sin(\alpha)))d\alpha$ directly. Unfortunately, for each λ, the one dimensional problems have to be solved numerically, since we were not able to derive an exact solution of equation (4.11).

4.2 Reconstruction over circles tangential to another circle

Secondly, we consider the circular means over the family of circles that are tangential to a circle of fixed radius ρ. Note that for $r = |\mathbf{x}| - \rho$ we have that $G(\mathbf{x}, |\mathbf{x}| - \rho) = G^b(\mathbf{x})$. According to Theorem (4.2) the Fourier coefficients of G^b satisfy the relation

$$G_\lambda^b(R, r) = \int_{-1}^{1} p_\lambda \left(\sqrt{R^2 + r^2 + 2Rrt} \right) \frac{T_{|\lambda|}(t)}{\sqrt{1 - t^2}} dt, \qquad (4.12)$$

with $r = R - \rho$. The next result establishes a relationship, between the coefficients G_λ^b and the pressure p_λ, outside the circle of radius ρ, in terms of the Mellin transform. The Mellin transform $\mathbf{M}$, which is a very useful tool in the field of integral equations, is introduced in the appendix of this thesis.

In order to state our result in a compact form we use the following abbreviations

$$g_\lambda(k) := G_\lambda \left(\frac{\rho + \sqrt{k^2 + \rho^2}}{2}, \frac{\sqrt{k^2 + \rho^2} - \rho}{2} \right) \qquad (4.13)$$

$$u_\lambda(k) := p_\lambda \left(\sqrt{k^2 + \rho^2} \right), \qquad (4.14)$$

$$h_\lambda(k) := \begin{cases} T_{|\lambda|} \left(\sqrt{k^2 - 1} \right) / \sqrt{k^2 - 1} & \text{if } |k| > 1 \\ 0 & \text{else.} \end{cases} \qquad (4.15)$$

Theorem 4.3. *Let the Fourier coefficients of G and p satisfy the integral equation (4.10). This integral equation can be written as Mellin convolution product when it is assumed that $\rho = R - r$ is constant. In this case the following relation*

$$\mathbf{M}\{u_\lambda\}(s)\ \mathbf{M}\{h_\lambda\}(s) = \mathbf{M}\{g_\lambda\}(s) \qquad (4.16)$$

holds, where the functions g_λ, u_λ and h_λ ere defined by equations (4.13), (4.14) and (4.15) respectively.

Proof. We introduce the new integration variable $s^2 = R^2 + r^2 + 2rRt$. Then

the right side of equation (4.12) transforms into

$$\int_{R-r}^{R+r} \frac{p_\lambda(s)\, T_{|\lambda|}\left(\frac{s^2-R^2-r^2}{2rR}\right) s\, ds}{\sqrt{\left((r+R)^2-s^2\right)\left(s^2-(R-r)^2\right)}}.$$

To proceed note that for $-1 \le x \le 1$ the identities

$$T_{|\lambda|}(x) = \cos(\lambda \arccos(x)), \quad \arccos(x) = 2\arctan\left(\frac{\sqrt{1-x^2}}{1+x}\right)$$

hold and since $-1 \le \frac{s^2-R^2-r^2}{2rR} \le 1$ for $R-r \le s \le R+r$ the latter integral becomes

$$\int_{R-r}^{R+r} \frac{p_\lambda(s)\, s\, ds}{\sqrt{\left((r+R)^2-s^2\right)\left(s^2-(R-r)^2\right)}}\, T_{|\lambda|}\left(\sqrt{\frac{(R+r)^2-s^2}{s^2-(R-r)^2}}\right).$$

Now set $\rho = R-r$ and $\widetilde{\rho} = R+r$ and introduce the relations

$$\widetilde{\rho}^2 - \rho^2 = k^2, \quad s^2 - \rho^2 = p^2. \tag{4.17}$$

by our assumption the variable ρ is fixed which implies that equations (4.13) and (4.14) are functions of k only. Moreover using the relation (4.17), with abbreviations (4.13) and (4.14), we can be rewrite (4.12) as

$$g_\lambda(k) = \int_0^k \frac{u_\lambda(p)}{\sqrt{k^2-p^2}}\, T_{|\lambda|}\left(\frac{\sqrt{k^2-p^2}}{p}\right) dp. \tag{4.18}$$

We proceed by rewriting the latter integral to

$$g_\lambda(k) = \int_0^k \frac{u_\lambda(p)\, dp}{p}\, T_{|\lambda|}\left(\sqrt{(k/p)^2-1}\right) \frac{dp}{\sqrt{(k/p)^2-1}}.$$

Introduce the a new integration variable σ, by the relation $\sigma p = k$, the latter expression becomes

$$g_\lambda(k) = \int_1^\infty \frac{u_\lambda(k/\sigma)\, dp}{\sqrt{\sigma^2-1}}\, T_{|\lambda|}\left(\sqrt{\sigma^2-1}\right) \frac{1}{\sigma}\, d\sigma. \tag{4.19}$$

This, is the Mellin convolution of the functions u_λ and h_λ. Thus applying the mellin transform to equation gives the desired result. $\square$

Rearranging formula (4.16) as

$$\mathbf{M}\left\{u_\lambda\right\}(s) \; = \; \frac{\mathbf{M}\left\{g_\lambda\right\}(s)}{\mathbf{M}\left\{h_\lambda\right\}(s)}, \tag{4.20}$$

whenever $\mathbf{M}\left\{h_\lambda\right\}(s) \neq 0$, and applying the inverse Mellin transform yields u_λ. Unfortunately, we could not derive an analytic expression for $\mathbf{M}\left\{u_\lambda\right\}$. However, this is not a problem since its Mellin transform can be computed numerically and stored in a lookuptable for implementation issues. Once u_λ is determined, according to (4.13) p_λ is given and thus p can be computed from its Fourier series outside the circle with radius ρ.

Chapter 5

Resolution of Circular Integrating Detectors

In applications circular integrating detectors are approximated by toroidal shaped optical fibers with a certain thickness. As a result, pressure integrals, which are measured with approximate circular (toroidal) detectors, are only approximations to a circular integral. Moreover, the integral, measured by a toroidal detector, is recorded in an ultrasound detection system. This system does not immediately respond, when acoustic pressure is collected by a toroidal detector, which causes inaccurate temporal measurements. Both factors, the thickness of a toroidal detector and the inexactness of the ultrasound detection system, cause errors in the measurement data. Thus, a reconstruction algorithm, that uses this erroneous data yields a blurred version of the initial data f. In the following we present a model, that investigates the thickness of a toroidal detector and the time inaccuracy of the detection system, which can be used to describe the blurring of initial data explicitly.

In this section $\mathcal{W}^{3D}(f)(\mathbf{x}, t)$ will denote the solution of the problem (1.1)-(1.3) and Σ denotes the set of all two dimensional families of circles in $\mathbb{R}^3$. Further, we assume that a particular family $\Sigma_0 \subset \Sigma$ is parameterized by a map $Q \to \Sigma_0$, $\mathbf{q} \mapsto c_{\mathbf{x}(\mathbf{q})}$, where $\mathbf{q} = (q_1, q_2)$ and $Q \subset \mathbb{R}^2$ is an open set of parameters. Here $c_{\mathbf{x}(\mathbf{q})}$ denotes the circle that is centered at the point $\mathbf{x}(\mathbf{q}) \in \mathbb{R}^3$ that is contained in the affine plane $\varepsilon : \mathbf{x}(\mathbf{q}) + \mathbb{R}v_1(\mathbf{x}(\mathbf{q})) + \mathbb{R}v_2(\mathbf{x}(\mathbf{q}))$ and has radius $r_{\mathbf{x}(\mathbf{q})}$, where the vectors $v_1(\mathbf{x})$ and $v_2(\mathbf{x})$ form an orthonormal basis of ε. Further, we assume that the circles Σ_0 do not intersect with a
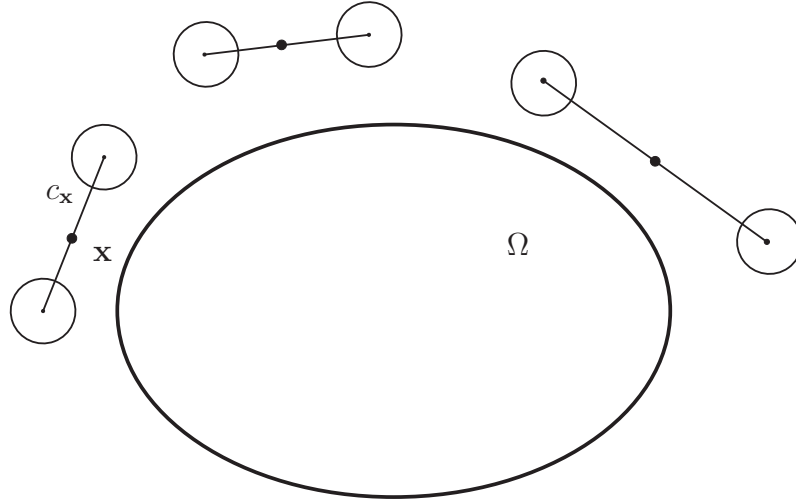
Figure 5.1: A cross section of ring shaped detectors placed around Ω.

domain Ω that contains the support of the initial pressure f as depicted in figure 5.1.

Suppose we know the circular means of acoustic pressure over a two dimensional family of circles. Then we are concerned with the inversion of the operator

$$C : \mathcal{C}_0^\infty(\Omega) \to \mathrm{ran}(C) \subset \mathcal{C}^\infty(Q \times \mathbb{R}_{\geq 0}) \tag{5.1}$$

$$C(f)(\mathbf{x}(\mathbf{q}), t) = \frac{1}{2\pi} \int_0^{2\pi} W^{3D}(f)(c_{\mathbf{x}(\mathbf{q})}(\alpha), t) d\alpha,$$

that maps the initial density f onto the circular mean of acoustic pressure $W^{3D}(f)(\mathbf{x}, t) := p(\mathbf{x}, t)$ (where p is the solution of (1.1)-(1.3)) over the circle $c_{\mathbf{x}(\mathbf{q})}$, where the circle $c_{\mathbf{x}(\mathbf{q})}$ is parameterized by the map $c_{\mathbf{x}(\mathbf{q})} : \alpha \mapsto r_{\mathbf{x}(\mathbf{q})} \cos(\alpha) v_1(\mathbf{x}(\mathbf{q})) + r_{\mathbf{x}(\mathbf{q})} \sin(\alpha) v_2(\mathbf{x}(\mathbf{q})) + \mathbf{x}(\mathbf{q})$. We assume that the operator (5.1) possesses an inverse C^{-1} for a certain family of circles Σ_0. Explicit formulas for the inverse can only be given in very special cases. For instance these families Σ_0 are given by one of the families considered in the Sections 3.1 and 3.2.

In the following calculations the variable $\mathbf{q}$ will be omitted.
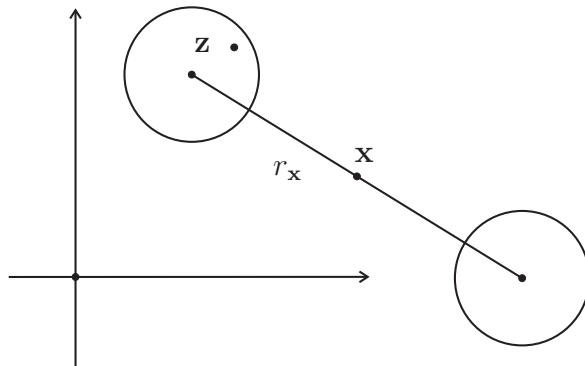
Figure 5.2: Cross section of a toroidal shaped detector. The weight ω assigned to the point $\mathbf{z}$ depends on the relative position of the point $\mathbf{z}$ to the center $\mathbf{x}$ of the toroidal detector.

The next operator models the inexactness in measurement data, which are caused by the thickness of a toroidal detector and the temporal inaccuracy of the ultrasound detection system.

$$C_{\varphi,w} : \mathcal{C}_0^\infty(\Omega) \to \operatorname{ran}(C) \subset \mathcal{C}^\infty(Q \times \mathbb{R}_{\geq 0}) \tag{5.2}$$

$$C_{\varphi,w}(f)(\mathbf{x}, t) := \varphi *_t \int_{\mathbb{R}^3} w(\mathbf{x}, \mathbf{z}) \, W^{3D}(f)(\mathbf{z}, t) \, d\mathbf{z},$$

where φ denotes the impulse response function that describes blurred time measurements and w is a weight function that describes the sensitivity of a toroidal detector as explained in figure 5.2.

The following theorems investigate influence of erroneous data, caused by the ultrasound detection system, onto the reconstruction of the initial pressure f. The first theorem establishes, that it is equivalent to either convolve the function $C(f)$ in time, with φ, or to apply the operator C to the initial data f, convolved with $-\pi\varphi(|\mathbf{x}|)/(|\mathbf{x}|)$.

Theorem 5.1. *Let $f \in \mathcal{C}_0^\infty(\Omega)$ and let $\varphi : \mathbb{R} \to \mathbb{R}$ be even, absolutely integrable, compactly supported and differentiable. Then the equality*

$$\varphi *_t C(f)(\mathbf{x}, t) = C(f * \Phi)(\mathbf{x}, t), \tag{5.3}$$

where

$$\Phi(\mathbf{x}) = -\frac{\pi}{2}\frac{\varphi'(|\mathbf{x}|)}{|\mathbf{x}|}$$

holds for all $(\mathbf{x}, t)$ *with* $\mathbf{x}$ *outside the support of* $\Phi * f$.

Proof. Let the function $\Phi(\mathbf{x}) = \widetilde{\varphi}(|\mathbf{x}|)$ be radially symmetric, absolute integrable and continues. First we will adjust Φ in such a way that the equation

$$W^{3D}(f * \Phi)(\mathbf{x}, t) = \varphi *_t W^{3D}(f)(\mathbf{x}, t)$$

holds. From the definition (5.1) it is then easy to see that the last expression implies (5.3).

We apply D'Alemberts formula for the solution of the three dimensional wave equation [26], to the function $\Phi * f$, which gives

$$W^{3D}(\Phi * f)(\mathbf{x}, t) = \frac{1}{4\pi}\partial_t t \int_{S^2} (f * \Phi)(\mathbf{x} + t\omega)dS(\omega)$$

$$= \frac{1}{4\pi}\partial_t t \int_{S^2}\left(\int_{\mathbb{R}^3} f(\mathbf{x}')\widetilde{\varphi}(|\mathbf{x} + t\omega - \mathbf{x}'|)d\mathbf{x}'\right)dS(\omega).$$

To proceed we substitute $\mathbf{x}' = \mathbf{x} + \rho\sigma$ with $\rho \in \mathbb{R}_{>0}$ and $\sigma \in S^2$, in the inner integral and apply Fubini's theorem which leads us to

$$W^{3D}(\Phi * f)(\mathbf{x}, t)$$

$$= \frac{1}{4\pi}\partial_t t \int_{S^2}\left(\int_{S^2}\int_0^\infty f(\mathbf{x} + \rho\sigma)\widetilde{\varphi}(|\rho\sigma - t\omega|)\rho^2 d\rho dS(\sigma)\right)dS(\omega)$$

$$= \partial_t t \int_0^\infty \int_{S^2} f(\mathbf{x} + \rho\sigma)\left(\frac{1}{4\pi}\int_{S^2}\widetilde{\varphi}(|\rho\sigma - t\omega|)dS(\omega)\right)\rho^2 d\rho dS(\sigma).$$

The last expression in the parenthesis

$$\frac{1}{4\pi}\int_{S^2}\widetilde{\varphi}(|\rho\sigma - t\omega|)dS(\omega)$$

is the mean value the of the function $\widetilde{\varphi}(|\mathbf{x}|)$ over a sphere with radius t centered $\rho\sigma$. Let I_Φ denote a primitive of $s \mapsto \widetilde{\varphi}(\sqrt{s})$, then the we have

$$\frac{1}{4\pi}\int_{S^2}\widetilde{\varphi}(|\rho\sigma - t\omega|)dS(\omega) = \frac{I_\Phi((\rho + t)^2) - I_\Phi((\rho - t)^2)}{4t\rho}, \qquad (5.4)$$

for $t, \rho > 0$. This identity can be found in [22] and the proof therein is presented in the appendix. Using (5.4) we have that

$$W^{3D}(\Phi * f)(\mathbf{x}, t) =$$

$$\frac{1}{4}\partial_t \int_0^\infty \left(I_\Phi((\rho + t)^2) - I_\Phi((\rho - t)^2)\right) \rho \int_{S^2} f(\mathbf{x} + \rho\sigma)dS(\sigma)d\rho. \qquad (5.5)$$

Since the time derivative of the function $t \mapsto I_\Phi((\rho + t)^2) - I_\Phi((\rho - t)^2)$ is continues we can interchange the order of differentiation and integration in equation (5.5) an we have that

$$W^{3D}(\Phi * f)(\mathbf{x}, t) = \frac{1}{2}\int_0^\infty (\rho - t)\widetilde{\varphi}(|\rho - t|)\left(\rho \int_{S^2} f(\mathbf{x} + \rho\sigma)dS(\sigma)\right)d\rho. \qquad (5.6)$$

The term $\partial_t I_\Phi((\rho + t)^2)$ vanishes since $\mathbf{x} \notin \operatorname{supp}(\Phi * f)$. On the other hand, again by D'Alemberts formula, we have

$$\varphi *_t W^{3D}(f)(\mathbf{x}, t) = \frac{1}{4\pi}\varphi * \partial_t t \int_{S^2} f(\mathbf{x} + t\sigma)dS(\sigma) \qquad (5.7)$$

$$= \frac{1}{4\pi}\int_0^\infty \varphi'(t - \rho)\left(\rho \int_{S^2} f(\mathbf{x} + \rho\sigma)dS(\sigma)\right)d\rho.$$

Comparing equations (5.6) and (5.7) we see that they coincide if $s\widetilde{\varphi}(|s|) = (-\pi/2)\varphi'(s)$ for $s \in \mathbb{R}$. Since the functions φ' and $s \mapsto s\widetilde{\varphi}(|s|)$ are odd the last equation is equivalent to

$$\widetilde{\varphi}(s) = -\frac{\pi}{2}\frac{\varphi'(s)}{s}, \text{ for } s \geq 0.$$

Thus $\Phi(\mathbf{x}) = \widetilde{\varphi}(|\mathbf{x}|)$ has the desired properties. $\qquad \square$

The left side of equation (5.3) models the temporal inaccuracy of toroidal measurements. Since, in applications only inaccurate time measurements are available, usually the inverse C^{-1} is applied to equation (5.3) which results in a blurred reconstruction of the initial pressure f.

A similar result can be derived for the circular mean of $W^{3D}(f * U)$, where $f * U$ is the initial pressure convolved with a radial function U. In order to

prove this result we introduce cylindrical coordinates (r, z, α) for each circle $c_{\mathbf{x}}$,

$$\Psi_{\mathbf{x}} : \mathbb{R}_{>0} \times \mathbb{R} \times (0, 2\pi) \to \mathbb{R}^3 \tag{5.8}$$
$$(r, z, \alpha) \to \mathbf{x} + z(v_1(\mathbf{x}) \times v_2(\mathbf{x})) + r\cos(\alpha)v_1(\mathbf{x}) + r\sin(\alpha)v_2(\mathbf{x}),$$

in such a way that the center of the circle is the origin of that coordinate system and its symmetry axis is normal to the plane $\mathbf{x} + \mathbb{R}v_1(\mathbf{x}) + \mathbb{R}v_2(\mathbf{x})$, where v_1 and v_2 are assumed to be orthonormal.

Theorem 5.2. *Let $U(\mathbf{x}) = u(|\mathbf{x}|)$ be a radially symmetric and absolute integrable function, $r_{\mathbf{x}} > 0$. Then the following relation*

$$C(U * f)(\mathbf{x}, t) = \frac{1}{2\pi} \int_{\mathbb{R}^3} w(\mathbf{x}, \mathbf{z}) \, W^{3D}(f)(\mathbf{z}, t) d\mathbf{z} \tag{5.9}$$

holds, where the weight, described in cylindrical coordinates (5.8), is given by

$$w(r, z) = \frac{1}{2\pi} \int_{-1}^{1} \frac{u(\sqrt{r_{\mathbf{x}}^2 + r^2 - 2r_{\mathbf{x}}rv + z^2})}{\sqrt{1 - v^2}} dv. \tag{5.10}$$

Proof. With the acoustic reciprocal principle, which can be found in the appendix of this thesis, we have

$$C(U * f)(\mathbf{x}, t) = \frac{1}{2\pi} \int_0^{2\pi} (W^{3D})(U * f)(c_{\mathbf{x}}(\widetilde{\alpha}), t) d\alpha$$

$$= \frac{1}{2\pi} \int_0^{2\pi} U * W^{3D}(f)(c_{\mathbf{x}}(\widetilde{\alpha}), t) d\widetilde{\alpha}$$

$$= \frac{1}{2\pi} \int_0^{2\pi} \left(\int_{\mathbb{R}^3} u(|c_{\mathbf{x}}(\widetilde{\alpha}) - \mathbf{z}|) \, W^{3D}(f)(\mathbf{z}, t) d\mathbf{z} \right) d\alpha. \tag{5.11}$$

The distance, in cylindrical coordinates, of the points $c_{\mathbf{x}}(\widetilde{\alpha})$ and $\mathbf{z}$ is given by

$$|c_{\mathbf{x}}(\widetilde{\alpha}) - \mathbf{z}|^2 = r_{\mathbf{x}}^2 + r^2 - 2r_{\mathbf{x}}r \cos(\alpha - \widetilde{\alpha}) + z^2$$

With the latter expression we have

$$C(U * f)(\mathbf{x}, t) =$$

$$\frac{1}{2\pi} \int_0^{2\pi} \int_0^{2\pi} \int_{\mathbb{R}_{>0}} \int_{\mathbb{R}} u \left(\sqrt{r_{\mathbf{x}}^2 + r^2 - 2r_{\mathbf{x}}r \cos(\alpha - \widetilde{\alpha}) + z^2} \right)$$

$$W^{3D}(f)(r, z, \alpha) r dr d\alpha dz d\widetilde{\alpha}.$$

Applying Fubini's and the Funk–Hecke theorem, see appendix, leads to

$$C(U * f)(\mathbf{x}, t) =$$

$$\frac{1}{2\pi} \int_{\mathbb{R}_{>0}} \int_{\mathbb{R}} \int_0^{2\pi} \left(\int_{-1}^1 \frac{u(\sqrt{r_\mathbf{x}^2 + r^2 - 2r_\mathbf{x} r v + z^2}) dv}{\sqrt{1 - v^2}} \right) W^{3D}(f)(r, z, \alpha, t)$$

$$d\alpha \, dr \, dz, \qquad\qquad\qquad\qquad (5.12)$$

which finishes the proof. $\qquad\qquad\qquad\qquad\qquad\qquad\qquad$ □

The last theorem shows how the function ω is computed for a known radial function U with equation (5.10). In the following we will discuss the properties of the weight function ω.

Assume that a point detector records the pressure signal of a spherical sound source. By the acoustic reciprocal principle, we know that the same signal would be measured by a spherical shaped detector, if the spherical source is replaced by a point source, see figure 5.3.
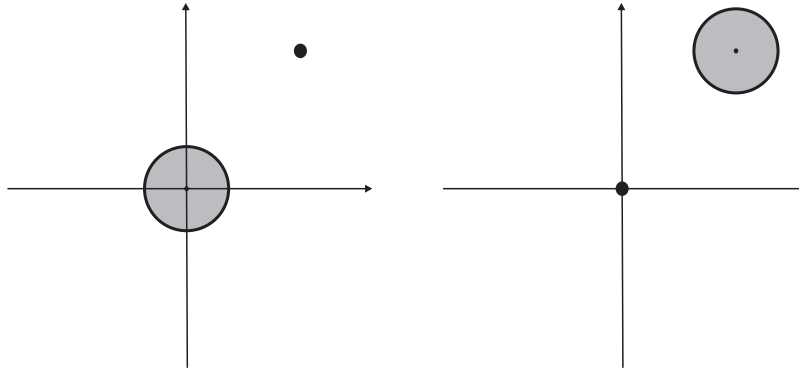
Figure 5.3: Left: A point detector, measures the signal from a spherical sound source. Right: A spherical detector, which measures the integral of acoustic pressure over its volume, records the signal emitted from a point source. According to the acoustic reciprocal principle this signals are equal.

As a consequence, a circular detector, measures the integral of the signals, measured by spherical detectors, placed along it, if the spherical source is
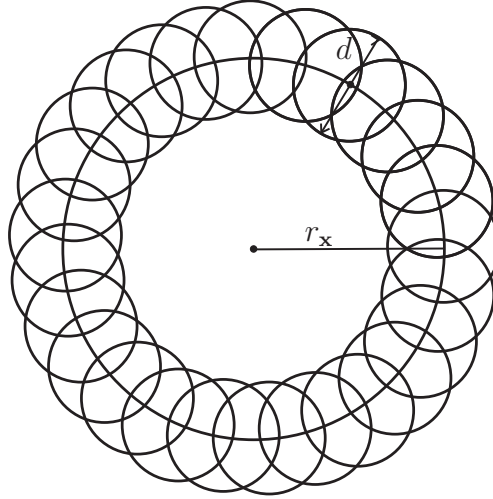
Figure 5.4: The circular annulus that results from a cross section, with the plane $z = 0$, of the family of spheres along a circle. The density of spheres nearby the inner radius is greater than the density nearby the outer radius.

interchanged by a point source. The result is a weighted integral of acoustic pressure over a torus. In figure 5.4 a cross section of the family of spheres, placed along a circle, is shown. We see that the density of the spheres nearby the inner radius of the circular annulus is greater than the density near the outer radius. This asymmetry around $r_{\mathbf{x}}$ has to be reflected by the sensitivity function ω in equation (5.9). However, an asymmetric sensitivity profile around $r_{\mathbf{x}}$ is quite natural. To appreciate this, assume that an optical fiber is bend into a toroidal loop. Bending the fiber squeezes the material on its inner and outer boundaries in an asymmetric way.

For a fixed z a reasonable sensitivity function is depicted in the lower picture in figure 5.5.

In the following we will make considerations above more rigorous. Suppose that an absolutely integrable function $u \in L^1(\mathbb{R})$ is given which is supported in the interval $[0, d]$, where $d < r_{\mathbf{x}}$ is the half width of the circular annulus in figure 5.4. Moreover we can assume that $z = 0$ since all the are the same
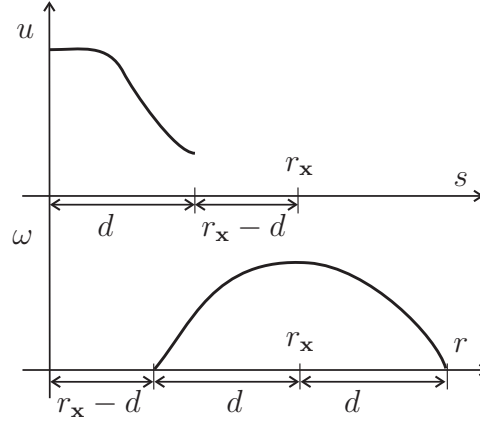
Figure 5.5: The image illustrates how ω is constructed from u according to equation (5.13).

for any z. It is not hard to figure out that the equation

$$w(r,0) = \int_{-1}^{1} \frac{u(\sqrt{r_\mathbf{x}^2 + r^2 - 2r_\mathbf{x}rv})}{\sqrt{1-v^2}}dv,$$

can be transformed into

$$\omega\left(r,0\right) = 2\int_{|r_\mathbf{x}-r|}^{r_\mathbf{x}+r} \frac{u(s)sds}{\sqrt{((r_\mathbf{x}+r)^2 - s^2)(s^2 - (r_\mathbf{x}-r)^2)}}, \tag{5.13}$$

if the new integration variable $s^2 = r_\mathbf{x}^2 + r^2 - 2r_\mathbf{x}rv$ is introduced. Further, since u is compactly supported in $[0,d]$ it can be seen from the integration limits in (5.13) and figure 5.5 that ω is supported in $[r_\mathbf{x}-d, r_\mathbf{x}+d]$. Moreover, we see from equation (5.13) that ω evaluated at $r = r_\mathbf{x} \pm \lambda$ gives

$$\omega\left(r_\mathbf{x} \pm \lambda, 0\right) = 2\int_{\lambda}^{d} \frac{u(s)sds}{\sqrt{((2r_\mathbf{x} \pm \lambda)^2 - s^2)(s^2 - \lambda^2)}},$$

which implies that ω can not be symmetric around $r_\mathbf{x}$ like explained above.

The considerations above can be used to find a function u for a sensitivity profile of a toroidal detector with desired properties. For instance, if a desired profile $w(r,0)$ should increases on the interval $[r_\mathbf{x} - d, r_\mathbf{x} - d + \varepsilon]$ and remain

almost constant on $[r_{\mathbf{x}} - d + \varepsilon, r_{\mathbf{x}} + d - \varepsilon]$ the choice $u = c\chi_{[d-\varepsilon,d]}$, for a $c > 0$, will give an ω with the desired properties.

However, it is not possible to find an u for an arbitrary sensitivity function w (for instance if ω is symmetric around $r_{\mathbf{x}}$), which means that equation (5.10) has no solution. If it has a solution we are able solve it explicitly and its solution is given in the appendix.

In the following we assume that a radial function $U(\mathbf{x}) = u(|\mathbf{x}|)$ for the sensitivity profile ω of a toroidal detector is given. By combining Theorems 5.2 and 5.1 we obtain the main result of this chapter.

Theorem 5.3. *Let $f \in \mathcal{C}_0^\infty(\Omega)$ and let φ and ω denote the impulse response and sensitivity functions of a toroidal detector. Then $C_{\varphi,w}(f) \in \operatorname{ran}(C)$ and the equation*

$$C(\Phi * U * f)(\mathbf{x}, t) = C_{\varphi,\omega}(f)(\mathbf{x}, t)$$

holds.

Proof. According to the theorems 5.2 and 5.1 we have

$$C(\Phi * U * f) = \varphi *_t C(U * f) = C_{\varphi,\omega}(f)$$

and therefore $C_{\varphi,w}(f) \in \operatorname{ran}(C)$ which concludes the proof. $\qquad\square$

Chapter 6

Numerical Results

In this chapter we present numerical results for the two step reconstruction algorithms in cylindrical and spherical geometry which were deduced in chapter 3 for the scanning geometries presented in figures 2.3 and 2.1. In both cases we simulate pressure data from a simple configuration of spheres and compute projections with respect to the families (3.25) and (3.2) with the stable reconstruction formulas which were derived in sections 3.1.3 and 3.2.4. The results show that that TAT with circular integrating detectors can be successfully implemented and provides an accurate reconstruction of the desired initial pressure.

6.1 Cylindrical stack of circles

In practice one deals with discrete measurement data

$$\mathtt{G}_\mathtt{l}[\mathtt{m},\mathtt{n}] := G_{\sigma_\mathtt{l}}(z_\mathtt{m}, t_\mathtt{n}), \qquad (\mathtt{l},\mathtt{m},\mathtt{n}) \in \{1,\ldots,\mathtt{N}_\sigma\} \times \{1,\ldots,\mathtt{N}_z\} \times \{1,\ldots,\mathtt{N}_t\},$$

where G_σ is as in (3.4), and where $\sigma_\mathtt{l} = 2\pi(\mathtt{l}-1)/\mathtt{N}_\sigma$, $z_\mathtt{m} = H(\mathtt{m}-1)/\mathtt{N}_z$ and $t_\mathtt{n} = T(\mathtt{n}-1)/\mathtt{N}_t$ are discrete samples of the angle, hight and time, respectively. Here $H > 0$ represents the finite height of the stack of circular integrating detectors (see Figure 2.1) and T is such that $G_\sigma(z,t) = 0$ for $t \geq T$ and $z \in [0, H]$.

In this section we outline how to implement (3.13) in order to find an approximation

$$\mathtt{F}_\mathtt{l}[\mathtt{m},\mathtt{n}] \simeq F_{\sigma_\mathtt{l}}(z_\mathtt{m}, r_\mathtt{n}), \qquad (\mathtt{m},\mathtt{n}) \in \{1,\ldots,\mathtt{N}_z\} \times \{1,\ldots,\mathtt{N}_r\},$$

with $r_{\mathtt{n}} = r_{\mathrm{d}}(\mathtt{n} - 1)/\mathtt{N}_r$. Having calculated such an approximation, one can reconstruct a discrete approximation to f by applying the filtered back–projection algorithm of [16] for fixed $\mathtt{m}$, see Remark 3.1.

A numerical reconstruction method based on (3.13) is as follows:

(i) The discrete Fourier transform (with respect to the first component) of the data

$$\mathtt{F}\{\mathtt{G}_{\mathtt{1}}\}\,[\mathtt{m},\mathtt{n}] := \sum_{\mathtt{m}'=1}^{\mathtt{N}_z} \mathtt{G}_{\mathtt{1}}[\mathtt{m}',\mathtt{n}]\; e^{-i2\pi\mathtt{m}(\mathtt{m}'-1)/\mathtt{N}_z} \tag{6.1}$$

with $(\mathtt{m},\mathtt{n}) \in \{-\mathtt{N}_z/2,\dots,\mathtt{N}_z/2 - 1\} \times \{1,\dots,\mathtt{N}_t\}$, is considered as an approximation to $\mathbf{F}\{F_{\sigma_1}\}\,(2\pi\mathtt{m}/H, t_{\mathtt{n}})$.

(ii) The sine transform $\mathbf{S}\{t\,\mathbf{F}\{F_{\sigma_1}\}\}$, evaluated at

$$\omega_{\mathtt{m},\mathtt{n}} = \sqrt{(2\pi\mathtt{m}/H)^2 + v_{\mathtt{n}}^2}\,, (\mathtt{m},\mathtt{n}) \in \{-\mathtt{N}_z/2,\dots,\mathtt{N}_z/2-1\}\times\{0,\dots,\mathtt{N}_r-1\}\,,$$

is approximated by the trapezoidal rule, leading to

$$\mathtt{S}\{\mathtt{tF}\{\mathtt{G}_{\mathtt{1}}\}\}\,[\mathtt{m},\mathtt{n}] := \sum_{\mathtt{n}'=1}^{\mathtt{N}_t} t_{\mathtt{n}'}\mathtt{F}\{\mathtt{G}_{\mathtt{1}}\}\,[\mathtt{m},\mathtt{n}']\sin\left(\omega_{\mathtt{m},\mathtt{n}}t_{\mathtt{n}'}\right). \tag{6.2}$$

(iii) Finally, truncating the Fourier Bessel Series and approximating the inverse Fourier transform with the trapezoidal rule leads to the following discrete version of (3.13):

$$\mathtt{F}_{\mathtt{1}}[\mathtt{m},\mathtt{n}] := \frac{4T}{\pi r_{\mathrm{d}}^3\mathtt{N}_t} \sum_{\mathtt{m}'=-\mathtt{N}_z}^{\mathtt{N}_z/2-1}\sum_{\mathtt{n}'=0}^{\mathtt{N}_r-1} \frac{v_{\mathtt{n}'}\mathtt{S}\{\mathtt{tF}\{\mathtt{G}_{\mathtt{1}}\}\}\,[\mathtt{m}',\mathtt{n}']}{\omega_{\mathtt{m}',\mathtt{n}'}^2\,J_1(r_{\mathrm{d}}v_{\mathtt{n}'})^3}J_0(r_{\mathtt{n}}v_{\mathtt{n}'})e^{-i2\pi\mathtt{m}'(\mathtt{m}-1)/\mathtt{N}_z}\,,$$
$$\tag{6.3}$$

with $(\mathtt{m},\mathtt{n}) \in \{-\mathtt{N}_z/2,\dots,\mathtt{N}_z/2 - 1\} \times \{0,\dots,\mathtt{N}_r - 1\}$.

A numerical reconstruction method using (3.13) can be obtained in an analogous manner. In this case one replaces (3.17) by

$$\mathtt{F}_{\mathtt{1}}[\mathtt{m},\mathtt{n}] := \frac{4T}{\pi r_{\mathrm{d}}^2\mathtt{N}_t} \sum_{\mathtt{m}'=-\mathtt{N}_z}^{\mathtt{N}_z/2-1}\sum_{\mathtt{n}'=0}^{\mathtt{N}_r-1} \frac{\mathtt{F}\{\mathtt{F}\{\mathtt{G}_{\mathtt{1}}\}\}\,[\mathtt{m}',\mathtt{n}']}{\omega_{\mathtt{m}',\mathtt{n}'}H_0^{(2)}(r_{\mathrm{d}}v_{\mathtt{n}'})J_0(r_{\mathrm{d}}v_{\mathtt{n}'})^2}J_0(r_{\mathtt{n}}v_{\mathtt{n}'})e^{-i2\pi\mathtt{m}'(\mathtt{m}-1)/\mathtt{N}_z}\,,$$
$$\tag{6.4}$$

which is the discrete analogue of (3.17).

To give a rough estimate of the computational complexity for the previous calculations let us assume $N_z = N_r = N_t = N_\sigma =: N$ and that the values of the sine function and the Bessel function are pre–computed and stored in lookup tables. Then the evaluation (6.1) needs $\mathcal{O}(N^2 \log N)$ floating point operations (FLOPS) whereas (6.2) and (6.3) require $\mathcal{O}(N^3)$ FLOPS. The filtered back projection formula (3.8) also requires $\mathcal{O}(N^3)$ FLOPS, see [16]. For three dimensional reconstruction (6.1), (6.2), (6.3) and the filtered back–projection formula have to be applied N times. Hence the total number of FLOPS is estimated as

$$N_{\mathrm{FLOPS}} = N\left(\mathcal{O}(N^2 \log N) + \mathcal{O}(N^3) + \mathcal{O}(N^3)\right) = \mathcal{O}(N^4).\qquad(6.5)$$

Note that three dimensional back–projection type formulas which use point measurement data have complexity $\mathcal{O}(N^5)$.

In the following numerical experiments we take $R = 0.4$, $H = 3.75$ and $T = 4$. The synthetic initial data f is assumed to be a superposition of radially symmetric objects around centers $\mathbf{x}_n$, i.e.,

$$f(\mathbf{x}) = \sum_n f_n\big(\|\mathbf{x} - \mathbf{x}_n\|\big), \qquad \mathbf{x} \in \mathbb{R}^3.$$

The acoustic pressure generated by a single radially symmetric object at position $\mathbf{x}$ and time t is given by (see [22])

$$p_n(\mathbf{x}, t) = \frac{\|\mathbf{x} - \mathbf{x}_n\| - t}{2\,\|\mathbf{x} - \mathbf{x}_n\|}\, f_n\Big(\big|\|\mathbf{x} - \mathbf{x}_n\| - t\big|\Big).\qquad(6.6)$$

By the superposition principle the total pressure is

$$p(\mathbf{x}, t) = \sum_{n=1}^{N} p_n(\mathbf{x}, t), \qquad (\mathbf{x}, t) \in \mathbb{R}^3 \times (0, \infty).\qquad(6.7)$$

The measurement data $G_\sigma(z, t) = 1/(2\pi) \int_0^{2\pi} p(\Phi_\sigma(z, r_{\mathrm{det}}, \alpha), t) d\alpha$, see (3.1), (3.27), were generated by evaluation of (6.6) followed by numerical integration over α. The radius r_{d} of the circular integrating detectors is chosen to be $2R$. In this case the stack of circular integrating detectors fully encloses the synthetic initial data f, see right image in in Figure 3.1.

Figure 6.1 shows a vertical cross section of the initial pressure f and the measurement data G_σ where Gaussian noise with a variance of 10% of the maximal data valued is added. The stack of circular integrating detectors is centered to the left of the objects. The reconstructions of F_σ with (6.3) and (6.4) from exact and noisy data are depicted in Figures 6.2 and 6.3. In the reconstructed images one notices some blurred boundaries which are limited data artifacts [38, 49] arising from the finite height of the stack of circular integrating detectors.

6.2   Array of circles of latitude on the Sphere

In this section we reconstruct a projection from the family of circles (3.25). We consider here the measurement data

$$\mathtt{G_s}[\mathtt{m},\mathtt{n}] := G_{\sigma_1}(\vartheta_\mathtt{m}, t_\mathtt{n}), \qquad (\mathtt{s},\mathtt{m},\mathtt{n}) \in \{1,\dots\mathtt{N}_\sigma\} \times \{1,\dots\mathtt{N}_\vartheta\} \times \{1,\dots\mathtt{N}_t\},$$

which are a discrete version of (3.27). Here $\sigma_\mathtt{s} = \pi(\mathtt{s}-1)/\mathtt{N}_\sigma$, $\vartheta_\mathtt{m} = \pi(\mathtt{m}-1)/\mathtt{N}_\vartheta$ and $t_\mathtt{n} = 2R(\mathtt{n}-1)/\mathtt{N}_t$ are discrete samples of the variables for which a measurement is performed. The aim is to find an approximation for the integrated initial pressure (3.3)

$$\mathtt{F_s}[\mathtt{m},\mathtt{n}] = F_{\sigma_\mathtt{s}}(r_\mathtt{n}, \vartheta_\mathtt{m}), \qquad (\mathtt{s},\mathtt{m},\mathtt{n}) \in \{1,\dots\mathtt{N}_\sigma\} \times \{1,\dots\mathtt{N}_\vartheta\} \times \{1,\dots\mathtt{N}_r\},$$

where $r_\mathtt{n} = R(\mathtt{n}-1)/\mathtt{N}_r$ and $\mathtt{N}_r = \mathtt{N}_t/2$. After such an approximation is calculated one can reconstruct a discrete approximation to f by applying the Fourier inversion formula of [6] for a fixed fixed $\mathtt{n}$.

First a discretization of formula (7.1) applied to the measurement data is given by

$$\mathtt{G_s}[\mathtt{l},\mathtt{n}] := \sum_{\mathtt{m}=1}^{\mathtt{N}_\vartheta} \mathtt{G_s}[\mathtt{m},\mathtt{n}] \; P_\mathtt{l}(\cos(\vartheta_\mathtt{m})) \sin(\vartheta_\mathtt{m}), \; l \in \{0,\dots,\mathtt{N}_\vartheta\} \qquad (6.8)$$

where the P_l are the normalized Legendre polynomials. The discrete sine transform, applied to the second component of the measurement data multiplied by t evaluated at ω_{nl} is implemented by

$$\mathtt{S}_t\left\{t\mathtt{G_s}\right\}[\mathtt{l},\mathtt{j}] := \left(\frac{2}{\pi}\right)^{1/2} \sum_{\mathtt{n}=1}^{\mathtt{N}_t} t_\mathtt{n} \mathtt{G_s}[\mathtt{l},\mathtt{n}] \; \sin\left(t_\mathtt{n}\omega_{\mathtt{l}\mathtt{j}}\right), \qquad \mathtt{j} \in \{0,\dots,\mathtt{N}_r - 1\} \,(6.9)$$

The Fourier transform with respect to the time variable is as usually implemented by

$$\mathbf{F}_t \{\mathbf{G_s}\} [\mathbf{l}, \mathbf{j}] = \left(\frac{1}{2\pi} \right)^{1/2} \sum_{n=1}^{N_t} \mathbf{G_s}[\mathbf{l}, n] \, e^{it_n \omega_{1j}}, \; \mathbf{j} \in \{ \frac{-N_t}{2}, \dots, \frac{N_t}{2} - 1 \} \quad (6.10)$$

and evaluated with the FFT algorithm. This finally leads to the discrete versions of inversion formula (3.43)

$$\mathbf{F_s}[n, m] := \sqrt{\frac{2}{\pi}} \sum_{l=0}^{N_\vartheta} \sum_{j=0}^{N_r - 1} \frac{\mathbf{S}_t \{ t \mathbf{G_s} \} [\mathbf{l}, \mathbf{j}]}{\omega_{j1}^2} \frac{j_1(r_n \omega_{j1}) P_1(\cos(\vartheta_m))}{j_{1+1}(R\omega_{j1})^3} \quad (6.11)$$

and (3.17)

$$\mathbf{F_s}[n, m] := \frac{2}{\pi} \sum_{l=0}^{N_\vartheta} \sum_{j=0}^{N_r - 1} \frac{\mathbf{F}_t \{ \mathbf{G_s} \} [\mathbf{l}, \mathbf{j}]}{\omega_{j1}^2 \, h_1^{(1)}(R\omega_{j1})} \frac{j_1(r_n \omega_{j1}) P_1(\cos(\vartheta_m))}{j_{1+1}(Rv_j)^2}. \quad (6.12)$$

We also include here short discussion of the computational complexity of the previous implementation. For simplicity assume that the same number of samples, i.e. $N_\vartheta = N_r = N_t = N_\sigma =: N$, for each variable is taken and that the values of the sine the spherical Bessel function and those of the Legendre polynomials are pre–computed and stored in lookup tables. Then the evaluation (6.1) needs $\mathcal{O}(N^2 \log N)$ floating point operations (FLOPS) whereas (6.9), (6.8), (3.43) and (3.17) require $\mathcal{O}(N^3)$ FLOPS. Applying the inversion formula (3.41) also requires $\mathcal{O}(N^3)$ FLOPS. For three dimensional imaging (6.1), (6.9),(6.8), (3.43), (or inversion formula (3.17)) and the filtered backprojection formula have to be applied N times. Thus the total number of FLOPS is estimated as

$$N_{\text{FLOPS}} = N \left(\mathcal{O}(N^2 \log N) + \mathcal{O}(N^3) + \mathcal{O}(N^3) + \mathcal{O}(N^3) \right) = \mathcal{O}(N^4). \quad (6.13)$$

which is the same amount of FLOPS like in the last section.

Numerical experiments are performed here for the values $R = 1$ and $T = 2$ are performed. The synthetic initial data f is again assumed to be a superposition of radially symmetric objects around centers $\mathbf{x}_n$. The acoustic pressure generated by each of those radially symmetric objects is given by formula (6.6) and the total pressure, by the superposition principle, is given by formula (6.7). The measurement data $G_\sigma(z, t) = 1/(2\pi) \int_0^{2\pi} p(\Phi_\sigma(R, \vartheta, \phi), t) d\phi,$

see (3.1), (3.27), were generated by evaluating of (6.6) followed by a numerical integration over ϕ.

Figure 6.4 shows a vertical cross section of the initial pressure f and the measurement data G_σ where Gaussian noise with a variance of 10% of the maximal data value is added.

The reconstructions of F_σ with (6.11) from exact and noisy data are depicted in Figure 6.5 from formula (6.11) and with formula (6.12) in Figure (6.6). Note that the reconstructed images do not have blurred boundaries. Moreover the images reconstructed with (3.43) are less sensitive to noise.
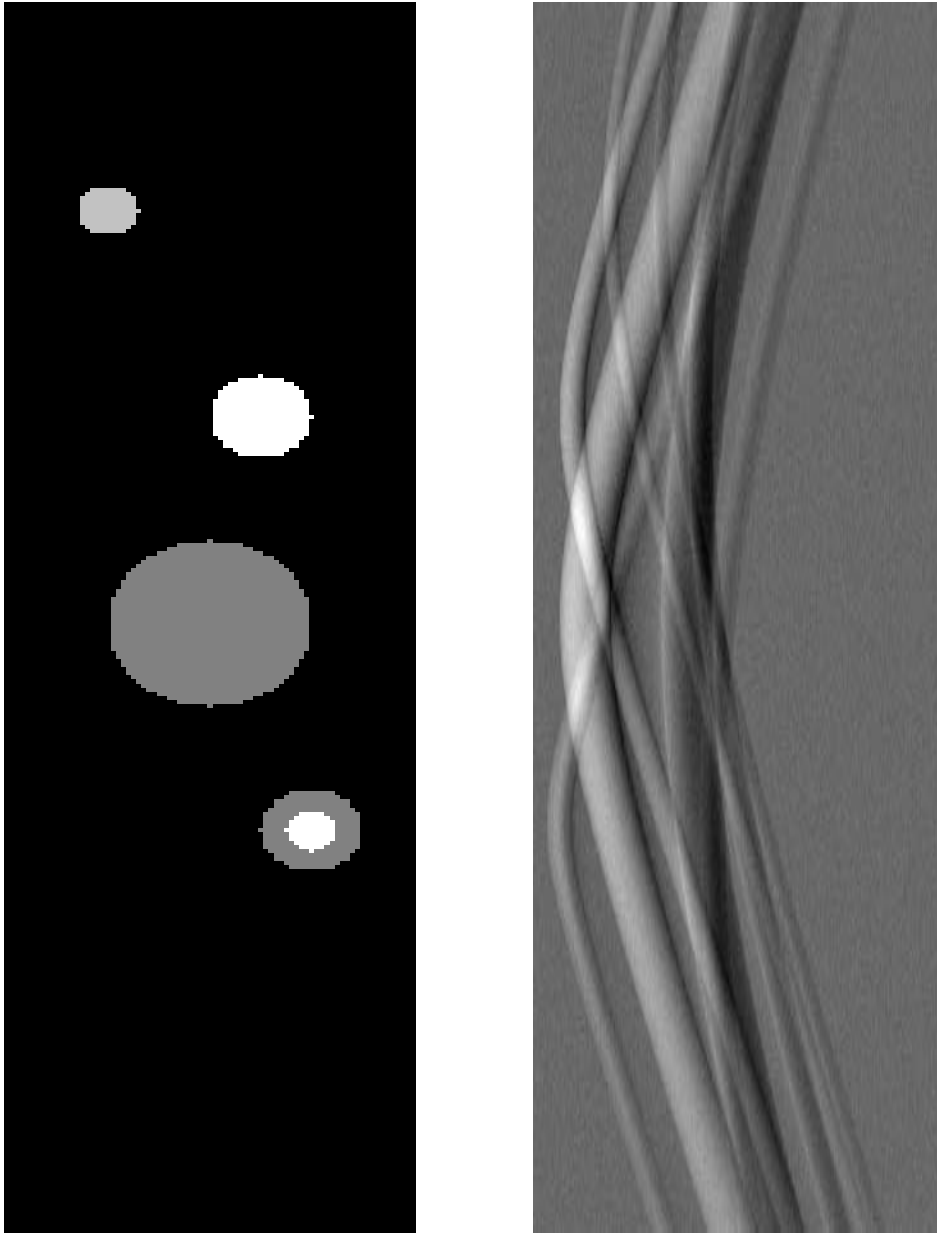
Figure 6.1: Left: Cross section of five absorbing spheres (z versus r). Right: The measurement data with 10% Gaussian noise added (z versus t).
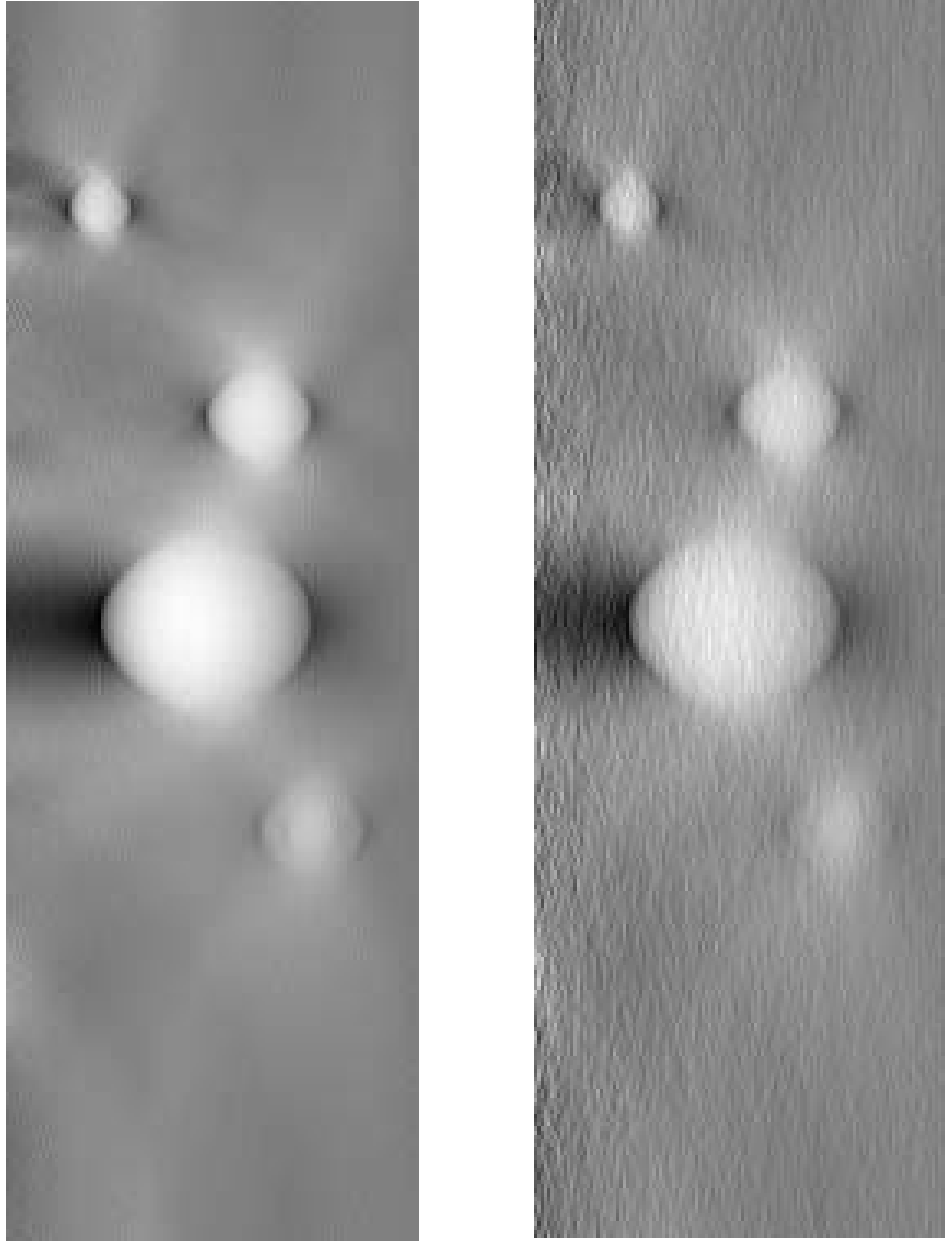
Figure 6.2: Reconstruction from simulated (left) and noisy data (right).
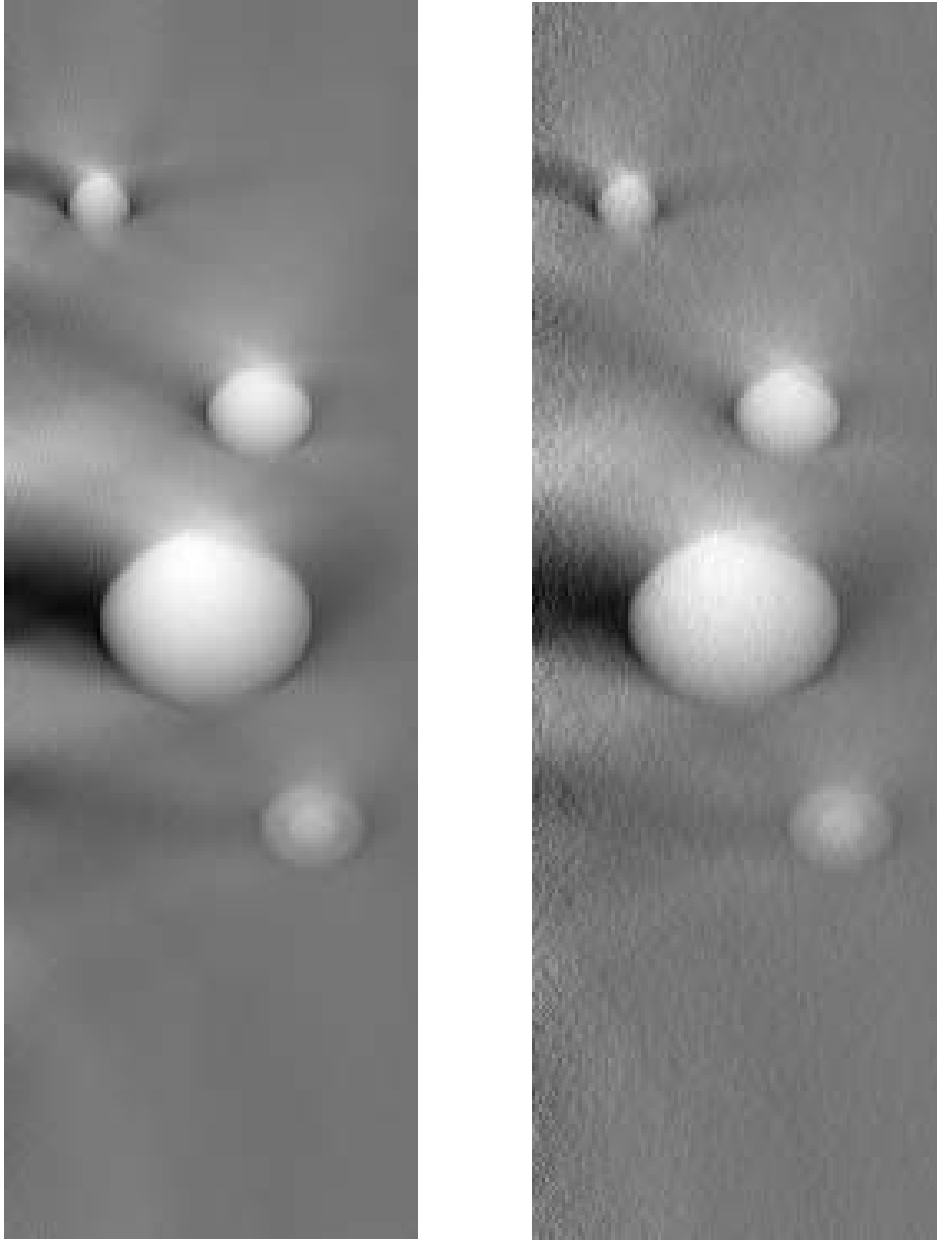
Figure 6.3: Reconstruction with (3.17) from simulated (left) and noisy data (right).
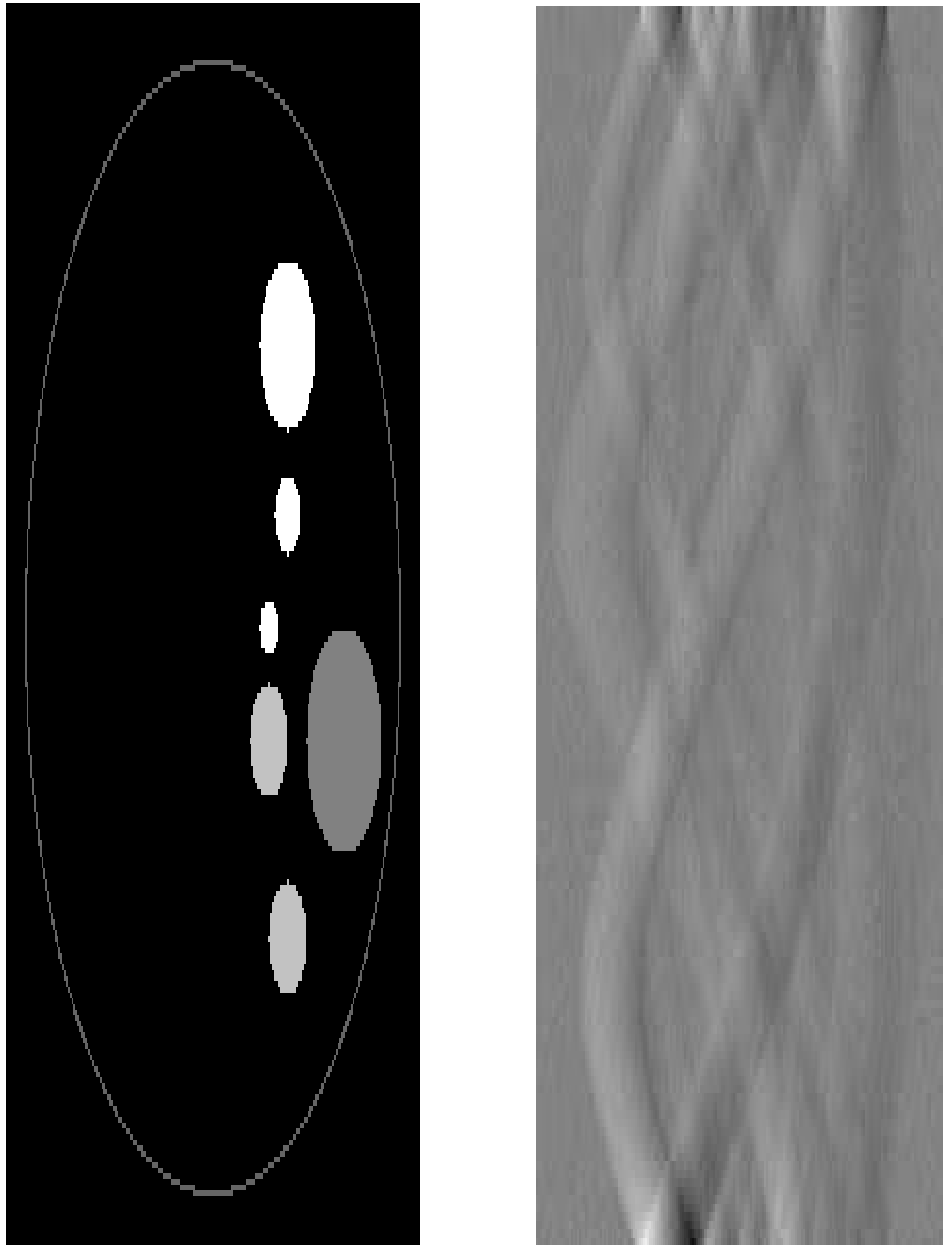
Figure 6.4: Left: Cross section of an ensemble of 6 absorbing spheres (x versus z). Right: The measurement data with 10% Gaussian noise added (ϑ versus t).
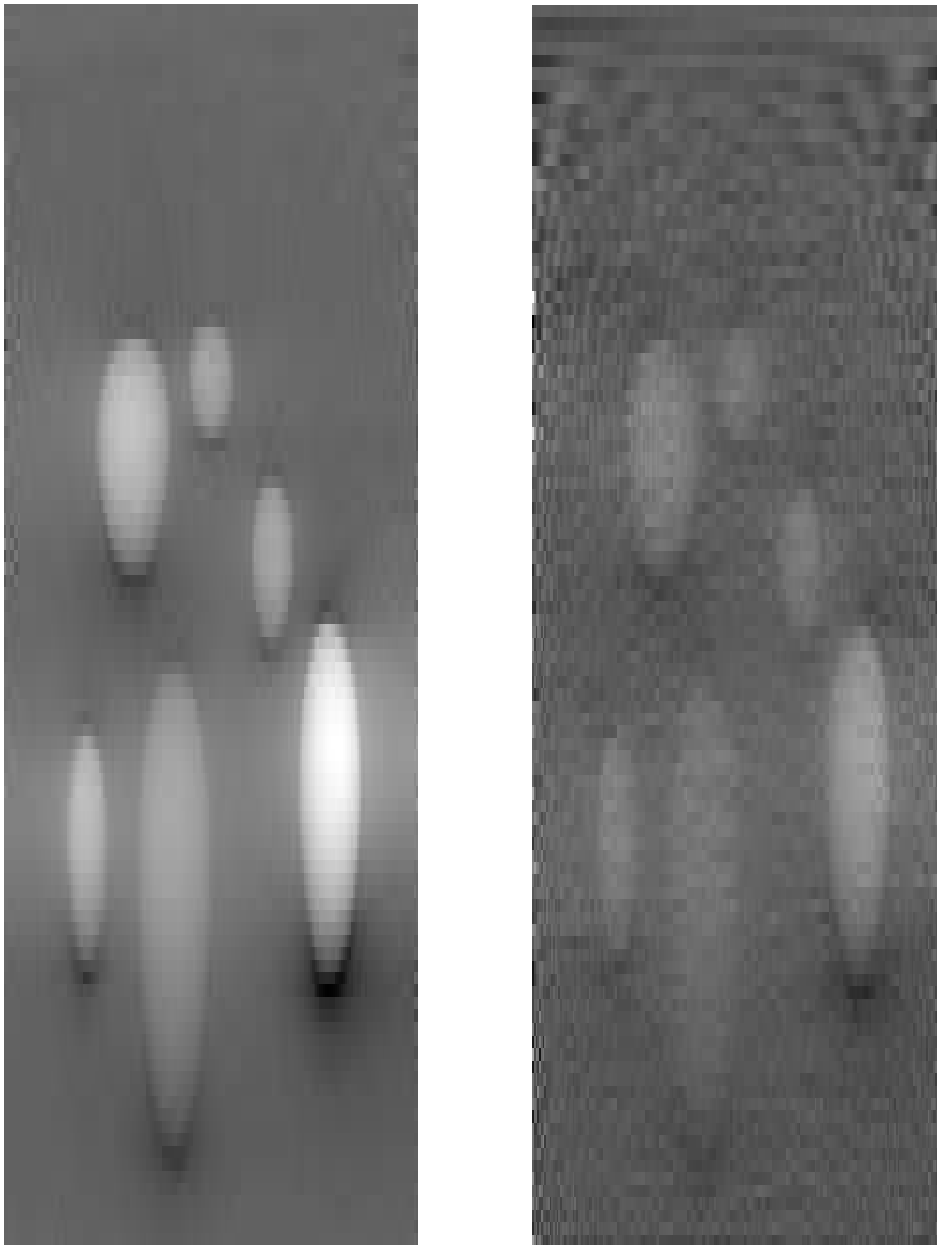
Figure 6.5: Reconstruction from simulated (left) and noisy data (right) with formula (6.3).
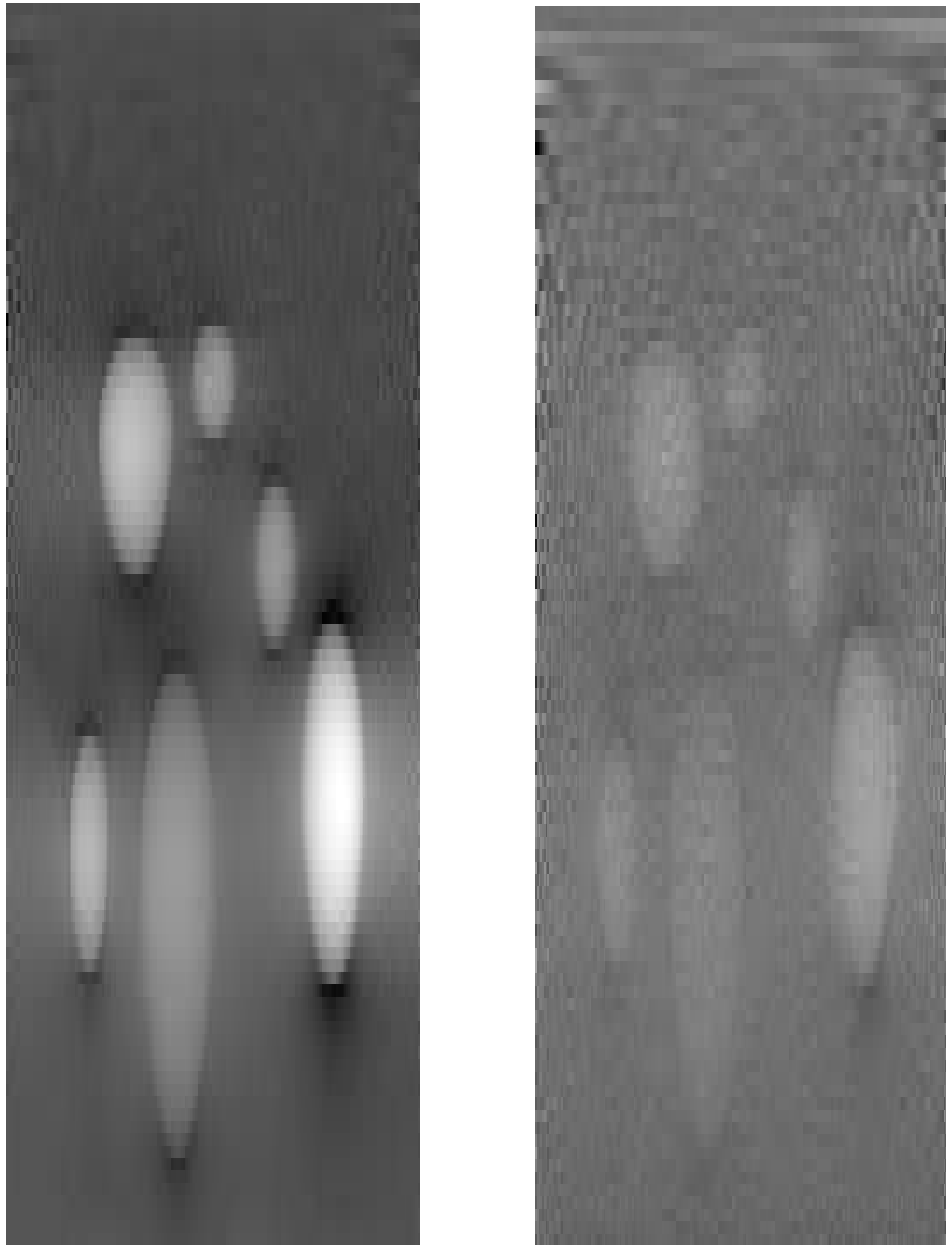
Figure 6.6: Reconstruction from simulated (left) and noisy data (right) (6.4).
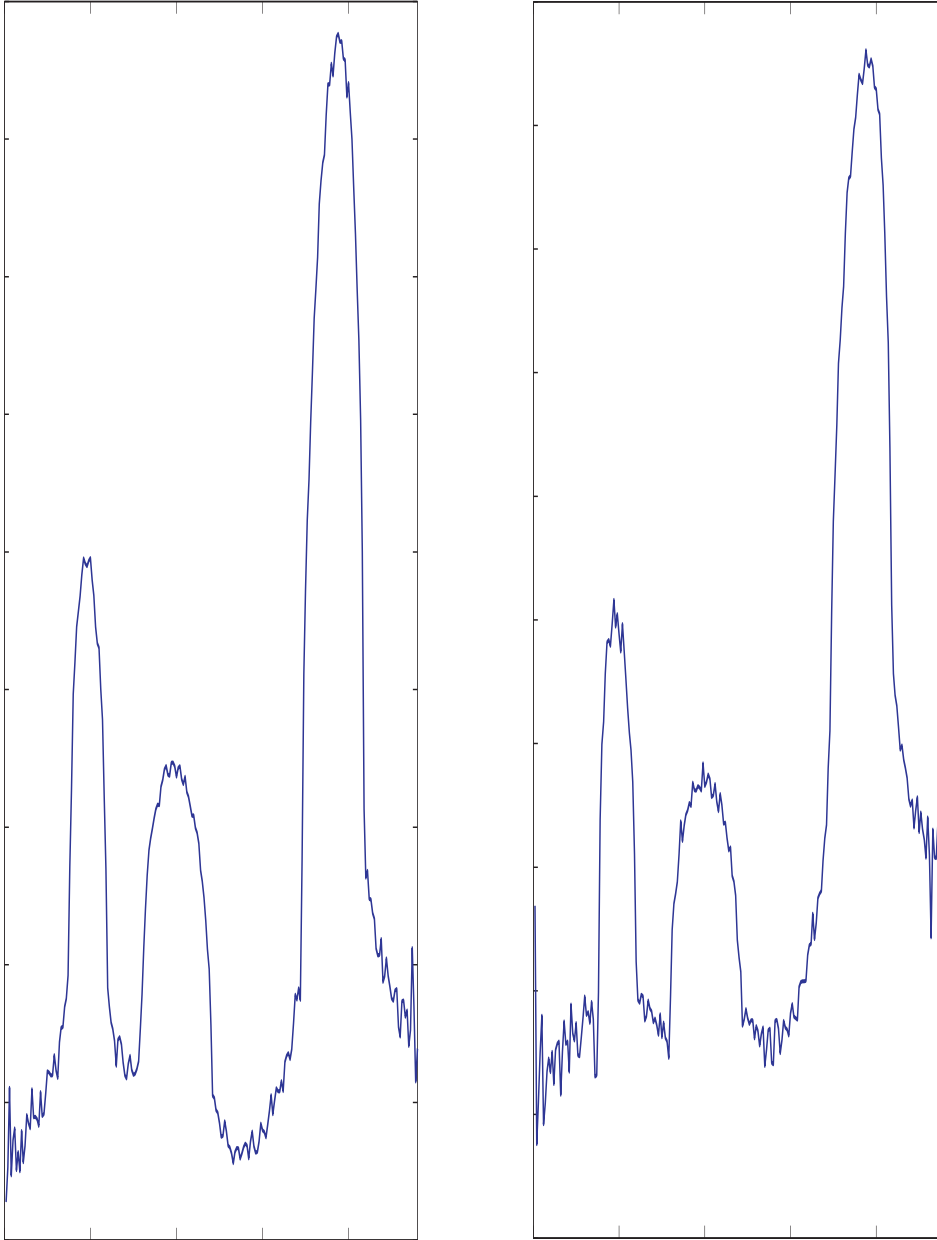
Figure 6.7: Cross section through the lower three spheres in the reconstructed images from simulated data. Left from formula (3.43) and right from formula (3.17).
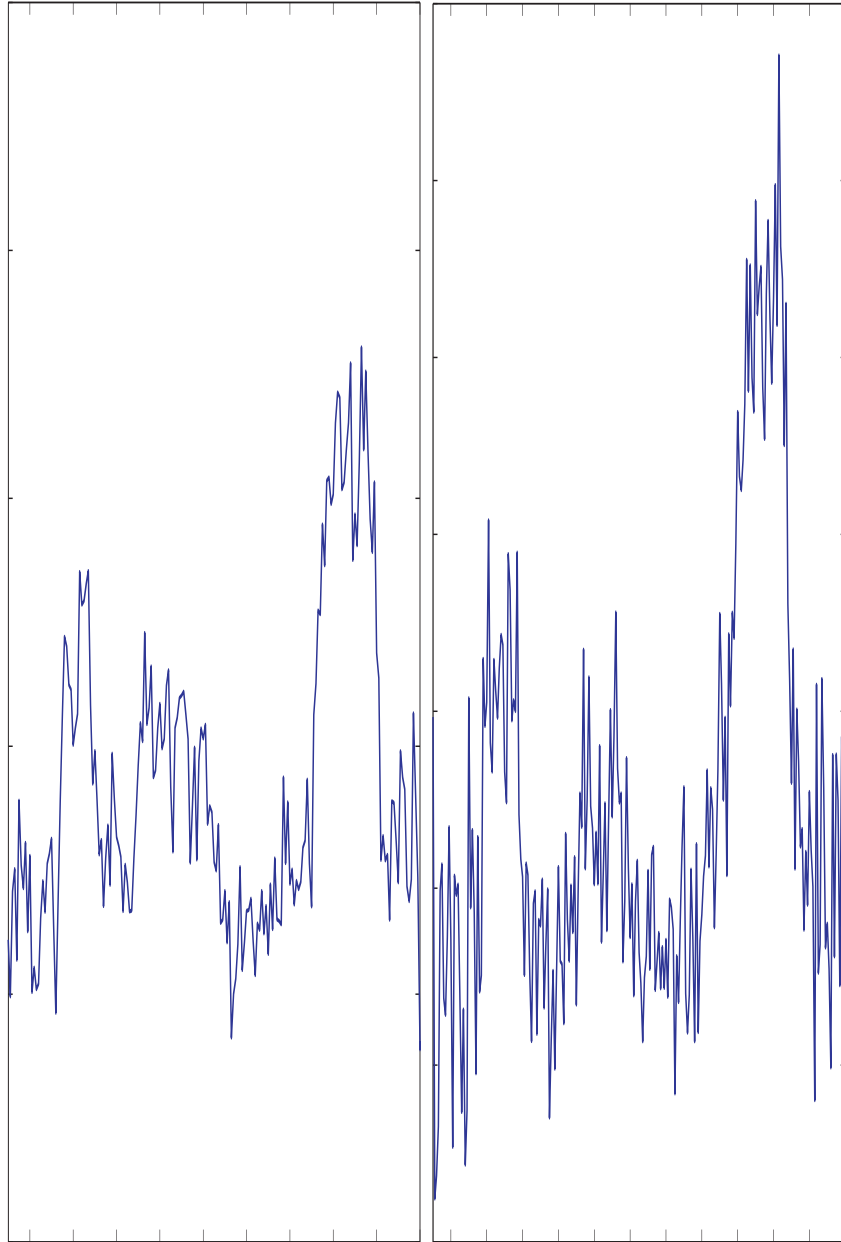
Figure 6.8: Cross section through the lower three spheres in the reconstructed images from noisy data. Left from formula (3.43) and right from formula (3.17).

Chapter 7

Appendix

Integral transforms

In the following we give a list of the integral transforms that are used in this thesis. The transforms are given by

$$\mathbf{S}\left\{\phi\right\}(\omega) := \int_0^\infty \phi(t)\sin(\omega t)dt\,, \qquad\qquad \phi \in L^1((0,\infty))\,, \omega > 0\,,$$

$$\mathbf{C}\left\{\phi\right\}(\omega) := \int_0^\infty \phi(t)\cos(\omega t)dt\,, \qquad\qquad \phi \in L^1((0,\infty))\,, \omega > 0\,,$$

$$\mathbf{F}\left\{\phi\right\}(k) := \int_\mathbb{R} \phi(z)e^{-ikz}dz\,, \qquad\qquad \phi \in L^1(\mathbb{R})\,, k \in \mathbb{R}\,,$$

$$\mathbf{H}\left\{\phi\right\}(v) := \int_0^\infty \phi(r)J_0(vr)\ rdr\,, \qquad\qquad \phi \in L^1((0,\infty), r^{1/2}dr)\,, v > 0\,,$$

$$\mathbf{H}^l\left\{\phi\right\}(\omega) := \int_0^\infty \phi(r)j_l(\omega r)\ r^2 dr\,, \qquad \phi \in L^1((0,\infty), r^2 dr)\,, \omega > 0\,,$$

$$\mathbf{M}\left\{\phi\right\}(s) := \int_0^\infty \phi(x)\ x^{s-1}dx\,, \qquad\qquad \phi \in \mathcal{C}_0(\mathbb{R}_{\geq 0})\,, s > 0\,,$$

$$\phi_l := \int_0^\pi \phi(\vartheta)P_l(\cos(\vartheta))\sin(\vartheta)d\vartheta\,, \quad \phi \in L^1((0,\pi), \sin(\vartheta)d\vartheta)\,, l \in \mathbb{N}\,,$$

where the letters denote the sine, cosine, Fourier, Hankel, spherical Hankel and Mellin transform, respectively. The value ϕ_l is the $l-$th Fourier coefficient with respect to the basis $\{P_l\}_{l \in \mathbb{N}}$ of normalized Legendre polynomials. Further, J_0 is the zero order Bessel function [1] and j_l denotes spherical Bessel function of the $l-$th order.

When the transforms above are applied to functions depending on several variables the transformed variable is added as subscript. For instance we write

$$\mathbf{H}_r \left\{ F_\sigma \right\} (z, v) = \int_0^\infty F_\sigma(z, r) J_0(vr) r \, dr, \qquad (7.1)$$

where the subscript indicates that r is transformed here.

The Mellin transforms $\mathbf{M}$ above is defined in as in [42]. Tables for the Mellin transform and its basic properties and can be found in [48, 42]. For simplicity we define the Mellin transform on the space piecewise continues and compactly supported functions, which we denote by $\mathcal{C}_0(\mathbb{R}_{\geq 0})$. The remaining integral transforms are defined on the L^1 spaces with appropriate weights.

The Mellin transform is often considered as a multiplicative version of the Fourier transform since it satisfies a multiplication theorem associated with the convolution product

$$(f * g)(s) = \int_0^\infty f(r) \, g \left(\frac{s}{r} \right) \frac{dr}{r}. \qquad (7.2)$$

According to [48, 42] we have that the Mellin transform satisfies

$$\mathbf{M}(f * g) = \mathbf{M}(f) \, \mathbf{M}(g). \qquad (7.3)$$

In several parts of this thesis the inverse integral transforms are applied in order to obtain reconstructions of the initial pressure. We explain that applying the inverse transforms is justified exemplarily with the relation that is given by equation (2.3). The general assumption that $f \in \mathcal{C}_0^\infty(\Omega)$ implies that the left side of (2.3) is a rapidly decreasing $\mathcal{C}^\infty$ function, which also implies that the right side has to be a function of the same type. Applying the inverse transforms above is justified for this class of functions.

Fourier series expansion

Consider a function $h \in L^2(\mathbb{R}^2)$ and assume $\mathbf{x} \in \mathbb{R}^2$ is given in polar coordinates $\mathbf{x} = (r\cos(\phi), r\sin(\phi))$. Then h is expanded into a Fourier series, with respect to its angular variable, by

$$h(r, \phi) = \sum_{\lambda \in \mathbb{Z}} h_\lambda(r)\, e^{i\lambda\phi}, \quad h_\lambda(r) = \int_0^{2\pi} h(r, \phi)e^{i\lambda\phi}.$$

The acoustic reciprocal principle

We prove the acoustic reciprocal principle which is used in theorem 5.2.

Theorem 7.1. *Let $f \in \mathcal{C}_0^\infty(\Omega)$ and Ψ be a compactly supported and absolutely integrable function. Then $\Psi * W^{3D}(f) = W^{3D}(f * \Psi)$.*

Proof. Using D'Alemberts formula we can write the solution of the 3D wave equation as $W^{3D}(f) = \partial_t \frac{1}{4\pi t}(f * h)$ as convolution with the distribution h given by

$$h(\mathbf{x}) = \delta(|\mathbf{x} - \mathbf{y}| - t).$$

Then the symmetry of the convolution implies

$$\Psi * W^{3D}(f) = \Psi * \partial_t \frac{1}{4\pi t}(f * h)$$
$$= \partial_t \frac{1}{4\pi t}(\Psi * f * h) = h * \partial_t \frac{1}{4\pi t}(\Psi * f) = W^{3D}(\Psi * f),$$

which concludes the proof. $\qquad\square$

Funk–Hecke theorem

We state the Funk–Hecke theorem for $n = 2$ only since this is the only case in which it is applied in this thesis.

Let h be an integrable function on $[-1, 1]$. For $n = 2$ the Funk–Hecke, see for example [41], theorem states that the equality

$$\int_0^{2\pi} h(\cos(\phi - \psi))e^{il\phi}d\phi = 2 \int_{-1}^1 h(t)T_{|l|}(t)(1 - t^2)^{-1/2}dte^{il\phi}, \qquad (7.4)$$

where $T_{|l|}$ denotes the Tchebychev polynomial of degree l, holds.

Proof of formula 5.4

We state here the proof of equation (5.4) as in [22].

Let φ be an absolute integrable function and denote by I_φ a primitive of the function $s \mapsto \varphi(\sqrt{s})$.

$$\frac{1}{4\pi} \int_{S^2} \varphi(|\rho\sigma - t\omega|)dS(\omega) = \frac{I_\varphi((\rho + t)^2) - I_\varphi((\rho - t)^2)}{4t\rho}, \qquad (7.5)$$

Proof. We compute

$$\frac{1}{4\pi} \int_{S^2} \varphi(|\rho\sigma - t\omega|)dS(\omega) = \frac{1}{4\pi} \int_{S^2} \varphi(\sqrt{\rho^2 + t^2 - 2t\rho \; (\sigma \cdot \omega)})dS(\omega)$$

$$= \frac{1}{2} \int_{-1}^1 \varphi(\sqrt{\rho^2 + t^2 - 2t\rho s})ds,$$

where the last equality follows from the Funk–Hecke theorem. Since I_φ is a primitive of $\varphi(\sqrt{s})$ it follows

$$\frac{1}{4\pi} \int_{S^2} \varphi(|\rho\sigma - t\omega|)dS(\omega) = \frac{I_\varphi(\rho^2 + t^2 - 2t\rho s)|_{-1}^1}{4t\rho}$$

$$= \frac{I_\varphi((\rho + t)^2) - I_\varphi((\rho - t)^2)}{4t\rho},$$

which finishes the proof. $\square$

Solution of equation 5.10

As it was discussed in chapter 5 integral equation (7.6)

$$\int_{-1}^{1} u\left(\sqrt{r_{\mathbf{x}}^2 + r^2 - 2trr_{\mathbf{x}} + z^2}\right) \frac{dt}{\sqrt{1-t^2}} = w\,(r,z) \qquad (7.6)$$

is not solvable for an arbitrary ω. However, in the case equation 7.6 has a solution we are able to compute it explicitly.

Theorem 7.2. *Let $r_{\mathbf{x}} > 0$ and w be an absolutely integrable function that solves 7.6. Then equation 7.6 can be transformed into the simpler integral equation*

$$\widetilde{\omega}\,(\alpha, \beta) = -2 \int_{\alpha}^{\beta} \frac{u(s)sds}{\sqrt{(\alpha^2 - s^2)\,(s^2 - \beta^2)}}. \qquad (7.7)$$

where $\alpha^2 = (r_{\mathbf{x}} + r)^2 + z^2$ and $\beta^2 = (r_{\mathbf{x}} - r)^2 + z^2$ and

$$\widetilde{w}(\alpha, \beta) = \omega\left(\frac{\alpha^2 - \beta^2}{4r_{\mathbf{x}}}, \sqrt{\left(\frac{\alpha^2}{2} + \frac{\beta^2}{2}\right)(1 - \frac{1}{2r_{\mathbf{x}}}) - r_{\mathbf{x}}}\right). \qquad (7.8)$$

Proof. After introducing the integration variable $s^2 = r_{\mathbf{x}}^2 + r^2 - 2trr_{\mathbf{x}} + z^2$ we have that $dt = -sds/(rr_{\mathbf{x}})$ and we recognize that the term $1 - t^2$ becomes

$$\frac{(2r_{\mathbf{x}}r + (r_{\mathbf{x}}^2 + r^2 + z^2 - s^2))\,((2r_{\mathbf{x}}r - (r_{\mathbf{x}}^2 + r^2 + z^2 - s^2))}{4r_{\mathbf{x}}^2 r^2}.$$

Therefore the left side of equation (7.6) transforms into

$$\int_{\sqrt{(r_{\mathbf{x}}+r)^2+z^2}}^{\sqrt{(r_{\mathbf{x}}-r)^2+z^2}} \frac{-2u(s)sds}{\sqrt{((r_{\mathbf{x}}+r)^2 - s^2 + z^2)\,(s^2 - (r_{\mathbf{x}} - r)^2 - z^2)}}.$$

Now substitute α and β like in the theorem and express r, z in terms of α, β equation (7.7) follows. $\qquad\square$

With the last theorem it follows.

Theorem 7.3. *The integral equation (7.7) can be transformed into an Abel integral equation and its solution is given by*

$$u\left(\sqrt{\alpha^2 - v^2}\right) = \frac{1}{2}\frac{d}{dv}\int_0^v \frac{k\,\widetilde{w}(\sqrt{\alpha^2 - k^2}\,)dk}{\sqrt{v^2 - k^2}}. \qquad (7.9)$$

Proof. We consider equation (7.7) for a fixed α and introduce the relations

$$\alpha^2 - \beta^2 = k^2, \qquad\qquad \alpha^2 - s^2 = p^2, \qquad\qquad (7.10)$$

$$g(p) := u\left(\sqrt{\alpha^2 - p^2}\right), \qquad h(k) := \widetilde{w}\left(\alpha, \sqrt{\alpha^2 - k^2}\right). \qquad (7.11)$$

With this relations (7.7) transforms into the simpler equation

$$h(k) = 2\int_0^k \frac{g(p)dp}{\sqrt{k^2 - p^2}}. \qquad (7.12)$$

This, is the well known Abel's integral equation. It is solvable and its solution is given by

$$g(v) = \frac{1}{2}\frac{d}{dv}\int_0^v \frac{k\,h(k)}{\sqrt{v^2 - k^2}}\,dk.$$

where the latter equation expressed in terms of u and $\widetilde{\omega}$ is given in (7.9). □

An application of theorem 3.7

Since theorem (3.7) guarantees that formulas (3.43) and (3.17) still make sense for square integrable functions it yields new series expansion formulas for the characteristic function as a byproduct. We present here such an expansion based on formula (3.17). In the following the abbreviation $\omega_n := \omega_{n0}$ is used.

Corollary 1. *The characteristic function on $[0, a]$ can be expanded as*

$$\chi_{[0,a]}(r) = \sum_{n\in\mathbb{N}}\left[e^{-i\omega(R-a)}\left(1 - ia\omega\right) - e^{-i\omega(R+a)}\left(ia\omega + 1\right)\right]\frac{j_0(r\omega_n)}{2R\omega_n^3 j_1(R\omega_n)^3}(7.13)$$

where the equality has to be understood in the L^2 sense.

Proof. Consider the pressure emitted by a characteristic sphere centered at the origin of radius a

$$p(\mathbf{x}, t) = \frac{r - t}{2r} \chi_{[0,a]} \left(|r - t| \right), \, \| \mathbf{x} \| = r.$$

In this special case the measurement data are given by $G(t, \vartheta) = P(R, \vartheta, t)$. Since there is no dependence on the angular variable ϑ in formula (3.43) it is summed over n only. Computation of the integral

$$\mathbf{F}_t \{G\} (\omega) = \int_{r_0 - a}^{R+a} \frac{R - t}{2R} e^{-i\omega t} dt \tag{7.14}$$

and inserting in (3.17) gives (7.13). $\qquad \square$

The sequence $\chi_{[0,a]}/a$ converges to the dirac measure δ in the distributional sense when a approaches 0. Using the expansion formula (7.14) and the rule of de L'hospital we have a new series expansion formula for the dirac measure given by

$$\delta(r) = \frac{2}{i} \sum_{n \in \mathbb{N}} e^{-i\omega_n R} \frac{1 + \omega_n^2}{\omega_n^3} \frac{j_0(r\omega_n)}{j_1(R\omega_n)^3}. \tag{7.15}$$

Derivation of thermoacoustic wave equation

Since all computations in this thesis rely on the mathematical model given by equations (1.1)-(1.3) we present here the standard derivation for acoustic wave propagation, caused by a short pulse of electromagnetic radiation, in an acoustically homogeneous medium.

The Model in TAT is deduced from fundamental equations in fluid dynamics [14, 40] and a heating model. The governing equations, which are based on very evident physical assumptions like the principle of mass conservation and Newton's law of motion, are the continuity and the Euler equation. If we assume a fluid with density ρ pressure p and velocity vector field v, described by twice differentiable functions, the governing equations are given by

$$\partial_t \rho + \nabla \cdot (\rho v) = 0 \tag{7.16}$$

$$\partial_t v + (v \cdot \nabla) v + \frac{1}{\rho} \nabla p = 0. \tag{7.17}$$

We assume that the considered functions depend on the arguments $\mathbf{x} \in \mathbb{R}^3$ and $t \in \mathbb{R}$, which will almost always be omitted in the notation.

Additionally let T, s and r denote differentiable functions that describe the temperature, the entropy and the energy absorbtion of the fluid. The heating model in TAT is given by the equation

$$\rho T \, \partial_t s = r. \tag{7.18}$$

Acoustic waves are small amplitude perturbations in the density field of a quiescent fluid around its static state which for tissue is assumed to be $v = 0$, ρ_0 and p_0. We model this small perturbations from the static state by the ansatz

$$
\begin{aligned}
v(\mathbf{x}, t) &= \varepsilon v_1(\mathbf{x}, t) + \dots \\
p(\mathbf{x}, t) &= p_0 + \varepsilon p_1(\mathbf{x}, t) + \dots \\
\rho(\mathbf{x}, t) &= \rho_0(\mathbf{x}) + \varepsilon \rho_1(\mathbf{x}, t) + \dots
\end{aligned} \tag{7.19}
$$

where $0 < \varepsilon << 1$. Substituting the latter equations (7.19) into the Euler equation (7.17) and the continuity equation (7.16) yields

$$\varepsilon \partial_t v_1 + \varepsilon^2 \left(v_1 \cdot \nabla \right) v_1 + \left(\frac{1}{\rho_0} - \varepsilon \frac{\rho_1}{\rho_0^2} + O(\varepsilon^2) \right) \varepsilon \nabla p_1 = 0$$

$$\varepsilon \partial_t \rho_1 + \varepsilon \nabla \cdot (\rho_0 v_1) + \varepsilon^2 \nabla (\rho_1 v_1) = 0,$$

where in the first equation the Taylor expansion

$$\frac{1}{\rho} = \frac{1}{(\rho_0 + \varepsilon \rho_1)} = \frac{1}{\rho_0} - \varepsilon \frac{\rho_1}{\rho_0^2} + O(\varepsilon^2)$$

is used. Neglecting terms of order higher than $O(\varepsilon)$ we arrive at the linearized versions of equations (7.16) and (7.17)

$$\partial_t v_1 + \frac{\nabla p_1}{\rho_0} = 0 \tag{7.20}$$

$$\partial_t \rho_1 + \nabla \cdot (\rho_0 v_1) = 0. \tag{7.21}$$

Since only a small amount of energy is absorbed by an object when it is illuminated by a rapid pulse of electromagnetic radiation its energy absorbtion function is modeled as $r(x, t) = \varepsilon r_1(\mathbf{x}, t)$ for $0 < \varepsilon << 1$. The pulse

also causes an increase of its temperature and its specific entropy which are modeled as

$$s(\mathbf{x}, t) = s_0 + \varepsilon s_1(\mathbf{x}, t)$$

$$T(s(\mathbf{x}, t), \nu(\mathbf{x}, t)) = T_0 + \varepsilon T_1(s(\mathbf{x}, t), \nu(\mathbf{x}, t)),$$

where

$$\nu(\mathbf{x}, t) = 1/\rho(\mathbf{x}, t).$$

Inserting the expressions (7.19) and the perturbation equations for $\tilde{T}$ and s above into (7.18) leads to the *linearized heat equation*

$$\rho_0 T_0 \partial_t s_1 = r_1. \tag{7.22}$$

In order to relate our heating model with the pressure we express acoustic pressure in terms of s and ν by $p(\mathbf{x}, t) = \tilde{p}(s(\mathbf{x}, t), \nu(\mathbf{x}, t))$ and use Taylor expansion of $\tilde{p}$, which is given by

$$\tilde{p}(s, \nu) = \tilde{p}(s_0 + \varepsilon s_1, 1/(\rho_0 + \varepsilon \rho_1)) = \tilde{p}(s_0 + \varepsilon s_1, \nu_0 - \varepsilon \frac{\rho_1}{\rho_0^2})$$

$$= \tilde{p}(s_0, \nu_0) + \varepsilon s_1 \partial_s \tilde{p}(s_0, \nu_0) - \varepsilon \frac{\rho_1}{\rho_0^2} \partial_\nu \tilde{p}(s_0, \nu_0) + O(\varepsilon^2).$$

By assumption the pressure satisfies the perturbation ansatz $p(\mathbf{x}, t) = p_0 + \varepsilon p_1(\mathbf{x}, t)$ and therefore also $\tilde{p}(s, \nu)$ does. Therefore we have

$$\tilde{p}(s, \nu) = \tilde{p}(s_0, \nu_0) + \varepsilon \left(s_1 \partial_{s_0} \tilde{p}(s_0, \nu_0) - \varepsilon \frac{\rho_1}{\rho_0^2} \partial_{\nu_0} \tilde{p} \right) := \tilde{p}(s_0, \nu_0) + \varepsilon \tilde{p}_1(s, \nu)$$

and comparing coefficients of order ε gives

$$s_1 = \frac{\tilde{p}_1}{\partial_s \tilde{p}} + \frac{\rho_1}{\rho_0^2} \frac{\partial_\nu \tilde{p}}{\partial_s \tilde{p}}, \tag{7.23}$$

where, according to [37, 19], the terms $\partial_\nu \tilde{p}$ and $\partial_s \tilde{p}$ are related to the *heat capacity* c_p, *thermal expansion coefficient* β and the sound speed c by the equations

$$c^2 := -\frac{1}{\rho_0^2} \partial_\nu \tilde{p}(s_0, \nu_0), \quad \partial_s \tilde{p}(s_0, \nu_0) = \frac{\tilde{T}_0 c^2 \rho_0 \beta}{c_p}.$$

With this relations we can write equation (7.23) as

$$s_1 = \frac{c_p}{\tilde{T}_0 \rho_0 \beta} \left(\frac{1}{c^2} \tilde{p}_1 - \rho_1 \right)$$

and differentiating with respect to the time and employing equation (7.22) yields

$$\frac{1}{c^2} \partial_t \tilde{p}_1 - \partial_t \rho_1 = \frac{\beta}{c_p} r_1.$$

Now rewrite $\tilde{p}_1(s(\mathbf{x}, t), \nu(\mathbf{x}, t))$ as $p(\mathbf{x}, t)$ again and apply a further differentiation with respect to the time variable and with (7.20) and (7.21) it follows that

$$\frac{1}{c^2} \partial_t^2 p_1 - \Delta p_1 = \frac{\beta}{c_p} \partial_t r. \tag{7.24}$$

In TAT the energy absorbtion function $r(\mathbf{x}, t)$ depends on the electromagnetic *radiation intensity* $I_{\text{em}}(\mathbf{x}, t)$ and the spatial varying *absorbtion coefficient* $\psi(\mathbf{x}, t)$

$$r(\mathbf{x}, t) := I_{\text{em}}(\mathbf{x}, t) \psi(\mathbf{x}). \tag{7.25}$$

Since in TAT pulsed electromagnetic radiation is used to illuminate an object we write

$$I_{\text{em}}(\mathbf{x}, t) := j(t) I(\mathbf{x}) \tag{7.26}$$

where $j(t)$ is a function which models the temporary shape of the electromagnetic pulse. Commonly $j \in \mathcal{C}^1(\mathbb{R})$ is a function of small temporal support, i.e. $\operatorname{supp} j \subset [0, \tau]$ for $\tau << 1$, which satisfies

$$\int_{\mathbb{R}} j(t) dt = 1. \tag{7.27}$$

Combining the latter equations we recognize that (7.24) can be rewritten as

$$\frac{1}{c^2} \partial_t^2 p_1 - \Delta p_1 = \frac{\beta}{c_p} I(\mathbf{x}) \psi(\mathbf{x}) \frac{dj}{dt} \tag{7.28}$$

Finally to ensure uniqueness of the latter equation we impose the initial conditions

$$p_1(\mathbf{x}, 0) = 0, \quad \frac{\partial}{\partial t} p_1(\mathbf{x}, 0) = 0. \tag{7.29}$$

The physical meaning of this initial conditions is that there is no pressure field present before the an object is illuminated which is very reasonable.

Index

absorbtion coefficient, 86
acoustic reciprocal principle, 79

circular integrating, or circular, detector, 9
circular mean transform, 19, 23, 37
continuity equation, 83
convolution, 46
cylindrical coordinates, 10, 23

D'Hospital, 27, 40, 48

electromagnetic absorbtion properties, 1
electromagnetic radiation, 1
Euler equation, 83

Fourier Bessel series, 12, 27
Fourier series expansion, 16, 79
Fourier transform, 78
Funk–Hecke theorem, 79

Green function, 30, 31

Hankel transformation, 78

impulse response function, 7, 18
initial density or initial pressure, 3
integral equation, 17, 50, 81
inverse problem, 3

Legendre polynomials, 78
linear integrating detector, 5

linearized heat equation, 85

Mellin convolution product, 78
Mellin transformation, 78

pointlike detector, 3

radiation intensity, 86
Radon transform, 7

second order Hankel function of order n, 4
sensitivity of a toroidal detector, 18, 55
Sine and Cosine transformation, 78
spherical coordinates, 39
Spherical Hankel function, 5
Spherical Hankel transformation, 78
stereographic projection, 15, 37

Tchebychev polynomial, 17, 80
toroidal detector, 18, 53

ultrasound, 1

wave equation, 3, 22, 34, 79, 83

Bibliography

[1] M. Abramowitz and I.A. Stegun. *Handbook of Mathematical Functions.* Dover, New York, 1972.

[2] M. Agranovsky and P. Kuchment. Uniqueness of reconstruction and an inversion procedure for thermoacoustic and photoacoustic tomography with variable sound speed. *Inverse Probl.*, 23(5):2089–2102, 2007.

[3] M. L. Agranovsky, K. Kuchment, and E. T. Quinto. Range descriptions for the spherical mean Radon transform. *J. Funct. Anal.*, 248(2):344–386, 2007.

[4] Mark Agranovsky and Peter Kuchment. The support theorem for the single radius spherical mean transform, 2009. arXiv:0905.1310v1.

[5] G. Ambartsoumian and P. Kuchment. A range description for the planar circular Radon transform. *SIAM J. Math. Anal.*, 38(2):681–692, 2006.

[6] L. E. Andersson. On the determination of a function from spherical averages. *SIAM J. Math. Anal.*, 19(1):214–232, 1988.

[7] S. R. Arridge. Optical tomography in medical imaging. *Inverse Probl.*, 15(2):R41–R93, 1999.

[8] S.R. Arridge, J.C. Hebden, M. Schweiger, F.E.W. Schmidt, M.E. Fry, E.M.C. Hillman, H. Dehghani, and D.T. Delpy. A method for three-dimensional time-resolved optical tomography. 11(1):2–11, 2000.

[9] T. C. Benton and H. D. Knoble. Common zeros of two bessel functions. *Mathematics of computations*, 32:533–535, 1978.

[10] P. Burgholzer, H. Grün, M. Haltmeier, R. Nuster, and G. Paltauf. Compensation of acoustic attenuation for high-resolution photoacoustic imaging with line detectors. In A.A. Oraevsky and L.V. Wang, editors, *Photons Plus Ultrasound: Imaging and Sensing 2007: The Eighth Conference on Biomedical Thermoacoustics, Optoacoustics, and Acousto-optics*, volume 6437 of *Proceedings of SPIE*, page 643724. SPIE, 2007.

[11] P. Burgholzer, C. Hofer, G. Paltauf, M. Haltmeier, and O. Scherzer. Thermoacoustic tomography with integrating area and line detectors. *IEEE Trans. Ultrason., Ferroeletr., Freq. Control*, 52(9):1577–1583, September 2005.

[12] P. Burgholzer, G. J. Matt, M. Haltmeier, and G. Paltauf. Exact and approximate imaging methods for photoacoustic tomography using an arbitrary detection surface. *Phys. Rev. E*, 75(4):046706, 2007.

[13] W. F. Cheong, S. A. Prahl, and A. J. Welch. A review of the optical properties of biological tissues. *IEEE J. Quantum Electron.*, 26(12):2166–2185, 1990.

[14] A. J. Chorin and J. E. Marsden. *A Mathematical Introduction to Fluid Mechanics*. Springer Verlag, New York, 3. edition, 1993.

[15] R. O. Esenaliev, I. V. Larina, K. V. Larin, D. J. Deyo, M. Motamedi, and D. S. Prough. Optoacoustic technique for noninvasive monitoring of blood oxygenation: a feasibility study. *App. Opt.*, 41(22):4722–4731, 2002.

[16] D. Finch, M. Haltmeier, and Rakesh. Inversion of spherical means and the wave equation in even dimensions. *SIAM J. Appl. Math.*, 68(2):392–412, 2007.

[17] D. Finch and Rakesh. The spherical mean value operator with centers on a sphere. *Inverse Probl.*, 23(6):37–49, 2007.

[18] M. Haltmeier, O. Scherzer, P. Burgholzer, R. Nuster, and G. Paltauf. Thermoacoustic tomography and the circular Radon transform: exact inversion formula. *Math. Models Methods Appl. Sci.*, 17(4):635–655, 2007.

[19] M. Haltmeier, O. Scherzer, P. Burgholzer, and G. Paltauf. Thermoacoustic computed tomography with large planar receivers. *Inverse Problems*, 20(5):1663–1673, 2004.

[20] M. Haltmeier, O. Scherzer, and G. Zangerl. Influence of detector bandwidth and detector size to the resolution of photoacoustic tomagraphy. In F. Breitenecker and I. Troch, editors, *Argesim Report no. 35: Proceedings Mathmod 09 Vienna*, pages 1736–1744, 2009.

[21] M. Haltmeier, O. Scherzer, and G. Zangerl. A reconstruction algorithm for photoacoustic imaging based on the nonuniform FFT. *IEEE Trans. Med. Imag.*, 28(11):1727–1735, November 2009.

[22] M. Haltmeier, T. Schuster, and O. Scherzer. Filtered backprojection for thermoacoustic computed tomography in spherical geometry. *Math. Methods Appl. Sci.*, 28(16):1919–1937, 2005.

[23] M. Haltmeier and G. Zangerl. Spatial resolution in photoacoustic tomography: Effects of detector size and detector bandwidth. Technical Report 30, 2010.

[24] S. Helgason. *The Radon Transform*, volume 5 of *Progress in Mathematics*. Birkhäuser, Boston, second edition, 1999.

[25] Y. Hristova, P. Kuchment, and L. Nguyen. Reconstruction and time reversal in thermoacoustic tomography in acoustically homogeneous and inhomogeneous media. *Inverse Problems*, 24(5):055006 (25pp), 2008.

[26] F. John. *Partial Differential Equations*, volume 1 of *Applied Mathematical Sciences*. Springer Verlag, New York, fourth edition, 1982.

[27] W. Joines, Y. Zhang, C. Li, and Jirtle R. The measured electrical properties of normal and malignant human tissues from 50 to 900 mhz. *Med. Phys.*, 21:547–550, 1994.

[28] R. Kowar. Causality analysis of waves and wave equations obeying attenuation. Technical Report 6, 2009.

[29] R. Kowar, O. Scherzer, and X. Bonnefond. Frequency dependent attenuation revisited. Technical Report 16, 2009.

[30] R. A. Kruger, W. L. Kiser, D. R. Reinecke, G. A. Kruger, and K. D. Miller. Thermoacoustic molecular imaging of small animals. *Mol. Imaging*, 2(2):113–123, 2003.

[31] R. A. Kruger, P. Lui, Y. R. Fang, and R. C. Appledorn. Photoacoustic ultrasound (PAUS)—reconstruction tomography. *Med. Phys.*, 22(10):1605–1609, 1995.

[32] R. A. Kruger, K. D. Miller, H. E. Reynolds, W. L. Kiser, D. R. Reinecke, and G. A. Kruger. Breast cancer in vivo: contrast enhancement with thermoacoustic CT at 434 MHz-feasibility study. *Radiology*, 216(1):279–283, 2000.

[33] R. A. Kruger, D. R. Reinecke, and G. A. Kruger. Thermoacoustic computed tomography – technical considerations. *Med. Phys.*, 26:1832–1837, 1999.

[34] P. Kuchment and L. A. Kunyansky. Mathematics of thermoacoustic and photoacoustic tomography. *European J. Appl. Math.*, 19:191–224, 2008.

[35] L. A. Kunyansky. Explicit inversion formulae for the spherical mean Radon transform. *Inverse Probl.*, 23(1):373–383, 2007.

[36] L. A. Kunyansky. A series solution and a fast algorithm for the inversion of the spherical mean radon transform. *Inverse Probl.*, 23(6):S11–S20, 2007.

[37] L. D. Landau and E. M. Lifschitz. *Lehrbuch der theoretischen Physik, Band VI: Hydrodynamik*. Akademie Verlag, Berlin, 1991.

[38] A. K. Louis and E. T. Quinto. Local tomographic methods in sonar. In *Surveys on solution methods for inverse problems*, pages 147–154. Springer, Vienna, 2000.

[39] P.M. Morse and H. Feshbach. *Methods of Theoretical Physics*. McGraw-Hill Book Co., New York, 1953. 2 volumes.

[40] H. J. Davies N. Curle. *Modern Fluid Dynamics*, volume 1. D. Van Nostrand Company LTD London, 1968.

[41] F. Natterer. *The Mathematics of Computerized Tomography*. Teubner, Stuttgart, 1986.

[42] F. Natterer. *The Mathematics of Computerized Tomography*, volume 32 of *Classics in Applied Mathematics*. SIAM, Philadelphia, 2001.

[43] S. J. Norton. Reconstruction of a two-dimensional reflecting medium over a circular domain: Exact solution. *J. Acoust. Soc. Amer.*, 67(4):1266–1273, 1980.

[44] R. Nuster, Hollota M., H. Grossauer, P. Burgholzer, and G. Paltauf. Photoacoustic micro-tomography using optical interferometric detection. Technical Report 19, 2009.

[45] V. P. Palamodov. *Reconstructive Integral Geometry*, volume 98 of *Monographs in Mathematics*. Birkhäuser Verlag, Basel, 2004.

[46] G. Paltauf, P. Burgholzer, M. Haltmeier, and O. Scherzer. Thermoacoustic tomography using optical line detection. In C. D. Depeursinge, editor, *Novel Optical Instrumentation for Biomedical Applications II*, volume 5864 of *Proceedings of SPIE*, page 586402. SPIE, 2005.

[47] G. Paltauf, R. Nuster, M. Haltmeier, and P. Burgholzer. Photoacoustic tomography using a Mach-Zehnder interferometer as an acoustic line detector. *App. Opt.*, 46(16):3352–3358, 2007.

[48] A. Polyanin and A. Manzhirov. *Handbook of Integral Equations*. Mathematics in Science and Engineering. CRC Press, London, Nwe York, Washington D.C., 1998.

[49] E. T. Quinto. Singularities of the X-ray transform and limited data tomography in $\mathbf{R}^2$ and $\mathbf{R}^3$. *SIAM Journal on Mathematical Analysis*, 24(5):1215–1225, 1993.

[50] O. Scherzer, M. Grasmair, H. Grossauer, M. Haltmeier, and F. Lenzen. *Variational methods in imaging*, volume 167 of *Applied Mathematical Sciences*. Springer, New York, 2009.

[51] M. Schweiger, S.R. Arridge, and D.T. Delpy. Application of the finite-element method for the forward and inverse models in optical tomography. *J. Math. Imaging Vision*, 3(4):263–283, 1993.

[52] I. N. Sneddon. *The Use of Integral Transforms*. McGraw-Hill, New York, 1972.

[53] V. V. Volchov. *Integral Geometry and Convolution Equations*. Kluwer Academic Publishers, The Netherlands, 2003.

[54] M. Xu and L. V. Wang. Exact frequency-domain reconstruction for thermoacoustic tomography–I: Planar geometry. *IEEE Trans. Med. Imag.*, 21:823–828, 2002.

[55] M. Xu and L. V. Wang. Time-domain reconstruction for thermoacoustic tomography in a spherical geometry. *IEEE Trans. Med. Imag.*, 21(7):814–822, 2002.

[56] M. Xu and L. V. Wang. Analytic explanation of spatial resolution related to bandwidth and detector aperture size in thermoacoustic or photoacoustic reconstruction. *Phys. Rev. E*, 67(5):0566051–05660515 (electronic), 2003.

[57] M. Xu and L. V. Wang. Universal back-projection algorithm for photoacoustic computed tomography. *Phys. Rev. E*, 71(1):0167061–0167067 (electronic), 2005.

[58] M. Xu, Y. Xu, and L. V. Wang. Time-domain reconstruction algorithms and numerical simulations for thermoacoustic tomography in various geometries. *IEEE Trans. Biomed. Eng.*, 50(9):1086–1099, 2003.

[59] Minghua Xu and Lihong V. Wang. Time-domain reconstruction for thermoacoustic tomography in a spherical geometry. *Med. Phys.*, 21(7):814–822, 2002.

[60] Y. Xu, M. Xu, and L. V. Wang. Exact frequency-domain reconstruction for thermoacoustic tomography–II: Cylindrical geometry. *IEEE Trans. Med. Imag.*, 21:829–833, 2002.

[61] X. Yang and L. V. Wang. Ring-based ultrasonic virtual point detector with applications to photoacoustic tomography. *Applies Physics Letters*, 90(25):251103, 2007.

[62] G. Zangerl, M. Haltmeier, and O. Scherzer. Cylindrical coordinates in thermoacoustic tomography. In *IPDO Symposium on inverse problems, design and optimization, Miami, Florida*, 2007.

[63] G. Zangerl and O. Scherzer. Exact reconstruction in photoacoustic to-
     mography with circular integrating detectors ii: Spherical geometry.
     Math. Methods Appl. Sci., page to appear, 2010.

[64] G. Zangerl, O. Scherzer, and M. Haltmeier. Circular integrating detec-
     tors in photo and thermoacoustic tomography. *Inverse Probl. Sci. Eng.*,
     17(1):133–142, 2009.

[65] G. Zangerl, O. Scherzer, and M. Haltmeier. Exact series reconstruc-
     tion in photoacoustic tomography with circular integrating detectors.
     Commun. Math. Sci., 7(3):665–678, 2009.

ATTACHMENT

INFLUENCE OF DETECTOR BANDWIDTH AND DETECTOR SIZE TO THE RESOLUTION OF PHOTOACOUSTIC TOMOGRAPHY

Markus Haltmeier[1], Otmar Scherzer[1,2], Gerhard Zangerl[1]

[1]Department of Mathematics, University of Innsbruck, Austria,

[2]Radon Institute of Computational and Applied Mathematics, Linz, Austria

Corresponding author: Markus Haltmeier, University of Innsbruck, Department of Mathematics, 6020 Innsbruck, Technikerstraße 21a, Austria, `markus.haltmeier@uibk.ac.at`

Abstract.   High spatial resolution is one of the major aims in photoacoustic tomography. Two main factors limiting the resolution of photoacoustic tomography are the detector size and the finite bandwidth of the ultrasound detection system. We present a quantitative analysis of those effects for "approximate point detectors" and for "approximate line detectors".

Keywords. Photoacoustic tomography; image reconstruction; wave equation; resolution; bandwidth.

AMS classifications. 44A12, 65R32, 35L05, 92C55.

1   Introduction

Photoacoustic tomography (PAT) is a novel imaging method for visualizing the electromagnetic absorption coefficient of a medium at low frequencies. It is based on the excitation of high bandwidth acoustic waves by illuminating a probe with pulsed electromagnetic energy, and combines the advantages of optical (high contrast) and ultrasonic imaging. We refer the reader to [22, Section 1.5] for a detailed mathematical description. PAT has proven great promise for a variety of biomedical applications, such as imaging of animals [15, 23], early cancer diagnostics [16, 19], and imaging of vasculature [4, 14]
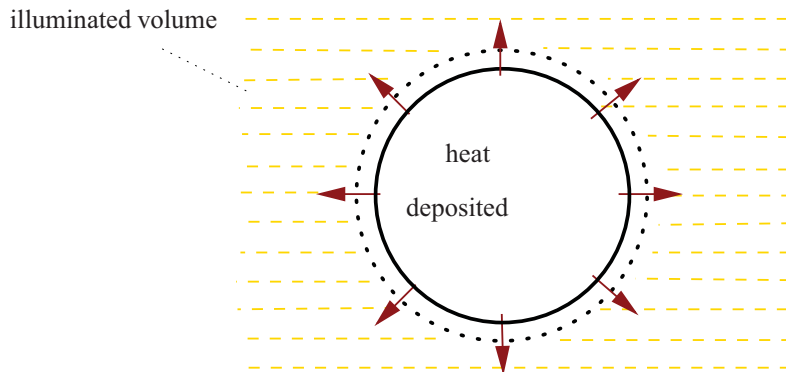
Figure 1: Thermoelastic effect: Parts of a specimen are illuminated with electromagnetic energy and react with expansion

If a probe is illuminated with a short pulse of non-ionizing electromagnetic radiation, it absorbs a fraction of energy, heats up, and reacts with an expansion (the so called thermoelastic effect; see figure 1). This in turn induces an acoustic wave, which is recorded outside of the object. Other than in conventional ultrasound imaging, where the source of the acoustic wave is an external transducer, in PAT the source is the imaged object itself. The frequency bandwidth of the recorded signals is therefore generally broad and depends on the size and the shape of illuminated structures.

If we assume that the probe is acoustically homogeneous, then the excited acoustic pressure $p : \mathbb{R}^3 \times (0,\infty) \to \mathbb{R}$ satisfies

$$\left(\partial_t^2 - \Delta\right) p(\mathbf{x},t) = 0, \qquad\qquad (\mathbf{x},t) \in \mathbb{R}^3 \times (0,\infty), \qquad (1a)$$

$$p(\mathbf{x},0) = f(\mathbf{x}), \partial_t p(\mathbf{x},0) = 0, \qquad\qquad \mathbf{x} \in \mathbb{R}^3, \qquad (1b)$$

where Δ denotes the Laplacian with respect to the spatial variable $\mathbf{x}$ and ∂_t is the derivative with respect to the temporal variable t. For simplicity of presentation we assume throughout that $f \in C_c^\infty(B_R)$, where $B_R \subset \mathbb{R}^3$ is the ball with radius R centered at the origin. Here and in the following, $C_c^\infty(\Omega)$ denotes the space of all smooth functions $f : \mathbb{R}^3 \to \mathbb{R}$ with have compact support in the set $\Omega \subset \mathbb{R}^3$.

In the following we denote by $\mathscr{W}^{3D} : C_c^\infty(\mathbb{R}^3) \to C^\infty(\mathbb{R}^3 \times (0,\infty))$ the operator that takes smooth compactly supported initial data to the solution of (1a), (1b). The goal of PAT is to reconstruct the initial pressure f (representing the probe) from measurements of $(\mathscr{W}^{3D} f)(\mathbf{x},t)$ taken outside of B_R.
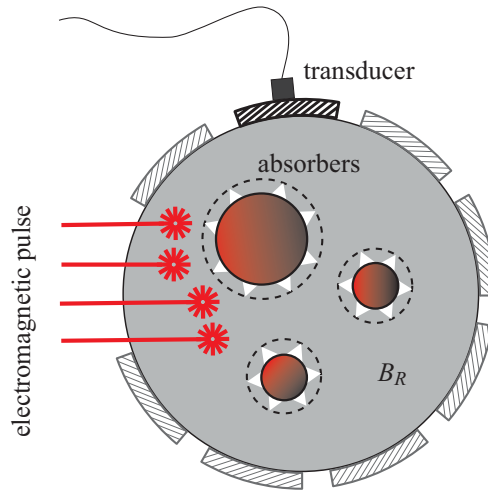
Figure 2: Photoacoustic tomography with piezoelectric transducer as an "approximate point detector".

1.1 Approximate point-detectors

The classical approach in PAT is to assume that point data

$$(\mathbf{P}f)(\mathbf{z},t) := g(\mathbf{z},t) := (\mathscr{W}^{3D}f)(\mathbf{z},t), \qquad (\mathbf{z},t) \in \partial B_R \times (0,\infty),$$

are given (∂B_R denotes the boundary of B_R). The operator $\mathbf{P} : C_c^\infty(B_R) \to C^\infty(\partial B_R \times (0,\infty))$ that maps a compactly supported initial data to the data measured by an ideal point detector can be inverted uniquely [1, 2]. In [6, 7] it is shown that $\mathbf{P}$ is an isometry with respect to the inner products $\int_{B_r} f_1 f_2$ and $2/R \int_{\partial B_R \times (0,\infty)} t g_1 g_2$ on $C_c^\infty(B_R)$ and $C^\infty(\partial B_R \times (0,\infty))$, respectively. The inversion is therefore even stable with respect to the L^2 topologies. Exact expressions for its inverse

$$\mathbf{P}^{-1} : \mathrm{ran}(\mathbf{P}) \subset C^\infty(\partial B_R \times (0,\infty)) \to C_c^\infty(B_R)$$

are derived in [6, 17, 25]. Here and in the following $\mathrm{ran}(\mathbf{P}) := \{\mathbf{P}f : f \in C_c^\infty(B_R)\}$ denotes the range of $\mathbf{P}$.

In practical applications, the detection system has a finite bandwidth. Moreover, standard ultrasound transducers, which integrate the pressure over its surface, are used to approximate point data. If we assume that the transducer surface is part of the measurement surface and rotationally symmetric (see Fig. 2), then the measured data are given by

$$(\mathbf{P}_{\phi,w}f)(\mathbf{z},t) = \left[\phi *_t \int_{\partial B_R} w\left(|\mathbf{z} - \mathbf{z}'|\right) (\mathscr{W}^{3D}f)(\mathbf{z}',\cdot)\, dS(\mathbf{z}') \right](t), \qquad (\mathbf{z},t) \in \partial B_R \times (0,\infty).$$

Here $w(r)$ represents the sensitivity of the detector surface, $\phi(t)$ denotes the impulse response function of the ultrasound detection system, and $*_t$ is the convolution with respect to t.

Insufficient knowledge of w and ϕ, as well as the severe ill-posedness of deblurring problems make it impossible to stably invert $\mathbf{P}_{\phi,w}$. It is therefore common to apply the exact inverse of $\mathbf{P}$ to the data $\mathbf{P}_{\phi,w}f$. This results in a blurred reconstruction, where the blurring depends, e.g., on the detector size. Exact blurring kernels will be given in Subsection 1.3.

1.2 Approximate line-detectors

In order to partly overcome the size and shape limitations of point detectors, in [3, 11, 21] we propose PAT with line integrals

$$(\mathbf{L}f)(\mathbf{z},t) := \int_{\ell_{\mathbf{z}}} (\mathscr{W}^{3D}f)(\mathbf{x},t)\, dS(\mathbf{x}), \qquad (\mathbf{z},t) \in \partial B_R \times (0,\infty),$$

where $\ell_{\mathbf{z}}$ is the unique line passing through $\mathbf{z}$, being tangential to ∂B_R, and orthogonal to $\mathbf{e}_3$. The inversion of $\mathbf{L}$ requires a two step reconstruction procedure:

- For fixed orientation of $\ell_{\mathbf{z}}$, the data $(\mathbf{L}f)(\mathbf{z},t)$ is the solution of the two dimensional wave equation where the initial data are given by the linear projection of f in that direction [11]. Hence linear projections of f can be obtained by recovered the initial data of the two dimensional wave equation from values of its solution on a circle.

- In a second stage, a three dimensional image is reconstructed from the projection images by applying the inverse two dimensional classical Radon transform in planes orthogonal to the rotation axis.
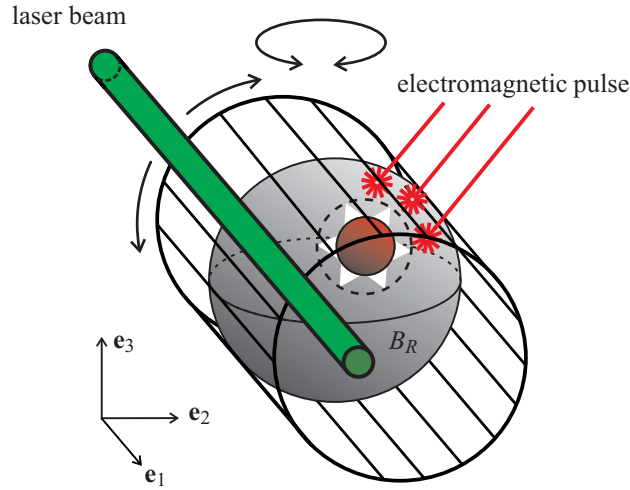
Figure 3: Photoacoustic tomography with a laser beam as "approximate line detector".

The operator $\mathbf{L} : C_c^\infty(B_R) \to C^\infty(\partial B_R \times (0,\infty))$ that maps a compactly supported initial data to the data measured by an ideal line detector can be inverted uniquely. Exact inversion formulas have been derived in [5, 11, 17, 18].

In practical applications the line detector is approximated by a cylindrically symmetric laser beam that is part of an interferometric setup (see Fig. 3). Such a laser naturally integrates the pressure over its volume [9, 21], and thus

$$(\mathbf{L}_{\phi,w} f)(\mathbf{z},t) = \left[\phi *_t \int_{\mathbb{R}^3} w\big(\mathrm{dist}(\ell_{\mathbf{z}}, \mathbf{x})\big) (\mathscr{W}^{3D} f)(\mathbf{x},t) d\mathbf{x}\right], \qquad (\mathbf{z},t) \in \partial B_R \times (0,\infty)$$

are the actually available data. Here $w(r)$ represents the radial profile of the detecting laser beam, $\phi(t)$ is the impulse response function of the ultrasound detection system, and $\mathrm{dist}(\ell_{\mathbf{z}}, \mathbf{x})$ denotes the distance between line $\ell_{\mathbf{z}}$ and point $\mathbf{x}$.

Again, application of $\mathbf{L}^{-1} : \mathrm{ran}(\mathbf{L}) \to C_c^\infty(B_R)$ to the data $\mathbf{L}_{\phi,w} f$ leads to a blurred reconstruction. However, the laser beam can be made very thin, suggesting that the one dimension approximation with approximate line detectors gives less blurred images than the zero dimension approximation with approximate point detectors. Our aim is to make such statements precise, by calculating analytical blurring kernels and to investigate the resolution for both kind of detectors.

1.3   Analytic expressions for blurring kernels

Our first result explicitly characterizes the blurring kernel of point detectors:

Theorem 1. *Let $f \in C_c^\infty(B_R)$, and let $\phi, w : \mathbb{R} \to \mathbb{R}$ be even function such that $\mathbf{x} \in \mathbb{R}^3 \mapsto \phi'(|\mathbf{x}|)/|\mathbf{x}|$ and $\mathbf{z} \in \partial B_R \mapsto w(|\mathbf{z} - \mathbf{z}_0|)$, are absolutely integrable, for some $\mathbf{z}_0 \in \partial B_R$. Moreover, assume that $\mathrm{supp}(\phi) \subset [-\tau, \tau]$, where $\tau := \mathrm{dist}\big(\mathrm{supp}(f), \partial B_R\big)$ and $\mathrm{supp}(\phi) := \overline{\{t : \phi(t) \neq 0\}}$.*

Then $\mathbf{P}_{\phi,w} f \in \mathrm{ran}(\mathbf{P})$ and

$$\left(\mathbf{P}^{-1} \mathbf{P}_{\phi,w} f\right)(\mathbf{x}) = \left[\Phi_{\mathrm{band}} * \int_{\mathbb{R}^3} W_{\mathrm{point}}(\cdot, \mathbf{x}') f(\mathbf{x}') d\mathbf{x}'\right](\mathbf{x}), \qquad \mathbf{x} \in B_R, \tag{2}$$

with the blurring kernels

$$\Phi_{\mathrm{band}}(\mathbf{x}) := -\pi\phi'(|\mathbf{x}|)/(2|\mathbf{x}|), \qquad\qquad \mathbf{x} \in \mathbb{R}^3, \tag{3}$$

$$W_{\mathrm{point}}(\mathbf{x}, \mathbf{x}') := \frac{R^2}{|\mathbf{x}|^2} \delta\left(|\mathbf{x}| - |\mathbf{x}'|\right) w\left(|\mathbf{x} - \mathbf{x}'| R/|\mathbf{x}|\right), \qquad\qquad \mathbf{x}, \mathbf{x}' \in \mathbb{R}^3. \tag{4}$$

Proof. See Section 2. □

As a consequence of Theorem 1, the detector aperture causes blurring in the lateral direction, which becomes more severe near to the recording surface. The finite bandwidth, on the other hand, causes spatially invariant blurring.

We will also prove a corresponding result for approximate line detectors:

Theorem 2. *Let $f \in C_c^\infty(B_R)$, and let $\phi, w : \mathbb{R} \to \mathbb{R}$ be even functions such that $\mathbf{x} \in \mathbb{R}^3 \mapsto \phi'(|\mathbf{x}|)/|\mathbf{x}|$ and $\mathbf{x} \in \mathbb{R}^3 \mapsto \int_{|\mathbf{x}|}^\infty \partial_\xi w(\xi)/\sqrt{\xi^2 - |\mathbf{x}|^2} \, d\xi$ are absolutely integrable. Moreover, assume that $\mathrm{supp}(\phi * w) \subset [-\tau, \tau]$, where $\tau := \mathrm{dist}\big(\mathrm{supp}(f), \partial B_R\big)$.*

Then $\mathbf{L}_{\phi,w} f \in \mathrm{ran}(\mathbf{L})$ *and*

$$\left(\mathbf{L}^{-1} \mathbf{L}_{\phi,w} f\right)(\mathbf{x}) = (\Phi_{\text{band}} * W_{\text{line}} * f)(\mathbf{x}), \qquad \mathbf{x} \in B_R, \tag{5}$$

where Φ_{band} *is as in (3), and*

$$W_{\text{line}}(\mathbf{x}) := -\frac{1}{\pi} \int_{|\mathbf{x}|}^{\infty} \frac{\partial_\xi w(\xi)}{\sqrt{\xi^2 - |\mathbf{x}|^2}} d\xi, \qquad \mathbf{x} \in \mathbb{R}^3. \tag{6}$$

Here both blurring effects are spatially invariant.

Proof. See Section 3. □

1.4 Prior work and innovations

Analytic expressions for the blurring kernels with approximate line detectors are presented for the first time. Exact blurring kernels for approximate point detectors have also been derived in [24]. However, we present a completely different and probably simpler analysis, which is based on geometric arguments and the rotational invariance of the wave equation. Moreover, in [24] the authors did not show that $\mathbf{P}_{\phi,w} f \in \mathrm{ran}(\mathbf{P})$. Instead, they applied a particular inversion formula (i.e. an extension of $\mathbf{P}_{\text{point}}^{-1}$ outside the range of $\mathbf{P}_{\text{point}}$) to the blurred data. Hence their results depend on the used extension, whereas our results are independent of any particular inversion formula. On the other hand, the results of [24] can be applied even if ϕ is non-symmetric, in which case $\phi *_t (\mathbf{P}_{\text{point}} f) \notin \mathrm{ran}(\mathbf{P})$.

2 Blurring kernels for approximate point detectors

The main goal in this section is the derivation analytic expressions for the blurring kernels due to the detector size and bandwidth. The proof of of Theorem 1 will follow from the following Propositions 2.1 and 2.2 and will be given at the end of this section.

Proposition 2.1. *Let* $f \in C_c^\infty(B_R)$*, let* $w : \mathbb{R} \to \mathbb{R}$ *be an even function such that* $\mathbf{z} \in \partial B_R \mapsto w(|\mathbf{z} - \mathbf{z}_0|)$ *is absolutely integrable for some* $\mathbf{z}_0 \in \partial B_R$*, and define*

$$f_w(\mathbf{x}) := \int_{\mathbb{R}^3} \left[\frac{R^2}{|\mathbf{x}|^2} \delta(|\mathbf{x}| - |\mathbf{x}'|) w(|\mathbf{x} - \mathbf{x}'| R / |\mathbf{x}|) \right] f(\mathbf{x}') \, d\mathbf{x}, \qquad \mathbf{x} \in B_R.$$

Then

$$(\mathbf{P} f_w)(\mathbf{z},t) := \int_{S_R} w(|\mathbf{z} - \mathbf{z}'|)(\mathbf{P} f)(\mathbf{z}',t) dS(\mathbf{z}'), \qquad (\mathbf{z},t) \in S_R \times (0,\infty). \tag{7}$$

Proof. Our first goal is to calculate an expression for f_w without the Dirac δ function. To that end, denote $\mathbf{x} = \rho \sigma$, $\mathbf{x}' = \rho' \sigma'$ with $\rho, \rho' \in (0,\infty)$ and $\sigma, \sigma' \in S^2$. Then

$$f_w(\mathbf{x}) = R^2 \int_{S^2} \left(\int_0^\infty \delta(\rho - \rho') w(|\rho\sigma - \rho'\sigma'| R / \rho) f(\rho'\sigma') \, d\rho' \right) d\sigma'$$

$$= R^2 \int_{S^2} w(|\sigma - \sigma'| R) f(\rho\sigma') \, d\sigma'.$$

Now define

$$p_w(\rho\sigma,t) := R^2 \int_{S^2} w(|\sigma - \sigma'| R)(\mathscr{W}^{3D} f)(\rho\sigma',t) \, d\sigma'.$$

We will show that $p_w = \mathscr{W}^{3D} f_w$, which then implies (7), since

$$\int_{S_R} w(|R\sigma - \mathbf{z}'|) p(\mathbf{z}',t) dS(\mathbf{z}') = R^2 \int_{S^2} w(R|\sigma - \sigma'|) p(R\sigma',t) d\sigma' = (\mathbf{P} f_w)(R\sigma,t), \qquad (R\sigma,t) \in S_R \times (0,\infty).$$

To that end, let $Q[\theta,\phi] : \mathbb{R}^3 \to \mathbb{R}^3$ be a rotation with

$$Q[\theta,\phi]\mathbf{e}_3 = (\sin\theta\cos\phi, \sin\theta\sin\phi, \cos\theta), \qquad (\theta,\phi) \in (0,\pi) \times (0,2\pi).$$

Introducing spherical coordinates around axis σ shows that

$$p_w(\rho\sigma,t) = R^2 \int_0^\pi \int_0^{2\pi} w(|\sigma - Q[\theta,\phi]\sigma| R)(\mathscr{W}^{3D} f)(\rho Q[\theta,\phi]\sigma,t) \sin\theta \, d\theta \, d\phi$$

$$= R^2 \int_0^\pi w(2R(1 - \cos\theta)) \sin\theta \int_0^{2\pi} (\mathscr{W}^{3D} f)(Q[\theta,\phi](\rho\sigma),t) \, d\theta \, d\phi.$$

The rotational invariance of the wave equation implies that $(\rho\sigma,t) \mapsto (\mathscr{W}^{3D}f)\big(Q[\theta,\phi](\rho\sigma),t\big)$ is a solution of the wave equation and its linearity implies that so is $p_w(\rho\sigma,t)$. Since the initial conditions $p_w(\mathbf{x},0) = f_w(\mathbf{x})$ and $\partial_t p_w(\mathbf{x},0) = 0$ immediately follow from the definition of p_w this implies $p_w = \mathscr{W}^{3D}f_w$ and concludes the proof. $\qquad\square$

The next proposition deals with the blurring to the finite bandwidth of the detection system.

Proposition 2.2. *Let $f \in C_c^\infty(\mathbb{R}^3)$ and let $\phi : \mathbb{R} \to \mathbb{R}$ be an even compactly supported function such that $\Phi_{\text{band}}(\mathbf{x}) := -\pi\phi'(|\mathbf{x}|)/(2\,|\mathbf{x}|)$ is absolutely integrable. Then $\mathscr{W}^{3D}(\Phi_{\text{band}} * f)(\mathbf{x},t) = (\phi *_t \mathscr{W}^{3D}f)(\mathbf{x},t)$, for $\mathbf{x}$ outside the support of $\Phi_{\text{band}} * f$.*

Proof. Let $\Psi(\mathbf{x}) = \psi(|x|)$ be a radially symmetric absolutely integrable function. Our aim is to find an analytic expression for $\mathscr{W}^{3D}(\Psi * f)$ in terms of the solution $\mathscr{W}^{3D}f$ of (1a), (1b) and the to adjust Ψ such that $\mathscr{W}^{3D}(\Psi * f) = \phi *_t \mathscr{W}^{3D}f$ outside the support of $\Psi * f$.

D' Alemberts formula for the solution of the three dimensional wave equation (see [13]) applied to initial data $\Psi * f$ reads

$$\mathscr{W}^{3D}(\Psi * f)(\mathbf{x},t) = \frac{1}{4\pi}\partial_t t \int_{S^2} \left(\int_{\mathbb{R}^3} f(\mathbf{x}')\psi(|\mathbf{x}+t\omega-\mathbf{x}'|)d\mathbf{x}' \right) dS(\omega).$$

Substituting $\mathbf{x}' = \mathbf{x} + \rho\sigma$, with $\rho > 0$ and $\sigma \in S^2$, in the inner integral, and applying Fubini's Theorem leads to

$$\mathscr{W}^{3D}(\Psi * f)(\mathbf{x},t) = \frac{1}{4\pi}\partial_t t \int_{S^2} \left(\int_{S^2} \int_0^\infty f(\mathbf{x}+\rho\sigma)\psi(|\rho\sigma-t\omega|)\rho^2 d\rho dS(\sigma) \right) dS(\omega)$$

$$= \partial_t t \int_0^\infty \int_{S^2} f(\mathbf{x}+\rho\sigma) \left(\frac{1}{4\pi} \int_{S^2} \psi(|\rho\sigma-t\omega|)dS(\omega) \right) \rho^2 d\rho dS(\sigma)$$

The inner integral in the last expression is the (spherical) mean of $\Psi(\mathbf{x}) = \psi(|x|)$ over a sphere with radius t centered at $\rho\sigma$. Denoting by I_ψ a primitive of $s \mapsto \psi(\sqrt{s})$, then [12, Lemma 5.1] assures that

$$\frac{1}{4\pi} \int_{S^2} \psi(|\rho\sigma-t\omega|)dS(\omega) = \frac{I_\psi\big((\rho+t)^2\big) - I_\psi\big((\rho-t)^2\big)}{4t\rho},$$

provided $\rho, t > 0$. Consequently

$$\mathscr{W}^{3D}(\Psi * f)(\mathbf{x},t) = \frac{1}{4}\partial_t \int_0^\infty \big(I_\psi((\rho+t)^2) - I_\psi((\rho-t)^2)\big)\rho \int_{S^2} f(\mathbf{x}+\rho\sigma)dS(\sigma)\, d\rho.$$

Differentiating under the integral leads

$$\mathscr{W}^{3D}(\Psi * f)(\mathbf{x},t) = \frac{1}{2} \int_0^\infty (\rho-t)\psi(|\rho-t|) \left(\rho \int_{S^2} f(\mathbf{x}+\rho\sigma)dS(\sigma) \right) d\rho, \qquad \mathbf{x} \notin \text{supp}(\Psi * f). \qquad (8)$$

On the other hand, again by D' Alemberts formula, we have

$$(\phi *_t \mathscr{W}^{3D}f)(\mathbf{x},t) = \frac{1}{4\pi} \int_0^\infty \phi'(t-\rho) \left(\rho \int_{S^2} f(\mathbf{x}+\rho\sigma)dS(\sigma) \right) d\rho. \qquad (9)$$

Equations (8) and (9) coincide if $s\psi(|s|) = -\frac{\pi}{2}\phi'(s)$ for all $s \in \mathbb{R}$. Since ϕ is assumed to be an even function, this is the case if

$$\psi(s) = -\frac{\pi}{2}\frac{\phi'(s)}{s}, \qquad s \geq 0.$$

This concludes the proof by taking $\Psi = \Phi_{\text{line}}$. $\qquad\square$

Proof of Theorem 1. *Propositions 2.1 and 2.2 imply that*

$$(\mathbf{P}_{\phi,w}f)(\mathbf{x},t) = \left(\phi *_t \int_{S_R} w(|\mathbf{z}-\mathbf{z}'|)(\mathscr{W}^{3D}f)(\mathbf{z}',\cdot)dS(\mathbf{z}') \right)(t)$$

$$= \big(\phi *_t (\mathscr{W}^{3D}f_w)(\mathbf{x},\cdot)\big)(t) = \big(\mathscr{W}^{3D}(\Phi_{\text{band}} * f_w)(\mathbf{x},t\big), \qquad \mathbf{x} \notin \text{supp}(\Phi_{\text{band}} * f).$$

Together with support hypothesis on ϕ this shows that $\mathbf{P}_{\phi,w}f = \mathbf{P}(\Phi_{\text{band}} * f_w)$. Therefore $\mathbf{P}_{\phi,w}f \in \text{ran}(\mathbf{P})$ and $\mathbf{P}^{-1}\mathbf{P}_{\phi,w}f = \Phi_{\text{band}} * f_w$ which concludes the proof.

3   Blurring kernels for approximate line detectors

The main goal in this section is the proof analytic expressions for the blurring kernels due to the detector size and bandwidth of Theorem 2. In the following let $\mathscr{W}^{2D} : C_c^\infty(\mathbb{R}^2) \to C_c^\infty(\mathbb{R}^2 \times (0,\infty))$ denote the operator that takes a compactly supported initial data to the solution of the two dimensional wave equation

$$\left(\partial_t^2 - \Delta\right) p(\mathbf{x},t) = 0, \qquad\qquad\qquad (\mathbf{x},t) \in \mathbb{R}^2 \times (0,\infty), \qquad (10a)$$

$$p(\mathbf{x},0) = f(\mathbf{x}), \partial_t p(\mathbf{x},0) = 0, \qquad\qquad\qquad \mathbf{x} \in \mathbb{R}^2. \qquad (10b)$$

First we calculate the blurring kernel due to the detector size. To that end, we will make use of the following Lemma:

Lemma 3.1 (Acoustic reciprocal principle in two dimensions)**.** *Let $f \in C_c^\infty(\mathbb{R}^2)$ and let Ψ be a compactly supported absolutely integrable function. Then $\Psi * (\mathscr{W}^{2D} f) = \mathscr{W}^{2D}(\Psi * f)$.*

Proof. D'Alemberts formula for the solution of (10a), (10b) is $(\mathscr{W}^{2D} f)(\mathbf{x},t) = \partial_t (g * f)(\mathbf{x},t)$ with

$$g(\mathbf{x},t) := \begin{cases} 1/\left(2\pi\sqrt{t^2 - |\mathbf{x}|^2}\right), & \text{if } t > |\mathbf{x}|, \\ 0, & \text{otherwise}, \end{cases}$$

see [13]. The symmetry of the convolution implies that

$$\Psi * (\mathscr{W}^{2D} f) = \Psi * \partial_t(g * f) = \partial_t(\Psi * g * f) = g * \partial_t(\Psi * f) = \mathscr{W}^{2D}(\Psi * f),$$

and concludes the proof. $\qquad\qquad\qquad\qquad\qquad\qquad\qquad\qquad\qquad\qquad\qquad\qquad\qquad\square$

Proposition 3.2. *Let $f \in C_c^\infty(\mathbb{R}^3)$, let $w : \mathbb{R} \to \mathbb{R}$ be a compactly supported even function such that $W_{\text{line}}(\mathbf{x}) = -1/\pi \int_{|\mathbf{x}|}^\infty \partial_\xi w(\xi)/\sqrt{\xi^2 - |\mathbf{x}|^2}\, d\xi$ is absolutely integrable.*

Then, for any line $\ell \subset \mathbb{R}^3$,

$$\int_{\mathbb{R}^3} w\big(\text{dist}(\ell,\mathbf{x})\big)(\mathscr{W}^{3D} f)(\mathbf{x},t)d\mathbf{x} = \int_\ell \mathscr{W}^{3D}(W_{\text{line}} * f)(\mathbf{x},t)dS(\mathbf{x}). \qquad (11)$$

Proof. Without loss of restriction we shall assume that ℓ is of the form $\ell = \mathbb{R}(1,0,0) + (0,z_1,z_2)$. Moreover we write $\mathbf{x} = (x_1, \mathbf{x}_2)$ with $x_1 \in \mathbb{R}$ and $\mathbf{x}_2$ in $\mathbb{R}^2$ and denote by $\mathbf{X}$ the X-ray transform restricted to lines pointing in $(1,0,0)$ direction,

$$(\mathbf{X}h)(\mathbf{x}_2) := \int_\mathbb{R} h(x_1, \mathbf{x}_2)dx_1, \qquad h \in C_c^\infty(\mathbb{R}^3).$$

The commutation relation of the Laplacian with the X-ray transform implies that $\mathscr{W}^{2D}\mathbf{X} = \mathbf{X}\mathscr{W}^{3D}$, see [10, Theorem 1]. Therefore

$$\int_{\mathbb{R}^3} w(\text{dist}(\ell,\mathbf{x}))(\mathscr{W}^{3D} f)(\mathbf{x},t)d\mathbf{x} = \int_{\mathbb{R}^2} \int_\mathbb{R} w(|\mathbf{z}_2 - \mathbf{x}_2|)(\mathscr{W}^{3D} f)((x_1,\mathbf{x}_2),t)dx_1 d\mathbf{x}_2$$

$$= \int_{\mathbb{R}^2} w(|\mathbf{z}_2 - \mathbf{x}_2|)(\mathbf{X}\mathscr{W}^{3D} f)(\mathbf{x}_2,t)d\mathbf{x}_2$$

$$= \big(w(|\cdot|) * (\mathbf{X}\mathscr{W}^{3D} f)\big)(\mathbf{z}_2,t) = \big(w(|\cdot|) * (\mathscr{W}^{2D}\mathbf{X} f)\big)(\mathbf{z}_2,t). \qquad (12)$$

Let $U(\mathbf{x}) = u(|\mathbf{x}|)$ be a radially symmetric integrable function. Writing $\mathbf{x}' = (x_1', \mathbf{x}_2')$ with $x_1' \in \mathbb{R}$ and $\mathbf{x}_2'$ in $\mathbb{R}^2$, and applying Fubini's theorem shows

$$\mathbf{X}(U * f)(\mathbf{z},t) = \int_\ell (U * f)(\mathbf{x},t)dS(\mathbf{x})$$

$$= \int_\mathbb{R} \left(\int_\mathbb{R}\int_{\mathbb{R}^2} u\big(((x_1 - \mathbf{x}_1)^2 + |\mathbf{x}_2 - \mathbf{x}_2'|^2)^{1/2}\big)f(x_1',\mathbf{x}_2')d\mathbf{x}_2'dx_1'\right)dx_1$$

$$= \int_\mathbb{R}\int_{\mathbb{R}^2} \left(\int_\mathbb{R} u\big(((x_1 - \mathbf{x}_1)^2 + |\mathbf{x}_2 - \mathbf{x}_2'|^2)^{1/2}\big)dx_1\right)f(x_1',\mathbf{x}_2')d\mathbf{x}_2'dx_1'$$

$$= \int_\mathbb{R}\int_{\mathbb{R}^2} \left(\int_\mathbb{R} u\big((s^2 + |\mathbf{x}_2 - \mathbf{x}_2'|^2)^{1/2}\big)ds\right)f(x_1',\mathbf{x}_2')d\mathbf{x}_2'dx_1'$$

$$= \int_{\mathbb{R}^2} \left(\int_\mathbb{R} u\big((s^2 + |\mathbf{x}_2 - \mathbf{x}_2'|^2)^{1/2}\big)ds\right)(\mathbf{X}f)(\mathbf{x}_2')d\mathbf{x}_2'$$

$$= \int_{\mathbb{R}^2} I_u(|\mathbf{x}_2 - \mathbf{x}_2'|)(\mathbf{X}f)(\mathbf{x}_2')d\mathbf{x}_2' =: \big(I_u(|\cdot|) * \mathbf{X}f\big)(\mathbf{x}_2), \qquad (13)$$

where we defined $I_u(\xi) := \int_{\mathbb{R}} u\big((s^2+\xi^2)^{1/2}\big)ds$.

The relation $\mathbf{X}\mathscr{W}^{3D} = \mathscr{W}^{2D}\mathbf{X}$, identity (13), and the acoustic reciprocal principle Lemma 3.1, imply

$$\int_\ell \mathscr{W}^{3D}(U*f)(\mathbf{x},t)dS(\mathbf{x}) = \big((\mathbf{X}\mathscr{W}^{3D}(U*f))(\mathbf{z},t) = \big(\mathscr{W}^{2D}\mathbf{X}(U*f)\big)(\mathbf{z},t)$$
$$= \big(\mathscr{W}^{2D}(I_u(|\cdot|)*\mathbf{X}f)\big)(\mathbf{z},t) = \big(I_u(|\cdot|)*(\mathscr{W}^{2D}\mathbf{X}f)\big)(\mathbf{z},t). \tag{14}$$

Consequently the left hand sides of (12) and (14) coincide, if

$$w(\xi) = I_u(\xi) = \int_{\mathbb{R}} u\big((s^2+\xi^2)^{1/2}\big)ds = 2\int_\xi^\infty u(\eta)\frac{\eta\, d\eta}{\sqrt{\eta^2-\xi^2}}\,.$$

This is an Abel integral equation for the function W. Its solution is (see [8, 20])

$$u(\eta) = -\frac{1}{\pi}\int_\eta^\infty \frac{\partial_\xi w(\xi)}{\sqrt{\xi^2-\eta^2}}d\xi\,.$$

This concludes the proof by taking $U = W_{\text{line}}$. $\qquad\square$

Next we calculate the point spread function due to finite bandwidth.

Proposition 3.3. *Let $f \in C_c^\infty(\mathbb{R}^3)$ and let $\phi: \mathbb{R} \to \mathbb{R}$ be an even compactly supported function such that $\Phi_{\text{band}}(\mathbf{x}) := -\pi\phi'(|\mathbf{x}|)/(2|\mathbf{x}|)$ is absolutely integrable. Then*

$$\phi *_t \int_\ell (\mathscr{W}^{3D}f)(\mathbf{x},t)d\mathbf{x} = \int_\ell (\mathscr{W}^{3D}\Phi_{\text{band}}*f)(\mathbf{x},t)d\mathbf{x} \tag{15}$$

for any line ℓ outside the support of $\Phi_{\text{band}}*f$.

Proof. Proposition 2.2 states that $\phi *_t (\mathscr{W}^{3D}f) = \mathscr{W}^{3D}(\Phi_{\text{band}}*f)$ outside the support of of $\Phi_{\text{band}}*f$. Integrating this identity over ℓ proves (15). $\qquad\square$

Proof of Theorem 2. *According to Propositions 3.2 and 3.3*

$$\phi *_t \int_{\mathbb{R}^3} w\big(\text{dist}(\ell,\mathbf{x})\big)(\mathscr{W}^{3D}f)(\mathbf{x},t)d\mathbf{x} = \phi *_t \int_\ell \mathscr{W}^{3D}(W_{\text{line}}*f)(\mathbf{x},t)d\mathbf{x} = \int_\ell \mathscr{W}^{3D}(\phi *_t W_{\text{line}}*f)(\mathbf{x},t)d\mathbf{x}.$$

By taking $\ell = \ell_{\mathbf{z}}$, $\mathbf{z} \in B_R$, and using the support hypothesis on $\phi * w$, this shows $\mathbf{L}_{\phi,w}f = \mathbf{L}(\Phi_{\text{band}}*W_{\text{line}}*f)$. Therefore $\mathbf{L}_{\phi,w}f \in \text{ran}(\mathbf{L})$ and $\mathbf{L}^{-1}\mathbf{L}_{\phi,w}f = \Phi_{\text{band}}*W_{\text{line}}*f$ which concludes the proof.

4   Discussion and Conclusion

In this note we derived analytic expression for the point spread functions in PAT due to the finite detector size and the finite bandwidth of the ultrasound detection system. We showed that the point spread functions due to the finite bandwidth is spatial invariant. The point spread functions due to the detector size is only spatial invariant in the case of approximate line detectors.

The full with half maximum of the point spread function is a typical parameter to measure spatial resolution. Ignoring effects of finite bandwidth, Theorems 1 and 2 show that the lateral resolution of PAT with "approximate point detectors" is $a_{\text{transducer}}|\mathbf{x}|/R$, where $a_{\text{transducer}}$ is the diameter of the ultrasound transducer, and the (uniform) resolution of PAT with "approximate line detectors" is approximately a_{laser}, the width of the detecting laser beam (See Figure 4). Typical values $a_{\text{transducer}} = 2$ cm and $a_{\text{laser}} = 0.1$ cm point out the improved spatial resolution of PAT with integrating line detectors.
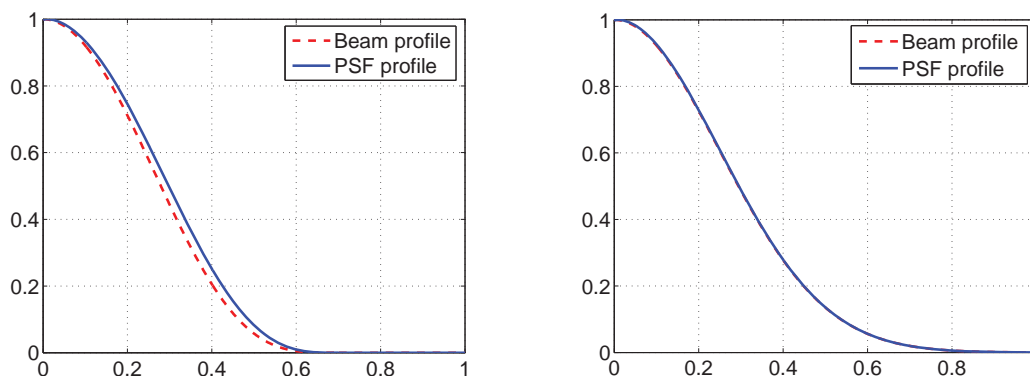
5   Acknowledgement

Figure 4: Examples for a beam profile $w(r)$ and profile $-1/\pi \int_r^\infty (\partial_s w)/\sqrt{s^2 - r^2}\,ds$ of the corresponding point spread function $W_{\text{line}}(\mathbf{x})$. One recognizes that the full with half maximum of both functions are similar.

6 References

[1] M. L. Agranovsky and E. T. Quinto. Injectivity sets for the Radon transform over circles and complete systems of radial functions. *J. Funct. Anal.*, 139(2):383–414, 1996.

[2] G. Ambartsoumian and P. Kuchment. On the injectivity of the circular Radon transform. *Inverse Probl.*, 21(2):473–485, 2005.

[3] P. Burgholzer, C. Hofer, G. Paltauf, M. Haltmeier, and O. Scherzer. Thermoacoustic tomography with integrating area and line detectors. *IEEE Trans. Ultrason., Ferroeletr., Freq. Control*, 52(9):1577–1583, 2005.

[4] R. O. Esenaliev, I. V. Larina, K. V. Larin, D. J. Deyo, M. Motamedi, and D. S. Prough. Optoacoustic technique for noninvasive monitoring of blood oxygenation: a feasibility study. *App. Opt.*, 41(22):4722–4731, 2002.

[5] D. Finch, M. Haltmeier, and Rakesh. Inversion of spherical means and the wave equation in even dimensions. *SIAM J. Appl. Math.*, 68(2):392–412, 2007.

[6] D. Finch, S. Patch, and Rakesh. Determining a function from its mean values over a family of spheres. *SIAM J. Math. Anal.*, 35(5):1213–1240, 2004.

[7] D. Finch and Rakesh. Trace identities for solutions of the wave equation with initial data supported in a ball. *Math. Methods Appl. Sci.*, 28:1897–1917, 2005.

[8] R. Gorenflo and S. Vessella. *Abel integral equations*, volume 1461 of *Lecture Notes in Mathematics*. Springer-Verlag, Berlin, 1991. Analysis and applications.

[9] H. Grün, M. Haltmeier, G. Paltauf, and P. Burgholzer. Photoacoustic tomography using a fiber based Fabry–Perot interferometer as an integrating line detector and image reconstruction by model-based time reversal method - article no. 663107. In C. Depeursinge, editor, *Novel Optical Instrumentation for Biomedical Applications III*, volume 6631. SPIE, 2007.

[10] M. Haltmeier and T. Fidler. Mathematical challenges arising in thermoacoustic tomography with line detectors. *arXiv:math/0610155v4*, 2008.

[11] M. Haltmeier, O. Scherzer, P. Burgholzer, R. Nuster, and G. Paltauf. Thermoacoustic tomography & the circular Radon transform: Exact inversion formula. *Math. Models Methods Appl. Sci.*, 17(4):635–655, 2007.

[12] M. Haltmeier, T. Schuster, and O. Scherzer. Filtered backprojection for thermoacoustic computed tomography in spherical geometry. *Math. Methods Appl. Sci.*, 28(16):1919–1937, 2005.

[13] F. John. *Partial Differential Equations*, volume 1 of *Applied Mathematical Sciences*. Springer Verlag, New York, fourth edition, 1982.

[14] R. G. M. Kolkman, E. Hondebrink, W. Steenbergen, and F. F. M. De Mul. In vivo photoacoustic imaging of blood vessels using an extreme-narrow aperture sensor. *IEEE J. Sel. Topics Quantum Electron.*, 9(2):343–346, 2003.

[15] R. A. Kruger, W. L. Kiser, D. R. Reinecke, G. A. Kruger, and K. D. Miller. Thermoacoustic molecular imaging of small animals. *Mol. Imaging*, 2(2):113–123, 2003.

[16] R. A. Kruger, K. D. Miller, H. E. Reynolds, W. L. Kiser, D. R. Reinecke, and G. A. Kruger. Breast cancer in vivo: contrast enhancement with thermoacoustic CT at 434 MHz-feasibility study. *Radiology*, 216(1):279–283, 2000.

[17] L. A. Kunyansky. Explicit inversion formulae for the spherical mean Radon transform. *Inverse Probl.*, 23(1):373–383, 2007.

[18] L. A. Kunyansky. A series solution and a fast algorithm for the inversion of the spherical mean radon transform. *Inverse Probl.*, 23(6):S11–S20, 2007.

[19] S. Manohar, A. Kharine, J. C. G. van Hespen, W. Steenbergen, and T. G. van Leeuwen. The twente photoa-

coustic mammoscope: system overview and performance. *Physics in Medicine and Biology*, 50(11):2543–2557, 2005.

[20] F. Natterer. *The Mathematics of Computerized Tomography*, volume 32 of *Classics in Applied Mathematics*. SIAM, Philadelphia, 2001.

[21] G. Paltauf, R. Nuster, M. Haltmeier, and P. Burgholzer. Experimental evaluation of reconstruction algorithms for limited view photoacoustic tomography with line detectors. *Inverse Probl.*, 23(6):81–94, 2007.

[22] O. Scherzer, M. Grasmair, H. Grossauer, M. Haltmeier, and F. Lenzen. *Variational Methods in Imaging*, volume 167 of *Applied Mathematical Sciences*. Springer, New York, 2008.

[23] X. D. Wang, G. Pang, Y. J. Ku, X. Y. Xie, G. Stoica, and L. V. Wang. Noninvasive laser-induced photoacoustic tomography for structural and functional *in vivo* imaging of the brain. *Nature Biotech.*, 21(7):803–806, 2003.

[24] M. Xu and L. V. Wang. Analytic explanation of spatial resolution related to bandwidth and detector aperture size in thermoacoustic or photoacoustic reconstruction. *Phys. Rev. E*, 67(5):0566051–05660515 (electronic), 2003.

[25] M. Xu and L. V. Wang. Universal back-projection algorithm for photoacoustic computed tomography. *Phys. Rev. E*, 71(1):0167061–0167067 (electronic), 2005.

A Reconstruction Algorithm for Photoacoustic Imaging Based on the Nonuniform FFT

Markus Haltmeier*, Otmar Scherzer, *Associate Member, IEEE*, and Gerhard Zangerl

Abstract—**Fourier reconstruction algorithms significantly outperform conventional backprojection algorithms in terms of computation time. In photoacoustic imaging, these methods require interpolation in the Fourier space domain, which creates artifacts in reconstructed images. We propose a novel reconstruction algorithm that applies the one-dimensional nonuniform fast Fourier transform to photoacoustic imaging. It is shown theoretically and numerically that our algorithm avoids artifacts while preserving the computational effectiveness of Fourier reconstruction.**

Index Terms—**Fast Fourier algorithm, image reconstruction, nonuniform FFT, photoacoustic imaging, planar measurement geometry.**

I. INTRODUCTION

PHOTOACOUSTIC imaging (PAI) is a novel promising tool for visualizing light absorbing structures in an optically scattering medium, which carry valuable information for medical diagnostics. It is based on the generation of acoustic waves by illuminating an object with pulses of nonionizing electromagnetic radiation, and combines the high contrast of pure optical and the high resolution of ultrasonic imaging. The method has demonstrated great promise for a variety of biomedical applications, such as imaging of animals [1], [2], early cancer diagnostics [3], [4], and imaging of vasculature [5], [6].

When an object is illuminated with short pulses of nonionizing electromagnetic radiation, it absorbs a fraction of energy and heats up. This in turn induces acoustic (pressure) waves, that are recorded with acoustic detectors outside of the object. Other than in conventional ultrasound imaging, where the source of acoustic waves is an external transducer, in PAI the source is the imaged object itself. The frequency bandwidth of the recorded signals is therefore generally broad and depends on the size and the shape of illuminated structures.
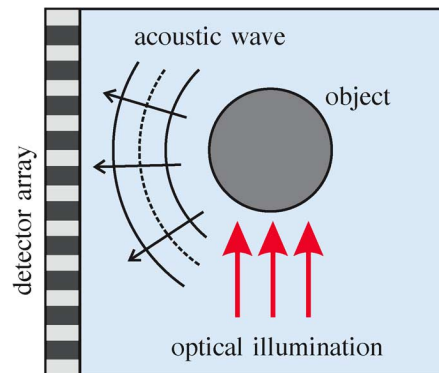
Fig. 1. Photoacoustic imaging for planar recording geometry. The object is illuminated by a pulse of electromagnetic radiation, and reacts with an expansion. Induced acoustic waves are measured with an array of acoustic detectors arranged on a plane (or a line) and used to from an image of the object.

A. Planar Recording Geometry

Throughout this paper, we assume a planar recording geometry, where the acoustic signals are recorded with omnidirectional detectors arranged on planes (or lines); see Fig. 1. The planar geometry is of particular interest since it can be realized most easily in practical applications. The recorded acoustic signals are then used to reconstruct the initially generated acoustic pressure which represents optically absorbing structures of the investigated object.

For the planar recording geometry, two types of theoretically exact reconstruction formulas have been reported: Temporal backprojection [7]–[10] and Fourier domain formulas [11], [7], [9], [12]–[15]. Numerical implementations of those formulas often lead to fast and accurate image reconstruction algorithms.

In temporal backprojection formulas, the signals measured at time t are back projected over spheres of radius $v_s t$ with the detector position in the center (v_s denotes the speed of sound). In Fourier domain formulas this backprojection is performed by interpolation in the frequency domain. Reconstruction methods based on Fourier domain formulas are attractive since they reconstruct an $N \times N \times N$ image in $\mathcal{O}(N^3 \log N)$ floating point operations by using of the fast Fourier transform (FFT). Straightforward implementations of backprojection type formulas, on the other hand, require $\mathcal{O}(N^5)$ operation counts; see [16] and [17].

The standard FFT algorithm assumes sampling on an equally spaced grid and therefore, in order to implement the Fourier domain formulas, interpolation in the Fourier space is required. Interpolation in the Fourier domain is a critical issue, and creates artifacts in reconstructed images, see the examples in Section V. One obtains significantly better results by increasing

the sampling density in the Fourier space. This is achieved by either zero-padding [13] or by symmetrizing the recorded signals around $t = 0$ (which is equivalent to using the fast cosine transform instead of the FFT). In this paper, we propose an efficient reconstruction algorithm that uses the nonuniform (or unevenly spaced) FFT [18]–[23] and further increases the quality of reconstruction.

B. Prior Work and Innovations

The nonuniform FFT has been applied to a variety of medical imaging problems, such as standard X-ray CT, magnetic resonance imaging, and diffraction tomography [24]–[26], and has also been used implicitly in gridding algorithms [27], [28]. All those algorithms deal with the problem of recovering a two (or higher) dimensional object function from samples of its multidimensional Fourier transform on a non-Cartesian grid.

Our approach is conceptually quite different to the above mentioned references: The special structure of our problem allows to perform several one-dimensional nonuniform FFTs instead of a single higher dimensional one. This leads to a reduced numerical cost, compared to the above algorithms. The proposed algorithm is more closely related to a reconstruction algorithm for X-ray CT suggested in [29, Sec. 5.2], which also evaluates the Fourier transform on irregular samples by means of the one-dimensional FFT.

C. Outline

This paper is organized as follows. In Section II, we present the mathematical basics of Fourier reconstruction in PAI. In Section III, we review the nonuniform FFT which is then used to derive the nonuniform FFT based reconstruction algorithm in Section IV. In Section V, we present numerical results of the proposed algorithm and compare it with existing Fourier and backprojection algorithms. The paper concludes with a discussion of some issues related to sampling and resolution in the Appendix.

II. PHOTOACOUSTIC IMAGING

Let $C_0^\infty(\mathbb{H})$ denote the space of smooth functions with bounded support in the half space $\mathbb{H} := \mathbb{R}^{d-1} \times (0, \infty), d \geq 2$. Consider the initial value problem

$$
\begin{aligned}
\left(\partial_t^2 - \Delta\right) p(\mathbf{x}, t) &= 0, \quad (\mathbf{x}, t) \in \mathbb{R}^d \times (0, \infty), \\
p(\mathbf{x}, 0) &= f(\mathbf{x}), \quad \mathbf{x} \in \mathbb{R}^d, \\
\partial_t p(\mathbf{x}, 0) &= 0, \quad \mathbf{x} \in \mathbb{R}^d
\end{aligned}
$$

with $f \in C_0^\infty(\mathbb{H})$. Here Δ denotes the Laplacian in $\mathbb{R}^d$ and ∂_t is the derivative with respect to t. We write $\mathbf{x} = (x, y), x \in \mathbb{R}^{d-1}, y \in \mathbb{R}$, and define the operator $\mathbf{Q} : C_0^\infty(\mathbb{H}) \to C^\infty(\mathbb{R}^d)$ by

$$
(\mathbf{Q}f)(x, t) := \begin{cases} p(x, y = 0, t), & \text{if } t > 0, \\ 0, & \text{otherwise.} \end{cases}
$$

Photoacoustic imaging for planar recording geometry is concerned with reconstructing $f \in C_0^\infty(\mathbb{H})$ from incomplete and possibly erroneous knowledge of $\mathbf{Q}f$. Of practical interest are the cases $d = 2$ and $d = 3$, see [30]–[33].

A. Exact Inversion Formula

The operator $\mathbf{Q}$ can be inverted analytically by means of the exact inversion formula

$$
\begin{aligned}
&(\mathbf{F}f)(K_x, K_y) \\
&= \frac{2K_y(\mathbf{FQ}f)\left(K_x, \text{sign}(K_y)\sqrt{|K_x|^2 + K_y^2}\right)}{\text{sign}(K_y)\sqrt{|K_x|^2 + K_y^2}}
\end{aligned}
\tag{1}
$$

where $(K_x, K_y) \in \mathbb{R}^{d-1} \times \mathbb{R}$, and $\mathbf{F}$ denotes the d-dimensional Fourier transform

$$
(\mathbf{F}\varphi)(\mathbf{K}) := \int_{\mathbb{R}^d} e^{-i\mathbf{K}\mathbf{x}} \varphi(\mathbf{x}) \, d\mathbf{x}, \quad \mathbf{K} = (K_x, K_y) \in \mathbb{R}^d.
$$

Equation (1) has been derived in [12], [13] for three spatial dimensions. It can be proven in any dimension by using the inversion formula for the spherical mean Radon transform of [7], [9]. A related formula using the Fourier cosine transform instead of the Fourier transform has been obtained in [34], [15] for $d = 2, 3$.

B. Partial Fourier Reconstruction

The inversion formula (1) yields an exact reconstruction of f, provided that $(\mathbf{Q}f)(x, t)$ is given for all $(x, t) \in \mathbb{R}^d$. In practical applications, only a *partial* (or *limited view*) data set is available [35]–[37]. In this paper we assume that data $(\mathbf{Q}f)(x, t)$ are given only for $(x, t) \in (0, X)^d$ (see Fig. 1) which are modeled by

$$
g(x, t) := w_{\text{cut}}(x, t)(\mathbf{Q}f)(x, t)
\tag{2}
$$

where w_{cut} is a smooth nonnegative cutoff function that vanishes outside $(0, X)^d$. Using data (2), the function f cannot be exactly reconstructed in a stable way (see [38] and [37]). It is therefore common to apply the exact inverse of $\mathbf{Q}$ to the partial data g and to consider the result as an approximation of the object to be reconstructed. More precisely, the function $f^\dagger$ defined by

$$
\begin{aligned}
&(\mathbf{F}f^\dagger)(K_x, K_y) \\
&:= \frac{2K_y(\mathbf{F}g)\left(K_x, \text{sign}(K_y)\sqrt{|K_x|^2 + K_y^2}\right)}{\text{sign}(K_y)\sqrt{|K_x|^2 + K_y^2}}
\end{aligned}
\tag{3}
$$

is considered an approximation of f. The function $f^\dagger$ is called *partial Fourier reconstruction*.

Fourier reconstruction algorithms in PAI name numerical implementations of (3). In this paper, we apply the one-dimensional nonuniform FFT to derive a fast and accurate algorithm for implementing (3).

III. NONUNIFORM FAST FOURIER TRANSFORM

The discrete Fourier transform of a vector $\mathbf{g} = (g_n)_{n=0}^{N-1} \in \mathbb{C}^N$ with respect to the nodes $\boldsymbol{\omega} = (\omega_k)_{k=-N/2}^{N/2-1}$ (with N even)

is defined by

$$T[\mathbf{g}](\omega_k) := \sum_{n=0}^{N-1} e^{-i\omega_k n 2\pi/N} g_n,$$
$$k = -N/2, \ldots, N/2 - 1. \quad (4)$$

Direct evaluation of the N sums in (4) requires $\mathcal{O}(N^2)$ operations. Using the classical fast Fourier transform (FFT) this effort can be reduced to $\mathcal{O}(N \log N)$ operations. However, application of the classical FFT is restricted to the case of evenly spaced nodes $\omega_k = k$, $k = -N/2, \ldots, N/2 - 1$.

The one-dimensional nonuniform FFT (see [18]–[20], [29], and [21]–[23]) is an approximate but highly accurate method for evaluating (4) at arbitrary nodes ω_k, $k = -N/2, \ldots, N/2 - 1$, in $\mathcal{O}(N \log N)$ operations.

A. Derivation of the Nonuniform FFT

To derive the nonuniform FFT we closely follow the presentation of [29], which is based on the following lemma.

Lemma 1 [29, Prop. 1]: Let $c > 1$ and $\alpha < \pi(2c - 1)$. Assume that $\Psi : \mathbb{R} \to \mathbb{R}$ is continuous in $[-\alpha, \alpha]$, vanishing outside $[-\alpha, \alpha]$, and positive in $[-\pi, \pi]$. Then

$$e^{-i\omega\theta} = \frac{c}{2\pi\Psi(\theta)} \sum_{j\in\mathbb{Z}} \hat{\Psi}(\omega - j/c) e^{-ij\theta/c},$$
$$\omega \in \mathbb{R}, |\theta| \le \pi \quad (5)$$

where $\hat{\Psi}(\omega) := \int_{\mathbb{R}} e^{-i\omega\theta} \Psi(\theta) d\theta$ denotes the one-dimensional Fourier transform of Ψ.

Proposition 2: Let c, α, Ψ, and $\hat{\Psi}$ be as in Lemma 1. Then, for every $\mathbf{g} = (g_n)_{n=0}^{N-1} \in \mathbb{C}^N$ and $\omega \in \mathbb{R}$ we have

$$\sum_{n=0}^{N-1} e^{-i\omega n 2\pi/N} g_n = \sum_{j\in\mathbb{Z}} e^{-i\pi(\omega-j/c)} \hat{\Psi}(\omega - j/c) \hat{G}_j \quad (6)$$

with

$$\hat{G}_j := \frac{c}{2\pi} \left(\sum_{n=0}^{N-1} \frac{g_n e^{-ijn2\pi/(Nc)}}{\Psi(n2\pi/N - \pi)} \right), \qquad j \in \mathbb{Z}. \quad (7)$$

Proof: Taking $\theta = n2\pi/N - \pi \in [-\pi, \pi]$ in (5), gives

$$e^{-i\omega n 2\pi/N} = \frac{c}{2\pi\Psi(n2\pi/N - \pi)}$$
$$\times \sum_{j\in\mathbb{Z}} \hat{\Psi}(\omega - j/c) e^{-ijn2\pi/(cN)} e^{-i\pi(\omega-j/c)}$$

and therefore

$$\sum_{n=0}^{N-1} e^{-i\omega n 2\pi/N} g_n$$
$$= \frac{c}{2\pi} \sum_{n=0}^{N-1} \sum_{j\in\mathbb{Z}} e^{-i\pi(\omega-j/c)} \hat{\Psi}(\omega - j/c)$$
$$\times \frac{g_n e^{-ijn2\pi/(cN)}}{\Psi(n2\pi/N - \pi)}.$$

Interchanging the order of summation in the right-hand side of the above equation shows (6), (7) and concludes the proof. ∎

In the following, we assume that cN is an even number. Then

$$\hat{G}_j = \frac{c}{2\pi} \left(\sum_{n=0}^{cN-1} \frac{g_n}{\Psi(n2\pi/N - \pi)} e^{-ijn2\pi/(Nc)} \right),$$
$$j \in \mathbb{Z} \quad (8)$$

where $g_n := 0$ for $n \ge N$, is an oversampled discrete Fourier transform with the oversampling factor c. Moreover, we assume that $\hat{\Psi}$ is concentrated around zero and decays rapidly away from zero. The nonuniform FFT uses the formulas (6) and (8) to evaluate $T[\mathbf{g}]$ at the nodes ω_k. The basic steps of the algorithm are as follows.

i) Append $(c - 1)N$ zeros to the vector $\mathbf{g} = (g_n)_{n=0}^{N-1}$ and evaluate $\hat{G}_j$, $j = -Nc/2, \ldots, Nc/2 - 1$, in (8) with the FFT algorithm.

ii) Evaluate the sums in (6) approximately by using only the terms with $|\omega_k - j/c| \le K$, where the *interpolation length* K is a small positive parameter.

Since $\hat{\Psi}$ is assumed to decay rapidly, the truncation error in Step ii) is small.

Algorithm 1 Nonuniform FFT with respect to the nodes $\boldsymbol{\omega} = (\omega_k)_{k=-N/2}^{N/2-1}$, using input vector $\mathbf{g} = (g_n)_{n=0}^{N-1}$, oversampling $c > 1$, interpolation length K, and window function Ψ.

---

1) $\boldsymbol{\Psi} \leftarrow (\Psi(2\pi n/N - \pi))_n$ ▷ precomputations
2) $\hat{\boldsymbol{\Psi}} \leftarrow (e^{-i(\omega_k-j/c)\pi/c} \hat{\Psi}(\omega_k - j/c))_{k,j}$
3)
4) **function** nufft $\mathbf{g}, \boldsymbol{\omega}, c, K, \boldsymbol{\Psi}, \hat{\boldsymbol{\Psi}}$
5) $\mathbf{g} \leftarrow \mathbf{g}/\boldsymbol{\Psi} \cdot c/(2\pi)$
6) $\mathbf{g} \leftarrow (\mathbf{g}, \texttt{zeros}(1, (c-1)N)$ ▷ zero-padding
7) $\mathbf{g} \leftarrow \texttt{fft}(\mathbf{g})$ ▷ one-dimensional FFT
8)   **for** $k = -N/2, \ldots, N/2 - 1$ **do**
9) $\hat{g}_k \leftarrow \sum_{|j-c\omega_k| \le cK} \hat{\Psi}_{k,j} g_j$ ▷ interpolation
10)   **end for**
11)   **return** $(\hat{g}_k)_k$
12) **end function**

The nonuniform Fourier transform is summarized in Algorithm 1. All evaluations of Ψ and $\hat{\Psi}$ are precomputed and stored. Moreover, the classical FFT is applied to a vector of length cN. Therefore the numerical complexity of Algorithm 1 is $\mathcal{O}(cN \log N)$. Typically $c = 2$, in which case the numerical effort of the nonuniform FFT is essentially twice the effort of the one-dimensional classical FFT applied to an input vector of the same length. See [29, Sec. 3] for an exact operation count, and a comparison between actual computation times of the classical and the nonuniform FFT.

B. Kaiser Bessel Window

In our implementation we choose for Ψ the *Kaiser Bessel window*

$$\Psi_{\text{KB}}^{\alpha,K}(\theta) := \frac{1}{I_0(\alpha K)} \begin{cases} I_0(K\sqrt{\alpha^2 - \theta^2}), & \text{if } |\theta| \le \alpha, \\ 0, & \text{if } |\theta| > \alpha \end{cases}$$

where I_0 is the modified Bessel function of order zero. The one-dimensional Fourier transform of $\Psi_{\mathrm{KB}}^{\alpha,K}$ is

$$\hat{\Psi}_{\mathrm{KB}}^{\alpha,K}(\omega) = 2\sinh(\alpha\sqrt{K^2 - \omega^2})/(I_0(\alpha K)\sqrt{K^2 - \omega^2})$$

if $\omega \in \mathbb{R} \setminus \{-K, K\}$ and $2\alpha/(I_0(\alpha K))$ otherwise.

The Kaiser Bessel window is a good and often used candidate for Ψ, since $\hat{\Psi}_{\mathrm{KB}}^{\alpha,K}(\omega)$ becomes extremely small for $|\omega| \geq K$. For example, with the parameters $K = 3$, and $\alpha = 3\pi$, we have for $\omega \geq K$

$$\left| \hat{\Psi}_{\mathrm{KB}}^{\alpha,K}(\omega)/\hat{\Psi}_{\mathrm{KB}}^{\alpha,K}(0) \right| \leq \left| \hat{\Psi}_{\mathrm{KB}}^{\alpha,K}(K)/\hat{\Psi}_{\mathrm{KB}}^{\alpha,K}(0) \right|$$
$$\simeq 3*10^{-11}.$$

Remark 3: Take $c = 1$ and let Ψ be the characteristic function of the interval $[-\pi, \pi]$. Then $\hat{\Psi}(\omega) = 2\pi\mathrm{sinc}(\pi\omega)$ and (6), (7) reduce to the sinc series

$$\sum_{n=0}^{N-1} e^{-i\omega n 2\pi/N} g_n$$
$$= \sum_{j\in\mathbb{Z}} e^{-i\pi(\omega-j)}\mathrm{sinc}(\omega - j)\left(\sum_{n=0}^{N-1} g_n e^{-ijn2\pi/N}\right)$$

which is a discretized version of Shannon's sampling formula [39], [40]

$$\hat{g}(\omega) = \sum_{j\in\mathbb{Z}} e^{-i\pi(\omega-j)}\mathrm{sinc}(\omega - j)\hat{g}(j), \quad \omega \in \mathbb{R}$$

applied to the Fourier transform of a function $g : \mathbb{R} \to \mathbb{R}$ that vanishes outside $[0, 2\pi]$.

See Fig. 2 for a comparison of sinc and $\hat{\Psi}_{\mathrm{KB}}^{\alpha,K}$, with $K = 3$ and $\alpha = 3\pi$. One realizes that $\hat{\Psi}_{\mathrm{KB}}^{\alpha,K}$ decays much faster than sinc and is therefore much better suited for truncated interpolation. In fact, $|\hat{\Psi}_{\mathrm{KB}}^{\alpha,K}(\omega)/\hat{\Psi}_{\mathrm{KB}}^{\alpha,K}(0)| < 3*10^{-11}$ for $\omega \geq 3$, whereas $|\mathrm{sinc}(\omega)| < 0.01$ only for $\omega \geq 100/\pi$.

An error estimate for the nonuniform FFT using the Kaiser Bessel window is given in [29]. The result is

$$\left| e^{-i\omega\theta} - \frac{c}{2\pi\Psi(\theta)} \sum_{|\omega-j/c|<K} \hat{\Psi}_{\mathrm{KB}}^{\alpha,K}(\omega - j/c)e^{-ij\theta/c} \right|$$
$$\leq \frac{30}{\pi I_0(K\pi\sqrt{\alpha^2 - 1/c^2})}.$$

For example, taking $c = 2$, $\alpha = 3\pi$ and $K = 3$, the above error is as small as $3*10^{-8}$.

IV. FOURIER RECONSTRUCTION ALGORITHM BASED ON THE NONUNIFORM FFT

In this section, we apply the one-dimensional nonuniform FFT to photoacoustic imaging. Throughout the following we restrict our attention to two dimensions, noting that the general case $d \geq 2$ can be treated in an analogous manner.

Assume that f is a smooth function that vanishes outside $(0, X)^2$, and set $g := w_{\mathrm{cut}}\mathbf{Q}f$, where w_{cut} is as in (2). Fourier reconstruction names an implementation of (3), that uses discrete data

$$g_{m,n} := g(m\Delta_{\mathrm{samp}}, n\Delta_{\mathrm{samp}}) \tag{9}$$
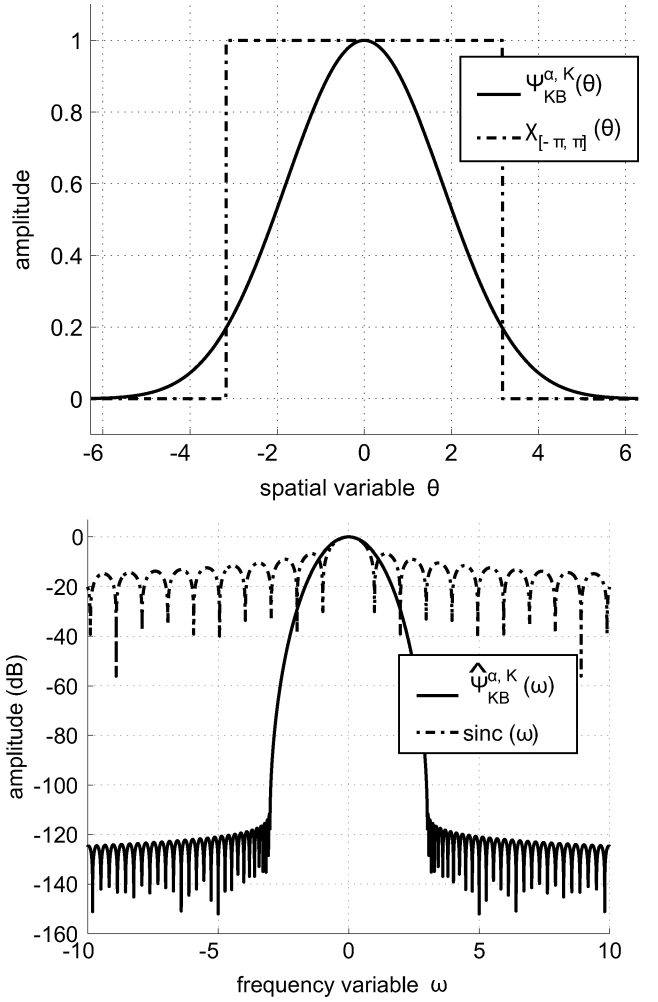

Fig. 2. Top: Kaiser-Bessel window $\Psi_{\mathrm{KB}}^{\alpha,K}(\theta)$ and characteristic function of the interval $[-\pi, \pi]$. Bottom: Fourier transforms $\hat{\Psi}_{\mathrm{KB}}^{\alpha,K}(\omega)$ and $2\pi\mathrm{sinc}(\omega)$ in decibels. Here, dB denotes the logarithmic decay $10\log_{10}(|\phi(\omega)/\phi(0)|)$ of some quantity $\phi(\omega)$.

with $(m, n) \in \{0, \dots, N-1\}^2$ and reconstructs an approximation

$$f_{m,n} \simeq f^\dagger(m\Delta_{\mathrm{samp}}, n\Delta_{\mathrm{samp}}) \tag{10}$$

with $(m, n) \in \{0, \dots, N-1\}^2$. Here $f^\dagger$ is defined by (3), N is an even number, and $\Delta_{\mathrm{samp}} := X/N$. In the Appendix, we show that the sampling in (10) and (9) is sufficiently fine, provided that $\Delta_{\mathrm{samp}} \leq \pi/\Omega$, where Ω is the essential bandwidth of f.

Discretizing (3) with the trapezoidal rule gives

$$\sum_{n=0}^{N-1}\left(\sum_{m=0}^{N-1} e^{-i(ln+km)2\pi/N}f_{m,n}\right)$$
$$= \frac{2k}{\omega_{k,l}}\sum_{n=0}^{N-1} e^{-i\omega_{k,l}n2\pi/N}\left(\sum_{m=0}^{N-1} e^{-ikm2\pi/N}g_{m,n}\right) \tag{11}$$

where

$$\omega_{k,l} := \mathrm{sign}(l)\sqrt{k^2 + l^2},$$
$$(k, l) \in \{-N/2, \dots, N/2-1\}^2.$$

One notices that the inner sums in (11)

$$\tilde{g}_{k,n} := \sum_{m=0}^{N-1} e^{-ikm2\pi/N} g_{m,n} \qquad (12)$$

can be exactly evaluated with N one-dimensional FFTs, and the outer sums

$$\hat{g}_k(\omega_{k,l}) := \sum_{n=0}^{N-1} e^{-i\omega_{k,l}n2\pi/N} \tilde{g}_{k,n} \qquad (13)$$

can be approximately evaluated with N one-dimensional nonuniform FFTs. Denoting the resulting approximation by $\hat{g}_{k,l} \simeq \hat{g}_k(\omega_{k,l})$ and setting

$$\hat{f}_{k,l} := \frac{2k\hat{g}_{k,l}}{\omega_{k,l}}, \quad (k,l) \in \{-N/2, \ldots, N/2-1\}^2 \qquad (14)$$

we finally find

$$f_{n,m} := \frac{1}{N^2} \sum_{k,l=N/2}^{N/2-1} e^{i(km+ln)2\pi/N} \hat{f}_{k,l} \qquad (15)$$

with the inverse two-dimensional FFT algorithm.

Algorithm 2 Nonuniform FFT based algorithm for calculating $\mathbf{f} = (f_{m,n})_{n,m=0}^{N-1}$ using data $\mathbf{g} = (g_{m,n})_{m,n=0}^{N-1}$, oversampling factor c, interpolation length K, and window function Ψ.

---

1) $\Psi \leftarrow (\Psi(2\pi n/N - \pi))_n$ ▷ precomputations
2) $\hat{\Psi} \leftarrow (e^{-i(\omega_k - j/c)\pi/c}\hat{\Psi}(\omega_k - j/c))_{k,j}$
3)
4) **function** FouRecNufft $\mathbf{g}, c, K, \Psi, \hat{\Psi}$
5)   **for** $n = 0, \ldots, N-1$ **do**
6) $\mathbf{h} \leftarrow (g_{m,n})_m$
7) $(\tilde{g}_{k,n})_k \leftarrow$ fft$(\mathbf{h})$ ▷ one-dimensional FFT
8)   **end for**
9) $\mathbf{l} \leftarrow (-N/2, \ldots, N/2 - 1)$
10)   **for** $k = -N/2, \ldots, N/2 - 1$ **do**
11) $\omega \leftarrow$ sign$(\mathbf{l})\sqrt{k^2 + \mathbf{l}^2}$
12) $\mathbf{h} \leftarrow$ nufft$(\mathbf{h}, \omega, c, K, \Psi, \hat{\Psi})$ ▷ nonuniform FFT
13) $(f_{k,l})_l \leftarrow 2k\mathbf{h}/\omega$
14)   **end for**
15) $\mathbf{f} \leftarrow (f_{k,l})_{k,l}$
16) $\mathbf{f} \leftarrow$ ifft2$(\mathbf{f})$ ▷ two-dimensional inverse FFT
17)   **return** $\mathbf{f}$
18) **end function**

The nonuniform FFT based reconstruction algorithm is summarized in Algorithm 2. Its numerical complexity can easily be estimated. Evaluating (12) requires $N\mathcal{O}(N\log N)$ operations (N one-dimensional FFTs), evaluating (12) requires $N\mathcal{O}(N\log N)$ operations (N nonuniform FFTs), and (15) is evaluated with the inverse two-dimensional FFT in $\mathcal{O}(N^2\log N)$ operations. Therefore the overall complexity of Algorithm 1 is $\mathcal{O}(N^2\log N)$.

In the next section we numerically compare Algorithm 2 with standard Fourier algorithms presented in the literature

[41], [13], which all differ in the way how the sums in (13) are evaluated.

1) **Direct Fourier algorithm**. Equation (13) cannot be evaluated with the classical FFT algorithm because the nodes $\omega_{k,l}$ are nonequispaced. The most simple way to evaluate (13) is with direct summation. Because there are N^2 such sums, direct Fourier reconstruction requires $\mathcal{O}(N^3)$ operations. Consequently it does not lead to a fast algorithm. However, since (13) is evaluated exactly, it is optimally suited to evaluate the image quality of reconstructions with fast Fourier algorithms.

2) **Interpolation based algorithm**. A fast and simple alternative to direct Fourier reconstruction is as follows: Choose an oversampling factor $c \geq 1$ and exactly evaluate

$$\hat{g}_k(\omega) := \Delta_{\text{samp}} \sum_{n=0}^{N-1} e^{-i\omega n2\pi/N} \tilde{g}_{k,n}$$

at the uniformly spaced nodes $\omega = \Delta_{\text{samp}} j/c$, $j \in \{0, \ldots, Nc - 1\}$, with the one-dimensional FFT algorithm. In a next step, linear interpolation is used to find approximate values $\hat{g}_{k,l} \simeq \hat{g}_k(\omega_{k,l})$, see [13]. Evaluating $\hat{g}_{k,l}$ with linear interpolation requires $\mathcal{O}(N^2)$ operation and therefore the overall numerical effort of linear interpolation based Fourier reconstruction is $\mathcal{O}(N^2\log N)$. Algorithms using nearest neighbor interpolation instead of the linear one have the same numerical complexity and have also been applied to PAI (see, e.g., [42]). Higher order polynomial interpolation has been applied in [43] for a cubic recording geometry.

3) **Truncated** sinc **reconstruction**. If the function Ψ in Algorithm 2 is chosen as the characteristic function of the interval $[-c\pi, c\pi]$, $c \geq 1$, then the nonuniform fast Fourier transform reduces to the truncated sinc interpolation considered in [41]. However, due to the slow decay of $\text{sinc}(\omega)$, truncation will introduce a nonnegligible error in the reconstructed image (see Remark 3).

The Fourier algorithms are also be compared with a numerical implementation of the backprojection formula

$$f(x,y) = -\frac{2y}{\pi} \int_{\mathbb{R}} \left(\int_r^\infty \frac{(\partial_t t^{-1}\mathbf{Q}f)(x',t)}{\sqrt{t^2 - r^2}} dt \right) dx' \qquad (16)$$

where $r = \sqrt{(x-x')^2 + y^2}$ denotes the distance between the detector location $(x', 0)$ and the reconstruction point (x, y). Equation (16) has been obtained in [8] by applying the method of descent to the three-dimensional universal backprojection formula discovered by Xu and Wang [10]. Again (16) gives an exact reconstruction only if it is applied to complete data $(\mathbf{Q}f)(x,t)$, $(x,t) \in \mathbb{R}^2$. In the numerical experiments the backprojection formula is applied to the partial data $w_{\text{cut}}\mathbf{Q}f$, see (2), and implemented with $\mathcal{O}(N^3)$ operation counts as described in [8, Sec. 3.3].

V. NUMERICAL RESULTS

In the following we numerically compare the proposed nonuniform FFT based algorithm with standard Fourier algorithm and the backprojection algorithm based on (16).
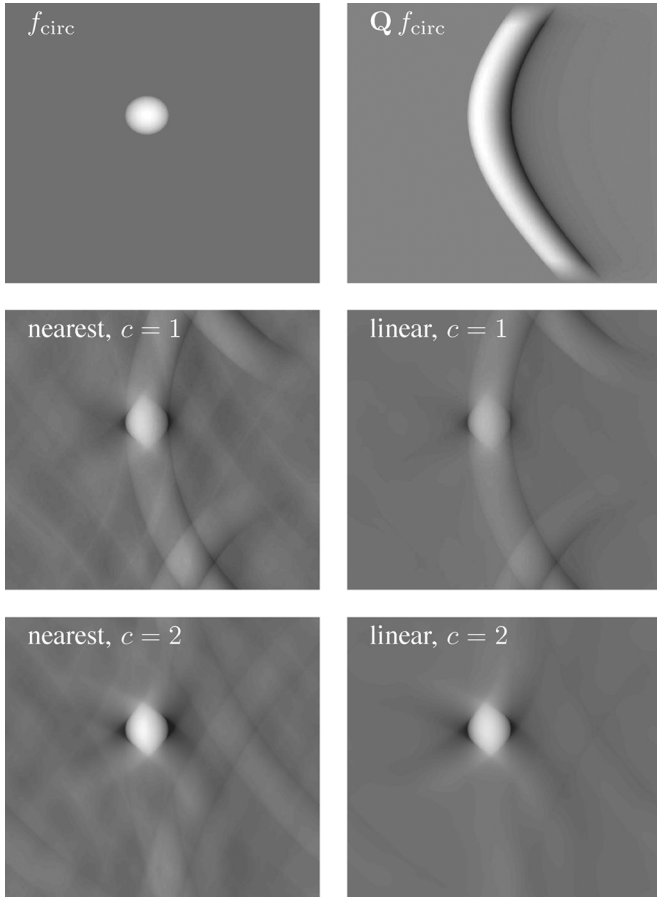
Fig. 3. Reconstruction with interpolation based Fourier algorithms. White corresponds to function value 1, black to function value -0.4. Top Line: Phantom and analytic data. Middle line: Reconstruction without oversampling ($c = 1$). Bottom line: Reconstruction with oversampling ($c = 2$).
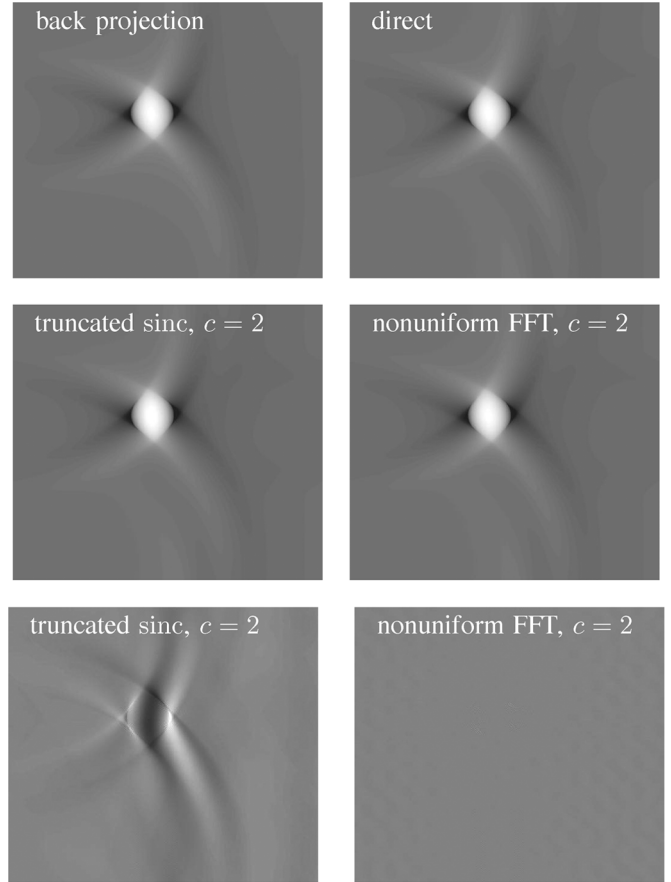

Fig. 4. Improved reconstructions. Top Line: Backprojection (left) and direct reconstruction (right). Middle Line: Truncated sinc (left) and nonuniform FFT based Fourier algorithm (right). Here, white corresponds to function value 1, black to function value -0.4. Bottom Line: Difference images between direct and truncated sinc reconstruction (left), and direct and nonuniform FFT based reconstruction (right). Here, white (resp. black) corresponds to function value 0.04 (resp. -0.04).

The cutoff function w_{cut} is constructed by convolution of

$$\varphi_\epsilon(x, t) = \begin{cases} C_\epsilon \exp(-1/(\epsilon - x^2 - t^2)^4), & \text{if } x^2 + t^2 < \epsilon, \\ 0, & \text{otherwise} \end{cases}$$

with the characteristic function of $[0, X]^2$, where ϵ is a small parameter and C_ϵ is chosen in such a way that $\int_{\mathbb{R}^2} \varphi_\epsilon(x, t) dx dt = 1$. Typically, ϵ is chosen as a "small" multiple of the sampling step size $\Delta_{\text{samp}} = X/N$.

In all numerical experiments, we take $X = 1$, and $N = 512$. The window width α is chosen to be slightly smaller than $\pi(2c - 1)$, where c is the oversampling factor that determines the accuracy of the Fourier reconstruction algorithms.

A. Circular Shaped Object

As first case example we use a circular shaped object

$$f_{\text{circ}}(\mathbf{x}) = \frac{2}{a} \begin{cases} (a^2 - |\mathbf{x} - \mathbf{x}_0|^2)^{1/2}, & \text{if } |\mathbf{x} - \mathbf{x}_0| < a, \\ 0, & \text{otherwise} \end{cases}$$

centered at $\mathbf{x}_0 := (x_0, y_0)$ (see top left image in Fig. 3). For such a simple object reconstruction artifacts can be identified very clearly. Moreover, the data $\mathbf{Q} f_{\text{circ}}$ can be evaluated analytically

(see [8, (B.1)]) as

$$(\mathbf{Q} f_{\text{circ}})(x, t)$$
$$= \frac{1}{a} \text{Re} \left[(s_+ - s_-) - t \log \left(\frac{s_+ + (t + a_i)}{s_- + (t - a_i)} \right) \right].$$

Here, $s_\pm := ((t \pm a)^2 + |(x, 0) - \mathbf{x}_0|^2)^{1/2}$, $\log(\cdot)$ is the principal branch of the complex logarithm, and $\text{Re}[z]$ denotes the real part of complex number z. The reconstruction results are depicted in Figs. 3 and 4. Table I and Fig. 5 compare run times with the relative ℓ^2-error

$$\frac{\|\mathbf{f} - \mathbf{f}^\dagger\|_{\ell^2}}{\|\mathbf{f}^\dagger\|_{\ell^2}} = \frac{\left(\sum_{m,n} (f_{m,n} - f_{m,n}^\dagger)^2 \right)^{1/2}}{\left(\sum_{m,n} (f_{m,n}^\dagger)^2 \right)^{1/2}}$$

were $\mathbf{f}^\dagger = (f_{m,n}^\dagger)$ denotes the discrete image obtained by direct Fourier reconstruction. Run times were measured for Matlab implementations on a personal computer with 2.4 GHz Athlon processor.

In order to demonstrate the stability of the Fourier algorithms, we also performed reconstructions from noisy data, where Gaussian noise was added with a variance equal to
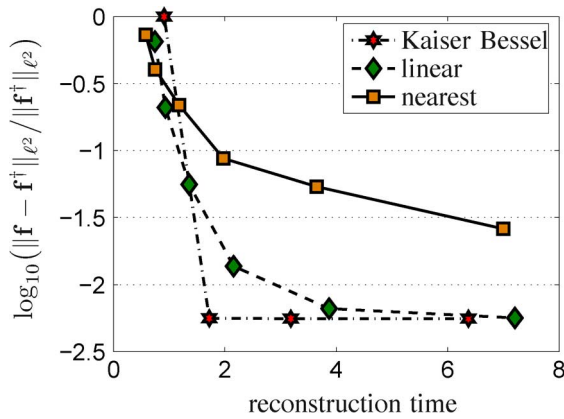
Fig. 5. Reconstruction time versus error. The points on the graphs belong to runtimes and errors for reconstruction with oversampling factors $c \in \{1, 2, 4, 8, 16, 32\}$.

TABLE I
RUN TIMES AND ERROR OF DIFFERENT RECONSTRUCTION METHODS

	c	ℓ^2-error	runtime (sec)
back projection	-	-	88.9
direct reconstruction	-	-	54.1
nearest neighbor	1	0.75	0.65
nearest neighbor	2	0.40	0.85
linear	1	0.65	0.8
linear	2	0.21	0.95
Truncates sinc	2	0.04	1.6
Kaiser Bessel	2	0.006	1.6

20% of the maximal data value. The reconstruction results are depicted in Fig. 6.

B. Shepp-Logan Phantom

In the next example, we consider the Shepp-Logan phantom f_{phant}, which is shown in top left image in Fig. 7. The data were calculated numerically by implementing d'Alemberts formula [44]

$$(\mathbf{Q}f_{\text{phant}})(x, 0, t) = \partial_t \int_0^t \frac{r(\mathbf{M}f_{\text{phant}})(x, 0, r)}{\sqrt{t^2 - r^2}} \, dr$$

with

$$(\mathbf{M}f_{\text{phant}})(x, 0, r) := \frac{1}{2\pi} \oint_{|\sigma|=1} f_{\text{phant}}((x, 0) + r\sigma) d\sigma$$

denoting the spherical mean Radon transform of f_{circ}. The reconstruction results from simulated data are depicted in Fig. 7.

C. Discussion

We emphasize that none of the above Fourier algorithms are designed to calculate an approximation of f but an approximation to the partial Fourier reconstruction $f^{\dagger}$ defined in (3). Therefore, even in the direct reconstruction (top right image in Fig. 4) and in the backprojection reconstruction one can see some blurred boundaries in the reconstruction. Such artifacts are expected using limited view data (2); see [38] and [37].

The results of interpolation based reconstruction without oversampling ($c = 1$) are quite useless. The reconstructions
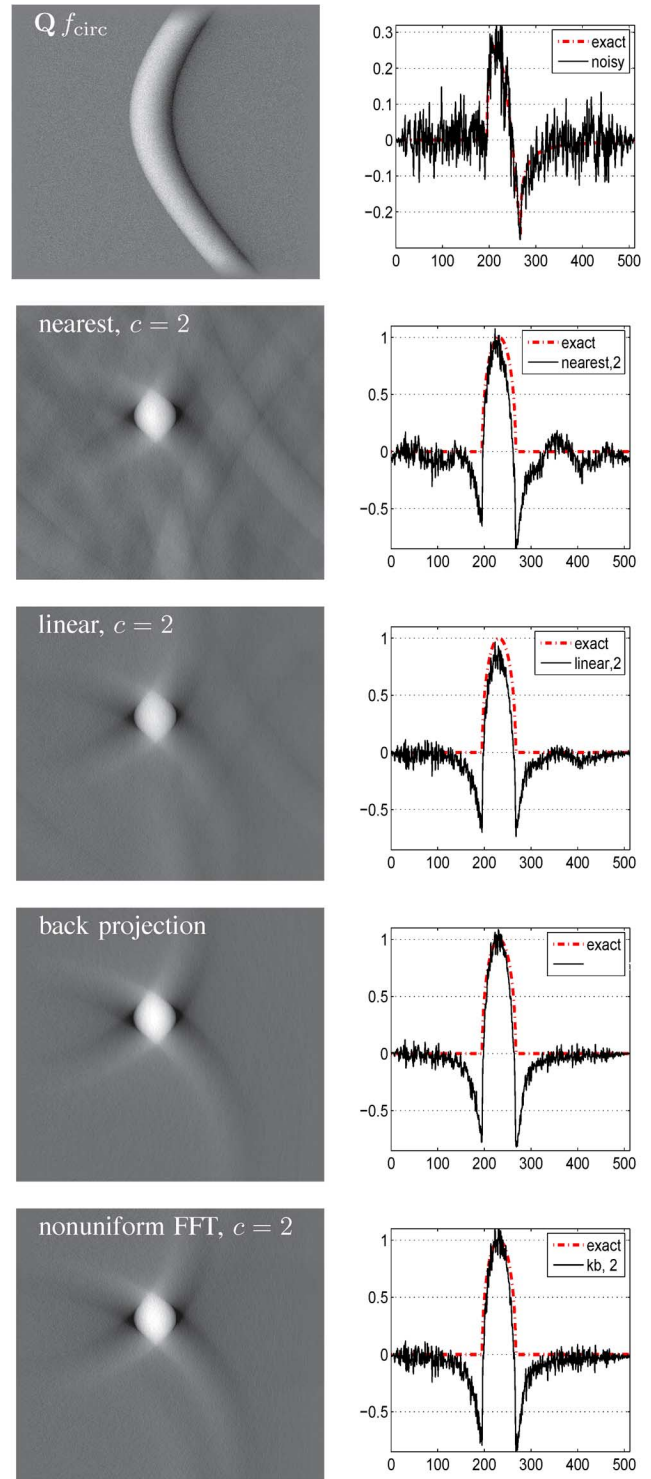

Fig. 6. Reconstruction from noisy data. Top Line: Noisy data. Second line: Nearest neighbor interpolation based reconstruction ($c = 2$). Third line: Linear interpolation based reconstruction ($c = 2$). Fourth line: Reconstruction with backprojection algorithm. Bottom line: Reconstruction with nonuniform FFT algorithm ($c = 2$). The horizontal profiles on the right are taken at $\{x = x_0\}$.

are significantly improved by using a larger oversampling factor c. However, even then, the results never reach the quality of the nonuniform FFT based reconstruction. Moreover, the numerical effort of linear interpolation based reconstruction is
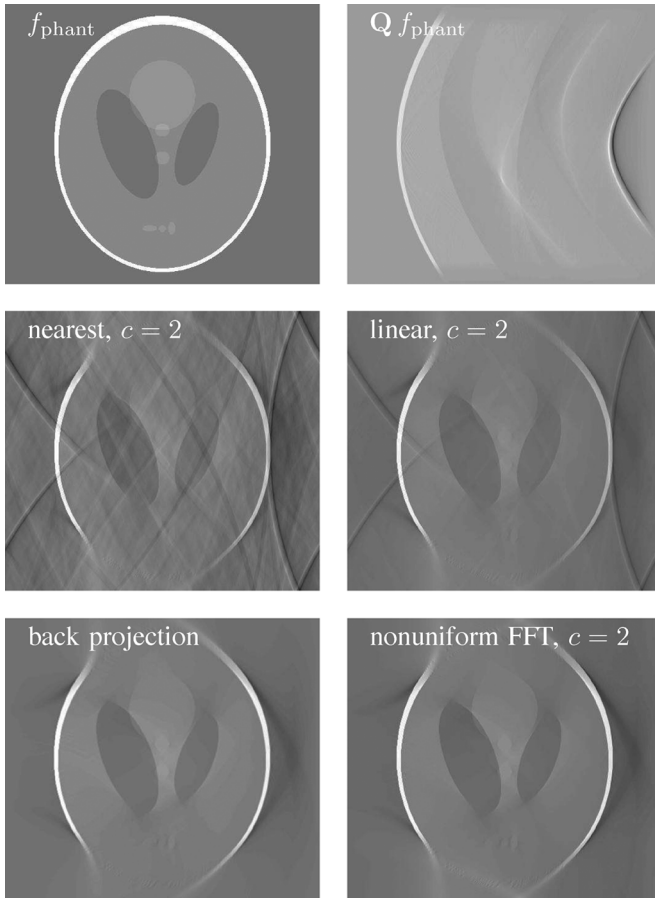
Fig. 7. Reconstruction of Shepp Logan phantom. Top line: Phantom and simulated data. Second line: Interpolation based reconstruction. Bottom line: Reconstruction with backprojection algorithm (left) and proposed nonuniform FFT algorithm (right).

proportional to the oversampling factor, which prohibits the use of "very large" values for c (see Fig. 5). In the reconstruction with $c = 2$ (bottom line in Fig. 3 and middle line in Fig. 7) artifacts are still clearly visible.

The images in the middle line of Fig. 4 suggest that truncated sinc and nonuniform FFT based reconstruction seem to perform quite similar. However, the differences to the direct Fourier reconstructions, shown in the bottom line in Fig. 4, demonstrate the higher accuracy of the nonuniform FFT based algorithm.

The results in Fig. 6 show that all applied reconstruction algorithms are quite stable with respect to data perturbation. In particular, the filtered backprojection algorithm produces images with the highest signal to noise ratio. However, only at the cost of a nearly 100 times longer computation time (see Table I).

VI. CONCLUSION

We presented a novel fast Fourier reconstruction algorithm for photoacoustic imaging using a limited planar detector array. The proposed algorithm is based on the nonuniform FFT. Theoretical investigation as well as numerical simulations show that our algorithm produces better images than existing Fourier algorithms with a similar numerical complexity. Moreover the proposed algorithm has been shown to be stable against data perturbations.

APPENDIX
SAMPLING AND RESOLUTION

Let f be smooth function that vanishes outside $(0, X)^d$, and define g, $f^\dagger$ by (2) and (3). We further assume that $\mathbf{F}w_{\mathrm{cut}}$ is concentrated around zero and, that f is essentially bandlimited with essential bandwidth Ω, in the sense that $(\mathbf{F}f)(\mathbf{K})$ is negligible for $|\mathbf{K}| \geq \Omega$. Note that since f has bounded support, $\mathbf{F}f$ cannot vanish exactly on $\{|\mathbf{K}| \geq \Omega\}$.

- **Sampling of** g. Equation (1) implies that

$$(\mathbf{F}g)(K_x, \omega) = (\mathbf{F}w_{\mathrm{cut}}) * (\mathbf{FQ}f)(K_x, \omega) \qquad (17)$$

with

$$(\mathbf{FQ}f)(K_x, \omega) = \frac{2\omega(\mathbf{F}f)(K_x, \mathrm{sign}(\omega)\sqrt{\omega^2 - |K_x|^2})}{\mathrm{sign}(\omega)\sqrt{\omega^2 - |K_x|^2}}$$

if $|\omega| > |K_x|^2$ and $(\mathbf{FQ}f)(K_x, \omega) = 0$ otherwise. The assumption that f has essential bandwidth Ω and (17) imply that $(\mathbf{F}g)(K_x, \omega)$ is negligible outside the set

$$\{(K_x, \omega) : |K_x| \leq |\omega| \leq \Omega\} \subset (-\Omega, \Omega)^d.$$

Now Shannon's sampling theorem [39], [40] states that g is sufficiently fine sampled if the step size in x and in t satisfies the Nyquist condition $\Delta_{\mathrm{samp}} \leq \pi/\Omega$.

- **Sampling of** $f^\dagger$. Similar considerations as above again show that $f^\dagger$ is essentially bandlimited with essential bandwidth Ω. Shannon's sampling theorem implies that $f^\dagger$ can be reliable reconstructed from discrete samples taken with step size $\Delta_{\mathrm{samp}} \leq \pi/\Omega$.

If f has essential bandwidth larger than Ω, the function g has to be filtered with a low pass-filter *before* sampling. Otherwise, sampling introduces aliasing artifacts in the reconstructed image.

Theoretically, the resolution (at least of the visible parts) can be increased ad infinity by simply decreasing the sampling size Δ_{samp}. In practical applications, several other factors such as the bandwidth of the ultrasound detection system limit the bandwidth of the data, and therefore the resolution of reconstructed images [33]. This, however, also guarantees that in practice a moderate sampling step size Δ_{samp} gives correct sampling without aliasing.

REFERENCES

[1] R. A. Kruger, W. L. Kiser, D. R. Reinecke, G. A. Kruger, and K. D. Miller, "Thermoacoustic molecular imaging of small animals," *Mol. Imag.*, vol. 2, no. 2, pp. 113–123, 2003.

[2] X. D. Wang, G. Pang, Y. J. Ku, X. Y. Xie, G. Stoica, and L. V. Wang, "Noninvasive laser-induced photoacoustic tomography for structural and functional *in vivo* imaging of the brain," *Nature Biotech.*, vol. 21, no. 7, pp. 803–806, 2003.

[3] R. A. Kruger, K. D. Miller, H. E. Reynolds, W. L. Kiser, D. R. Reinecke, and G. A. Kruger, "Breast cancer in vivo: Contrast enhancement with thermoacoustic CT at 434 MHz-feasibility study," *Radiol.*, vol. 216, no. 1, pp. 279–283, 2000.

[4] S. Manohar, A. Kharine, J. C. G. van Hespen, W. Steenbergen, and T. G. van Leeuwen, "The twente photoacoustic mammoscope: System overview and performance," *Phys. Med. Biol.*, vol. 50, no. 11, pp. 2543–2557, 2005.

[5] R. G. M. Kolkman, E. Hondebrink, W. Steenbergen, and F. F. M. De Mul, "In vivo photoacoustic imaging of blood vessels using an extreme-narrow aperture sensor," *IEEE J. Sel. Topics Quantum Electron.*, vol. 9, no. 2, pp. 343–346, 2003.

[6] R. O. Esenaliev, I. V. Larina, K. V. Larin, D. J. Deyo, M. Motamedi, and D. S. Prough, "Optoacoustic technique for noninvasive monitoring of blood oxygenation: A feasibility study," *App. Opt.*, vol. 41, no. 22, pp. 4722–4731, 2002.

[7] L. E. Andersson, "On the determination of a function from spherical averages," *SIAM J. Math. Anal.*, vol. 19, no. 1, pp. 214–232, 1988.

[8] P. Burgholzer, J. Bauer-Marschallinger, H. Grün, M. Haltmeier, and G. Paltauf, "Temporal back-projection algorithms for photoacoustic tomography with integrating line detectors," *Inv. Probl.*, vol. 23, no. 6, pp. 65–80, 2007.

[9] J. A. Fawcett, "Inversion of n-dimensional spherical averages," *SIAM J. Appl. Math.*, vol. 45, no. 2, pp. 336–341, 1985.

[10] M. Xu and L. V. Wang, "Universal back-projection algorithm for photoacoustic computed tomography," *Phys. Rev. E*, vol. 71, no. 1, pp. 0 167 061–0 167 067, 2005.

[11] M. A. Anastasio, D. Zhang, J. Modgil, and P. L. La Riviere, "Application of inverse source concepts to photoacoustic tomography," *Inv. Probl.*, vol. 23, no. 6, pp. S21–S35, 2007.

[12] S. J. Norton and M. Linzer, "Ultrasonic reflectivity imaging in three dimensions: Exact inverse scattering solutions for plane, cylindrical and spherical apertures," *IEEE Trans. Biomed. Eng.*, vol. 28, no. 2, pp. 202–220, Feb. 1981.

[13] Y. Xu, D. Feng, and L. V. Wang, "Exact frequency-domain reconstruction for thermoacoustic tomography—I: Planar geometry," *IEEE Trans. Med. Imag.*, vol. 21, no. 7, pp. 823–828, Jul. 2002.

[14] K. Köstli, D. Frauchinger, J. Niederhauser, G. Paltauf, H. Weber, and M. Frenz, "Optoacoustic imaging using a three-dimensional reconstruction algorithm," *IEEE J. Quantum Electron.*, vol. 7, no. 6, pp. 918–923, Nov./Dec. 2001.

[15] K. P. Köstli, M. Frenz, H. Bebie, and H. P. Weber, "Temporal backward projection of optoacoustic pressure transients using Fourier transform methods," *Phys. Med. Biol.*, vol. 46, pp. 1863–1872, 2001.

[16] M. Haltmeier, T. Schuster, and O. Scherzer, "Filtered backprojection for thermoacoustic computed tomography in spherical geometry," *Math. Methods Appl. Sci.*, vol. 28, no. 16, pp. 1919–1937, 2005.

[17] F. Natterer, *The Mathematics of Computerized Tomography.*. Stuttgart, Germany: Teubner, 1986.

[18] G. Beylkin, "On the fast Fourier transform of functions with singularities," *Appl. Comput. Harmon. Anal.*, vol. 2, no. 4, 1995.

[19] A. Dutt and V. Rokhlin, "Fast Fourier transforms for nonequispaced data," *SIAM J. Sci. Comput.*, vol. 14, no. 6, 1993.

[20] J. A. Fessler and B. P. Sutton, "Nonuniform fast Fourier transforms using min-max interpolation," *IEEE Trans. Signal Process.*, vol. 51, no. 2, pp. 560–574, Feb. 2003.

[21] L. Greengard and J. Lee, "Accelerating the nonuniform fast Fourier transform," *SIAM Rev.*, vol. 46, no. 3, pp. 443–454, 2004.

[22] D. Potts, G. Steidl, and M. Tasche, "Fast Fourier transforms for nonequispaced data: A tutorial," in *Modern Sampling Theory*, ser. Appl. Numer. Harmon. Anal.. Boston, MA: Birkhäuser, 2001, pp. 247–270.

[23] G. Steidl, "A note on fast Fourier transforms for nonequispaced grids," *Adv. Comput. Math.*, vol. 9, no. 3–4, pp. 337–352, 1998.

[24] M. M. Bronstein, A. M. Bronstein, M. Zibulevsky, and H. Azhari, "Reconstruction in diffraction ultrasound tomography using nonuniform FFT," *IEEE Trans. Med. Imag.*, vol. 21, no. 11, pp. 1395–1401, Nov. 2002.

[25] J. A. Fessler, "On NUFFT-based gridding for non-Cartesian MRI," *J. Magn. Reson.*, pp. 191–195, 2007.

[26] D. Gottlieb, B. Gustafsson, and P. Forssen, "On the direct Fourier method for computer tomography," *IEEE Trans. Med. Imag.*, vol. 19, no. 3, pp. 223–232, Mar. 2000.

[27] J. D. O'Sullivan, "A fast sinc function gridding algorithm for Fourier inversion in computer tomography," *IEEE Trans. Med. Imag.*, vol. 4, no. 4, pp. 200–207, Dec. 1985.

[28] H. Schomberg and J. Timmer, "The gridding method for image reconstruction by Fourier transformation," *IEEE Trans. Med. Imag.*, vol. 14, no. 3, pp. 596–607, Sep. 1995.

[29] K. Fourmont, "Non-equispaced fast Fourier transforms with applications to tomography," *J. Fourier Anal. Applicat.*, vol. 9, no. 5, pp. 431–450, 2003.

[30] P. Kuchment and L. A. Kunyansky, "Mathematics of thermoacoustic and photoacoustic tomography," *Eur. J. Appl. Math.*, vol. 19, pp. 191–224, 2008.

[31] S. K. Patch and O. Scherzer, "Special section on photo- and thermoacoustic imaging," *Inv. Probl.*, vol. 23, pp. S1–S122, 2007.

[32] O. Scherzer, M. Grasmair, H. Grossauer, M. Haltmeier, and F. Lenzen, *Variational Methods in Imaging*, ser. Appl. Math. Sci.. New York: Springer, 2009, vol. 167.

[33] M. Xu and L. V. Wang, "Photoacoustic imaging in biomedicine," *Rev. Sci. Instrum.*, vol. 77, no. 4, pp. 1–22, 2006.

[34] K. Köstli and P. Beard, "Two-dimensional photoacoustic imaging by use of Fourier-transform image reconstruction and a detector with an anisotropic response," *Appl. Opt.*, vol. 42, no. 10, pp. 1899–1908, 2003.

[35] G. Paltauf, R. Nuster, M. Haltmeier, and P. Burgholzer, "Experimental evaluation of reconstruction algorithms for limited view photoacoustic tomography with line detectors," *Inv. Probl.*, vol. 23, no. 6, pp. 81–94, 2007.

[36] X. Pan and M. A. Anastasio, "On a limited-view reconstruction problem in diffraction tomography," *IEEE Trans. Med. Imag.*, vol. 21, no. 4, pp. 413–416, Apr. 2002.

[37] Y. Xu, L. V. Wang, G. Ambartsoumian, and P. Kuchment, "Reconstructions in limited-view thermoacoustic tomography," *Med. Phys.*, vol. 31, no. 4, pp. 724–733, 2004.

[38] A. Louis and E. Quinto, "Local tomographic methods in sonar," in *Surveys on Solution Methods for Inverse Problems.*. New York: Springer, 2000, pp. 147–154.

[39] F. Natterer and F. Wübbeling, *Mathematical Methods in Image Reconstruction*, ser. Monographs Math. Model. Comput.. Philadelphia, PA: SIAM, 2001, vol. 5.

[40] M. Unser, "Sampling—50 years after Shannon," *Proc. IEEE*, vol. 88, no. 4, pp. 569–587, Apr. 2000.

[41] M. Jaeger, S. Schüpbach, A. Gertsch, M. Kitz, and M. Frenz, "Fourier reconstruction in optoacoustic imaging using truncated regularized inverse k-space interpolation," *Inv. Probl.*, vol. 23, pp. S51–S63, 2007.

[42] B. T. Cox, S. R. Arridge, and P. C. Beard, "Photoacoustic tomography with a limited-aperture planar sensor and a reverberant cavity," *Inv. Prob.*, vol. 23, no. 6, pp. S95–S112, 2007.

[43] L. A. Kunyansky, "A series solution and a fast algorithm for the inversion of the spherical mean radon transform," *Inv. Prob.*, vol. 23, no. 6, pp. S11–S20, 2007.

[44] R. Courant and D. Hilbert, *Methods of Mathematical Physics.*. New York: Wiley, 1962, vol. 2.
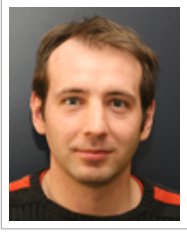
Mag. Gerhard Zangerl

Universitäre Ausbildung

2010 — **Voraussichtlicher Abschluss des Doktoratsstudiums**, *Titel der Dissertation*, "Thermoacoustic Tomography with Circular Integrating Detectors".

2009 — **Fortsetzung des Doktoratsstudiums**, an der Universität Wien.

2006 — **Beginn des Doktoratsstudiums**, an der Leopold-Franzens Universität Innsbruck.

2005 — **Abschluss des Magisterstudiums**, *Titel der Diplomarbeit*, "Der Parallelentransport auf zweidimensionalen Untermannigfaltigkeiten des dreidimenionalen Raumes".

1999-2005 — **Studium der Mathematik**, an der Leopold-Franzens Universität Innsbruck.

Schulbildung

1995-1999 — **Meinhardinum Stams**.

1987-1995 — **Hauptschule Kappl & Volksschule Ischgl**.

Berufliche Laufbahn

Oktober 2009 — **Wissenschaftlicher Mitarbeiter**, *am Computational Science Center (ehemalige Infmath Imaging Group)*, Angestellt im Rahmen des FWF Projektes: Photoacoustic Imaging in Biology and Medicine.

Mai 2006 — **Wissenschaftlicher Mitarbeiter**, *an der Infmath Imaging Group*, Angestellt im Rahmen des FWF Projektes: "Photoacoustic Imaging in Biology and Medicine".

Zusätzliche Tätigkeiten

Lehrtätigkeiten

2002-2005 — **Tutor**, in den Fächern Analytische Geometrie und Algorithmische Mathematik 1 & 2.

Stumpergasse 23 – 1160 Wien
+43-650-8523410 • ☎ *+43-1-4277-23705*
• ✉ *Gerhard.Zangerl@univie.ac.at* • *date of birth: March 6, 1981*

1/3

| 1999-2005 | **Nachilfelehrer**, Tätigkeit als Nachhilfelehrer in den Fächern Mathematik und Physik. |

Organisatorisches

seit Juni 2010	**Application for the second period of the NRN**, Mitarbeit bei der Organisation und Coordination des Folgeantrages für das FWF Projekt: "Photoacoustic Imaging in Biology and Medicine".
2009	**Recent developments in tomography**, Organisation eines Minisymposiums mit M. Haltmeier, Conference on Applied Inverse Problems 2009, Vienna.
2009	**Recent developments in photo- and thermoacoustic tomography**, Organisation eines Minisymposiums mit M. Haltmeier, Conference on Applied Inverse Problems 2009, Vienna.

Tätigkeit als Gutacher

2009	**Estimation of Tension Force in Double Hangers by a System Identification Approach**, *in Inverse Problems in Science and Engineering*.
2009	**Perturbation Method for Degenerate Identification Problems in Abstract Spaces**, *in Inverse Problems in Science and Engineering*.
2010	**Photoacoustic and Thermoacoustic Tomography: Image Formation Principles**, *in Handbook of Mathematical Methods in Imaging*.

Sonstige Fähigkeiten

| EDV Kenntnisse | **LaTex, MATLAB, Maple**. |

| Fremdsprachen | **Englisch**, *Gute Englischkenntnisse in Wort und Schrift*. |

| Führerschein | **PKW Führerschein**. |

Publikationen

Journale

[Journal 5]	**Full field detection in photoacoustic tomography**, *R. Nuster, G. Zangerl, M. Haltmeier, and G. Paltauf*, submitted, 2009.
[Journal 4]	**Exact series reconstruction in photoacoustic tomography with circular integrating detectors**, *G. Zangerl, M. Haltmeier, and O. Scherzer*, Commun. Math. Sci., 7(3):665–678, 2009.
[Journal 3]	**A reconstruction algorithm for photoacoustic imaging based on the nonuniform FFT**, *M. Haltmeier, O. Scherzer, and G. Zangerl*, IEEE Trans. Med. Imag., 28(3):1727–173, 2009.

.

Stumpergasse 23 – 1160 Wien
📟 *+43-650-8523410* • ☎ *+43-1-4277-23705*
• ✉ *Gerhard.Zangerl@univie.ac.at* • *date of birth: March 6, 1981*

2/3

[Journal 2] **Circular integrating detectors in photo and thermoacoustic tomography**, *G. Zangerl, M. Haltmeier, and O. Scherzer*, Inverse Probl. Sci. Eng., 17(1):133–142, 2009.

[Journal 1] **Exact reconstruction in photoacoustic tomography with circular integrating detectors ii: Spherical geometry**, *G. Zangerl and O. Scherzer*, Math. Methods in Appl. Sci., to appear 2010.

Proceedings

[Proc 2] **Influence of bandwidth and detector size to the resolution of photoacoustic tomography**, *M. Haltmeier, O. Scherzer, and G. Zangerl*, Proceedings MATHMOD 2009 in Vienna, ARGESIM Report no. 35, 2009.

[Proc 2] **Cylindrical coordinates in thermoacoustic tomography**, *G. Zangerl, O. Scherzer, and M. Haltmeier*, Proc. to Inverse Problems, Design and Optimization Symposium (IPDO 2007), Miami, Florida, USA: 564–569, 2007.

Vorträge

2010 **ECMI**, Wuppertal.

2010 **PAI Meeting**, Innsbruck.

2009 **PAI Meeting**, Innsbruck.

2009 **AIP**, Wien.

2008 **Variational Methods in imaging**, Universitätszentrum Obergurgel.

2007 **IPDO**, Miami, US.

2007 **Industrial Geometry**, Strobl.

Stumpergasse 23 – 1160 Wien
+43-650-8523410 • *+43-1-4277-23705*
• *Gerhard.Zangerl@univie.ac.at* • *date of birth: March 6, 1981*

3/3